**Naval Surface Warfare Center**
**Carderock Division**
West Bethesda, MD 20817-5700

**NSWCCD-61-TR-2020/24** **October 2020**

Platform Integrity Department

Technical Report

# Temperature-Dependent Material Property Databases for Marine Steels – Part 3: HSLA-80

by

Jennifer K. Semple

Daniel H. Bechetti

Wei Zhang

Charles R. Fisher

**Naval Surface Warfare Center**
**Carderock Division**
West Bethesda, MD 20817-5700

**NSWCCD-61-TR-2020/24** **October 2020**

Platform Integrity Department
Technical Report

# Temperature-Dependent Material Property Databases for Marine Steels – Part 3: HSLA-80

by
Jennifer K. Semple
Daniel H. Bechetti
Wei Zhang
Charles R. Fisher

# REPORT DOCUMENTATION PAGE

*Form Approved*
*OMB No. 0704-0188*



| 1. REPORT DATE *(DD-MM-YYYY)* | 2. REPORT TYPE | 3. DATES COVERED *(From - To)* |
|---|---|---|
| 28-10-2020 | Technical Report | JAN 2017 – DEC 2017 |

**4. TITLE AND SUBTITLE**

Temperature-Dependent Material Property Databases for Marine Steels – Part 3: HSLA-80

**5a. CONTRACT NUMBER** N/A

**5b. GRANT NUMBER** N/A

**5c. PROGRAM ELEMENT NUMBER** N/A

**6. AUTHOR(S)**

Jennifer K. Semple
Daniel H. Bechetti
Wei Zhang
Charles R. Fisher

**5d. PROJECT NUMBER** N/A

**5e. TASK NUMBER**

**5f. WORK UNIT NUMBER**

**7. PERFORMING ORGANIZATION NAME(S) AND ADDRESS(ES) AND ADDRESS(ES)**

Naval Surface Warfare Center,
Carderock Division, Code 611
9500 MacArthur Boulevard
West Bethesda, MD 20817-5700

Ohio State University, Department of Materials Science & Engineering
Welding Engineering Program
1248 Arthur Adams Dr
Columbus, OH 43221

**8. PERFORMING ORGANIZATION REPORT NUMBER**

NSWCCD-61-TR-2020/24

**9. SPONSORING / MONITORING AGENCY NAME(S) AND ADDRESS(ES)**

William Mullins
Program Manager, 332
Office of Naval Research
Arlington, VA 22217

Lightweight Innovations for Tomorrow (LIFT)
Detroit, MI 48216

**10. SPONSOR/MONITOR'S ACRONYM(S)**

**11. SPONSOR/MONITOR'S REPORT NUMBER(S)**

**12. DISTRIBUTION / AVAILABILITY STATEMENT**

DISTRIBUTION A. Approved for public release: distribution unlimited.

**13. SUPPLEMENTARY NOTES**

**14. ABSTRACT:**

The Lightweight Innovations for Tomorrow (LIFT) project entitled, *Robust Distortion Control Methods and Implementation for Construction of Lightweight Metallic Structures*, sought to address distortion issues with thin-plate steel fabrication of U.S. Navy ships. Integrated Computational Materials Engineering (ICME)-based tools and techniques were identified as the best path forward for distortion mitigation through computational simulation of the welding process. ICME tools require temperature-dependent material properties to achieve accurate computational results for distortion and residual stress. Properties of note include specific heat, thermal conductivity, coefficient of thermal expansion, elastic modulus, yield strength, and flow stress, from room temperature up to nearly the alloy's melting point. In addition, the temperatures associated with on-heating and on-cooling phase transformations and their variation with heating rate, cooling rate, and peak temperature are also important for the prediction of stress and distortion evolution.

The integrated project team (IPT) made generating pedigreed, temperature-dependent material property databases of Navy-relevant steels a key task within the LIFT project. The testing plan included some of the most common marine steels used in the construction of U.S. Naval vessels; namely DH36, HSLA-65, HSLA-80, HSLA-100, HY-80, and HY-100. Material testing for each of the six steel grades was performed jointly by the Welding Engineering Program within the Department of Materials Science and Engineering at the Ohio State University (OSU) and the Welding, Processing, and Nondestructive Evaluation Branch at the Naval Surface Warfare Center, Carderock Division (NSWCCD). The temperature-dependent material property data was then sent to ESI for adaptation for use in their welding-based, finite-element analysis (FEA) software colloquially known as SYSWELD.

This report is part of a seven-part series detailing the pedigreed steel data. The first six reports will report and discuss the material properties for each of the individual steel grades, whereas the final report will compare and contrast the measured steel properties across all six steels, while also comparing them to the available literature data. This report will focus specifically on the data associated with HSLA-80 steel.

**15. SUBJECT TERMS**

ICME, CWM, SYSWELD, Computational Simulation, Steel, Welding, Material Database, HSLA-80

| 16. SECURITY CLASSIFICATION OF: UNCLASSIFIED | | | 17. LIMITATION OF ABSTRACT | 18. NUMBER OF PAGES | 19a. RESPONSIBLE PERSON |
|---|---|---|---|---|---|
| a. REPORT | b. ABSTRACT | c. THIS PAGE | | | 19b. TELEPHONE NUMBER |
| UNCLASSIFIED | UNCLASSIFIED | UNCLASSIFIED | | 77 | Charles Fisher<br>(301) 227-4969 |

## CONTENTS

*Page*

## FIGURES

*Page*

## TABLES

*Page*

## ADMINISTRATIVE INFORMATION

The work described in this report was performed by the Welding, Processing, and Nondestructive Evaluation Branch (Code 611) of the Platform Integrity Department at the Naval Surface Warfare Center, Carderock Division (NSWCCD) and by the Department of Materials Science and Engineering at the Ohio State University. The work was funded in FY17 by the Office of Naval Research (ONR), in support of the Lightweight Innovations for Tomorrow (LIFT) Institute's program entitled *Robust Distortion Control Methods and Implementation for Construction of Lightweight Metallic Structures*.

## ACKNOWLEDGEMENTS

The authors would like to thank the other members of the LIFT Joining-R1-3 integrated project team, including other engineers at the Naval Surface Warfare Center, Carderock Division (Matthew Sinfield, David Kihl, Maria Posada, and Johnnie Deloach), Huntington Ingalls Industries – Ingalls Shipbuilding (T.D. Huang, Harry Rucker, Randy Johnson, Yu-Ping Yang, Steve Scholler, Charlotte Merritt, Michael Harbison, Shannon Dolese, Anthony Copeland, Melvin Washington, Stacey Merritt, Win Delancey, Dianna Genton, Lee Kvidahl, and John Walks), the University of Michigan (Pingsha Dong, Jack Hu, Matt Collette, Haseung Chung, Mark Groden, Mark Para-Shostrand, and Trey Neveux), the Massachusetts Institute of Technology (Richard Roth, Michele Bustamante, Randy Kirchain, and Joel Clark), EWI (Randy Dull and Wael Alfakir), ESI (Yogendra [San] Gooroochan and Mark Doroudian), the American Bureau of Shipping (Alex Gonzalez and Kin-Ling Sham), Comau, LLC (Martin Kinsella) and LIFT (Melvin Hawke, Alan Taub, and Hadrian Rori), for their technical assistance in the completion of this work.

*This page intentionally left blank*

## EXECUTIVE SUMMARY

*The Lightweight Innovations for Tomorrow (LIFT) project entitled, Robust Distortion Control Methods and Implementation for Construction of Lightweight Metallic Structures, sought to address distortion issues with thin-plate steel fabrication of U.S. Navy ships. Integrated Computational Materials Engineering (ICME)-based tools and techniques were identified as the best path forward for distortion mitigation through computational simulation of the welding process. ICME tools require temperature-dependent material properties to achieve accurate computational results for distortion and residual stress. Properties of note include specific heat, thermal conductivity, coefficient of thermal expansion, elastic modulus, yield strength, and flow stress of alloys from room temperature to near melting. In addition, the temperatures associated with on-heating and on-cooling phase transformations and their variation with heating rate, cooling rate, and peak temperature are also important for the prediction of stress and distortion evolution.*

*The integrated project team (IPT) made generating pedigreed, temperature-dependent material property databases of Navy-relevant steels a key task within the LIFT project. The testing plan included some of the most common marine steels used in the construction of U.S. Naval vessels; namely, DH36, HSLA-65, HSLA-80, HSLA-100, HY-80, and HY-100. Material testing for each of the six steel grades was performed jointly by the Welding Engineering Program within the Department of Materials Science and Engineering at the Ohio State University (OSU) and the Welding, Processing, and Nondestructive Evaluation Branch at the Naval Surface Warfare Center, Carderock Division (NSWCCD). The temperature-dependent material property data was then sent to ESI for adaptation for use in their welding-based, finite-element analysis (FEA) software colloquially known as SYSWELD.*

*This report is part of a seven-part series detailing the pedigreed steel data. The first six reports will report and discuss the material properties for each of the individual steel grades, whereas the final report will compare and contrast the measured steel properties across all six steels, while also comparing them to the available literature data. This report will focus specifically on the data associated with HSLA-80 steel.*

## BACKGROUND

The Lightweight Innovations for Tomorrow (LIFT) project entitled, *Robust Distortion Control Methods and Implementation for Construction of Lightweight Metallic Structures*, is a collaborative research project to address the complex fabrication problems that arise from the use of thin, high-strength steel panels for ship construction. The importance of lightweighting in the commercial and military shipbuilding sectors has gained attention in recent decades as a way to increase the performance capabilities of products while also reducing total ownership costs. Over the past decade, the production ratio of thin plate (10 mm [3/8-in.] or less) to thicker plate structures for steel construction at Huntington Ingalls Industries – Ingalls Shipbuilding has risen to over 80% in the Coast Guard's National Security Cutter (NSC) program. Modern naval vessel designs also make greater use of complex panels with inserts and cutouts, further increasing the fabrication complexity to achieve weight savings while meeting structural requirements.

European shipbuilding research suggests that 30% of hull fabrication costs can be attributed to re-work and fit-up issues due to distortion [1]. Integrated Computational Materials Engineering (ICME)

tools can be used to quantify distortions associated with the fabrication process of complex stiffened panels or other lightweight structures. These tools, once validated on selected product forms, could be used to establish recommended fitting, fixturing, welding, and assembly sequencing for optimized distortion control in thin-plate steel construction.

These ICME tools require detailed, reliable databases of temperature-dependent material properties in order to increase the accuracy of calculated distortion and residual stresses in welded metallic structures. Of highest importance to the fidelity of such models are the thermo-physical and thermo-mechanical properties of the material(s) being joined. The properties of note include specific heat, thermal conductivity, coefficient of thermal expansion (CTE), elastic modulus, yield strength, and flow stress of the alloy, from room temperature to near melting. The temperatures associated with on-heating and on-cooling phase transformations and their variation with heating rate, cooling rate, and peak temperature are also important for the prediction of stress and distortion evolution.

While some of these data exist for the most common Navy steels, they are generally not suitable for use in high-fidelity welding-focused computational models for several reasons. First, the methods of data generation are inconsistent because the testing was completed over many decades by separate researchers and programs. Also, significant gaps exist in the data, especially at temperatures above approximately 400 °C (~750 °F). Additionally, some available data are restricted against public distribution. Finally, the data are, in general, subject to reliability issues because of changes in material fabrication and testing practices that have occurred in the decades since the data were generated. To combat this lack of comprehensive and consistent data, the integrated project team IPT made generating pedigreed, temperature-dependent material property databases of Navy-relevant steels a key task within the LIFT project. A major portion of the tasking involved analysis of heat-affected zone (HAZ) microstructures, as this region of rapidly changing microstructure results in significant variation of local mechanical properties. These HAZ microstructures for Navy-relevant steels also do not have well-established mechanical property data, especially as a function of temperature and heating or cooling rate.

The testing plan included some of the most common marine steels used in the construction of U.S. Naval vessels; namely DH36, HSLA-65, HSLA-80, HSLA-100, HY-80, and HY-100. HSLA is short for “high-strength low-alloy,” whereas HY stands for “high yield.” The number designation behind HSLA and HY is the minimum yield strength of the plate material in units of ksi. Current (as of this writing) specifications for these alloys can be found in references [2] [3] [4]. Material testing for each of the six steel grades was performed jointly by the Welding Engineering Program within the Department of Materials Science and Engineering at the Ohio State University (OSU) and the Welding, Processing, and Nondestructive Evaluation Branch at the Naval Surface Warfare Center, Carderock Division (NSWCCD). The temperature-dependent material property data was then sent to ESI for adaptation for use in their welding-based, finite-element analysis (FEA) software colloquially known as *SYSWELD*.

This report is part of a seven-part series based on the pedigreed steel data. The first six reports will focus on establishing the material properties for each of the individual steel grades, whereas the final report will compare and contrast the measured steel properties across all six steels, while also comparing them to the available literature data. Follow-on reports detailing use of these temperature-dependent material databases are also expected. While this report focuses on HSLA-80 data, previous reports on DH36 and HSLA-65 can be found in [5]and [6], respectively.

# APPROACH

## Material Testing Program

The material property assessment program was developed through inputs from welding engineers at NSWCCD, researchers at OSU, and modeling experts at ESI. The program focused on generating the types of data required to develop Navy-relevant material databases for use by ESI's commercial software, *SYSWELD*. The raw data could also be adapted for use by other FEA tools, such as MSC's *Simufact Welding* or the welding module for *Abaqus*. Specific data included thermo-physical and mechanical properties of the alloys of interest, from room temperature up to near-melting. Density, heat capacity, thermal conductivity, and CTE were identified as the most important thermo-physical properties. Mechanical properties of interest included the elastic modulus, yield strength, and flow stress.

Material from a single HSLA-80 steel plate, procured to NAVSEA Technical Publication T9074-BD-GIB-010/0300 (Tech Pub 300) [4], was analyzed for this project. The plate was acquired by Huntington Ingalls Industries – Ingalls Shipbuilding (HII – Ingalls) and was nominally 4.76 mm (3/16-in.) thick. The room temperature yield strength and elongation requirements for this plate thickness are 552-758 MPa (80-110 ksi) and 14% in 50 mm (2-in.), respectively [4]. There are no ultimate tensile strength requirements for HSLA-80 plate procured to Tech Pub 300 [4]. The plate conformance certification sheet for the material investigated in this study is given in **Appendix A**. A portion of this plate was cut into 610 mm by 305 mm (24-in. by 12-in.) pieces and shipped to both NSWCCD and OSU for determination of temperature-dependent material properties.

### *Chemical Composition*

The chemical composition of the base material was measured at OSU using optical emission spectroscopy in accordance with ASTM E415 [7].

### *Heat Affected Zone Phase Transformation Analysis*

Phase transformations of HSLA-80 as a function of austenitization temperature and cooling rate were assessed via dilatometry. Continuous cooling transformation (CCT) diagrams were developed for four regions of the HAZ that are subject to microstructural transformation during welding: the intercritical region (ICHAZ); the low-temperature, fine-grained region (FGHAZ1); the high-temperature, fine-grained region (FGHAZ2); and the coarse-grained region (CGHAZ).

As part of the DH36 effort [5], the heating and cooling rates were defined by combining typical heat inputs used in the fabrication of DH36 weldments, from 0.4 to 2.6 kJ/mm (10 to 65 kJ/in) as suggested by Ingalls engineers, with numerical simulation of the heat flow using the *SmartWeld* program from Sandia National Laboratories [8]. From these calculations, it was determined that peak temperatures ($T_{peak}$) between 825 and 1350 °C (1517 and 2462 °F), in combination with cooling rates between 1 and 200 °C/s (1.8 and 360 °F/s), would provide information covering a sufficiently broad range of phase transformation behavior relevant to both slowly-cooled welds (*e.g.*, high heat input welds on thin plate) and rapidly-cooled welds (*e.g.*, low heat input welds on thick plate). Because both DH36 and HSLA-80 are low alloy steels, the heating and cooling rates used for HSLA-80 were the same as those for DH36 [5].

In addition to the on-cooling CCT diagram development, this portion of the testing program also involved a detailed assessment of the on-heating austenite transformation as a function of heating rate.

Just as on-cooling transformation temperatures vary with cooling rate, so do the on-heating austenitization temperatures (*i.e.*, $A_{c1}$ and $A_{c3}$). Heating rates between 10 and 2000 °C/s (18 and 3632 °F/s) were used to study these variations. **Table 1** shows the full test matrix utilized for HAZ CCT diagram development.

**Table 1.** Test Matrix for HAZ CCT Diagram Development

| ***Test Type*** | ***Region*** | ***Peak Temperature, °C (°F)*** | ***Heating Rate, °C/s (°F/s)*** | ***Soak Time, s*** | ***Cooling Rate, °C/s (°F/s)*** |
|---|---|---|---|---|---|
| $A_{c1}/A_{c3}$ Determination | N/A | 1200 (2192) | 10 (18)<br>100 (180)<br>200 (360)<br>500 (900)<br>1000 (1800)<br>2000 (3600) | N/A | N/A |
| CCT Diagram Development | ICHAZ | 825 (1517) | 200 (360) | 2 | 1 (1.8)<br>5 (9)<br>10 (18)<br>25 (45)<br>100 (180)<br>200 (360) |
| | FGHAZ1 | 1000 (1832) | | | |
| | FGHAZ2 | 1150 (2102) | | | |
| | CGHAZ | 1350 (2462) | | | |

Execution of this test matrix was performed at NSWCCD using a Gleeble 3500 thermo-mechanical simulation apparatus to apply the prescribed heating and cooling rates. The Gleeble operates on the principles of resistive heating, conductive cooling through water-cooled fixturing, and rapid (50 kHz) control system feedback to apply precise thermal cycles even at rapid heating and cooling rates that cannot be easily achieved by other apparatus. The Gleeble 3500 system, in combination with the apparatus's standard 'Pocket Jaw' setup, used full contact copper grips and 70 mm (2.76-in.) long specimens with 3 mm (0.118-in.) diameters. A linear variable differential transformer (LVDT)-type contact extensometer was used to measure diametric dilation of the specimens during heating and cooling. All dilatometry specimens were extracted perpendicular to the rolling direction of the plate, and all dilatometry tests were performed in an argon atmosphere. The typical experimental setup for the dilatometry testing is shown in **Figure 1.**

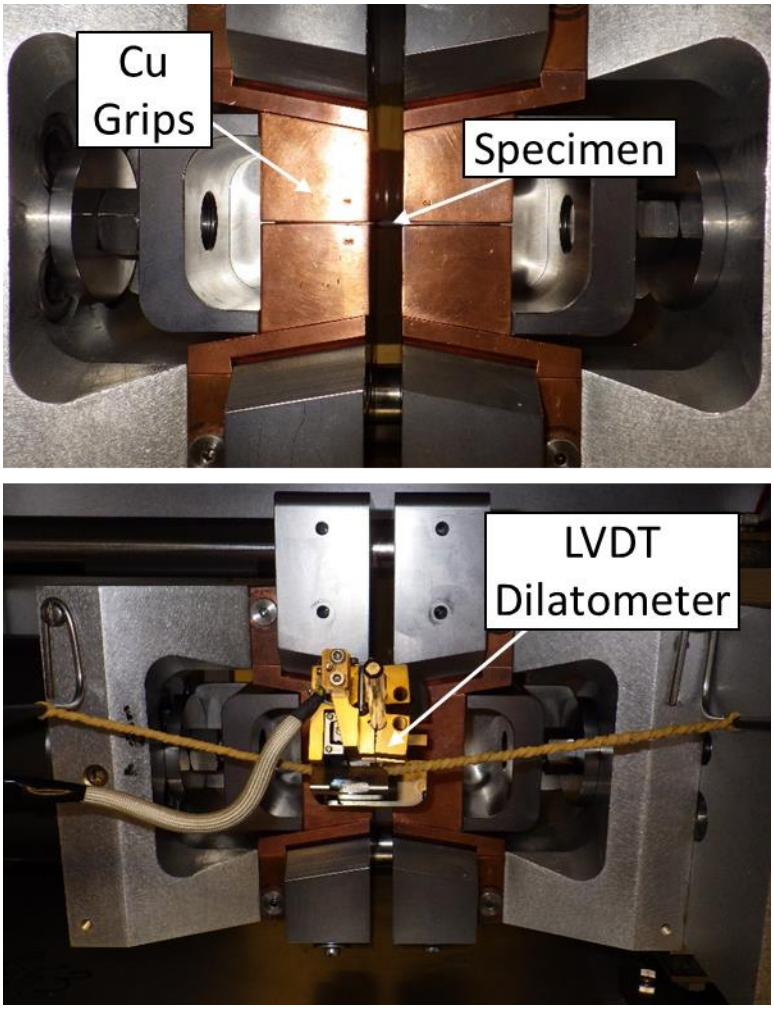


**Figure 1.** Photographs of the Gleeble-based dilatometry experimental set-up.

***Thermo-Physical Property Analysis***

Specimens were sent to the Thermophysical Properties Research Laboratory, Inc. (TPRL) in West Lafayette, IN for analysis of thermal diffusivity ($\alpha$) and specific heat ($C_p$). Thermal diffusivity was measured using the laser flash method according to ASTM E1461 [9]. Specific heat was measured using differential scanning calorimetry (DSC) methods according to ASTM E1269 [10]. Coefficient of thermal expansion (CTE) was measured from the on-heating Gleeble dilatometry data in two regimes: 150 to 650 °C (302 to 1202 °F) for the base material microstructure, and 1000 to 1300 °C (1832 to 2192 °F) for austenite. No attempt was made to determine CTE during the on-heating transformation. CTE calculations were either performed by linear fitting or by discrete analysis using the dilation data endpoints from each temperature range in conjunction with **Equation 1**. The material was assumed to be isotropic.

$$\alpha_T = \left(\frac{\Delta d}{d_0}\right)\left(\frac{1}{\Delta T}\right) \quad \textbf{(1)}$$

where $\alpha_T \equiv$ Linear coefficient of thermal expansion [°C$^{-1}$]
$\Delta d \equiv$ Change in specimen diameter over the chosen temperature range [cm]

$d_0$ ≡ Initial specimen diameter [cm]
$\Delta T$ ≡ Temperature range [°C]

The temperature-dependent density ($\rho$) was calculated using a theoretical cubic volume element under the assumption of isotropic thermal expansion:

$$\rho(T) = \frac{\rho_0 V_0}{V(T)} \quad \textbf{(2)}$$

where $\rho(T)$ ≡ Density at temperature $T$ [g/cm$^{-3}$]
$\rho_0$ ≡ Room temperature density provided by TPRL [g/cm$^3$]
$V_0$ ≡ Room temperature volume of the theoretical cubic element [cm$^3$]
$V(T)$ ≡ Volume of the theoretical cubic element at temperature $T$ [cm$^3$]

$V_0$ was calculated assuming a side length equal to the room temperature width of the dilatometry specimens. This value was chosen because, as shown in **Figure 1**, it corresponds to the starting gauge length for the dilatometer used to measure thermal expansion. A theoretical cubic volume element was chosen instead of the actual specimen dimensions to subvert potential complications with measuring dimensions that were not directly measured by the dilatometer (*e.g.*, the effect of thermal gradients on measurement of the specimen's longitudinal expansion). $V_T$ was simply calculated by:

$$V(T) = [w(T)]^3 \quad \textbf{(3)}$$

where $w(T)$ ≡ Dilatometer-measured specimen width at temperature $T$ [cm]

This method allowed calculation of the density through the austenite transformation. Finally, thermal conductivity ($\lambda$) as a function of temperature was calculated using **Equation 4**:

$$\lambda = \rho \cdot c_p \cdot \alpha \quad \textbf{(4)}$$

where $\lambda$ ≡ Thermal conductivity [W/cm-°C]
$c_p$ ≡ Specific heat capacity [J/g-°C]
$\rho_0$ ≡ Room temperature density [g/cm$^3$]
$\alpha$ ≡ Thermal diffusivity [cm$^2$/s]

### *Thermo-Mechanical Property Analysis*

Tensile specimens were machined from the HSLA-80 plates according to the dimensions shown in **Figure 2a**. All specimens were extracted with their length perpendicular to the rolling direction of the plate. On-heating tension testing of the HSLA-80 base material at temperatures between 22 and 1100 °C (72 and 2012 °F) was performed at IMR Test Labs in Portland, OR. Room temperature testing was performed in accordance with ASTM A370 [11], and elevated temperature testing was performed in accordance with ASTM E21 [12]. Specimens were of rectangular cross-section with 12.7 mm (0.50 in.) gauge width and approximately 50.8 mm (2.0 in.) gauge length. Testing was performed in strain control mode at target rates of 0.005 min$^{-1}$ prior to yield and 0.05 min$^{-1}$ after yield.

Elevated temperature HAZ mechanical properties were measured using the Gleeble 3500 at NSWCCD. Prior to mechanical testing, the specimens were thermally cycled to generate different initial microstructures based on the results of the CCT diagram development described above. For HSLA-80, microstructural analysis indicated that substantially different microstructures formed when the material

was cooled at 1, 10, 25, and 100 °C/s (1.8, 18, 45, and 180 °F/s). Because of programmatic time constraints, only a peak temperature of 1350 °C (2462 °F) was applied to the tensile specimens. All specimens were heated in an argon atmosphere, and forced air was used to meet cooling rates of 10 °C/s (18 °F/s) and above. All specimens were cooled to room temperature, and thereafter a longitudinal extensometer was affixed. The specimens were then reheated to the test temperature at a rate of 10 °C/s (18 °F/s) and soaked for 10 seconds before being pulled to failure in crosshead control mode at strain rates targeting those prescribed in ASTM E21 [12]. The crosshead displacement rate used was 0.30 mm/min (0.012 in/min). It is acknowledged that this is not the most representative method of mechanical testing for welding-related applications because the stresses that develop during welding do so rapidly and while the material is cooling and undergoing phase transformations. However, given the programmatic intent of establishing the mechanical behavior of specific microstructures and the need to avoid exposing the strain measurement device to dangerously elevated temperatures, the method of cooling to room temperature and tension testing after reheating was determined to be an acceptable compromise. In cases where the induced microstructure was stronger than the base material, a second reduced gauge section was machined in the specimen prior to testing to ensure specimen fracture in the region of interest. This revised specimen geometry is shown in **Figure 2b**.

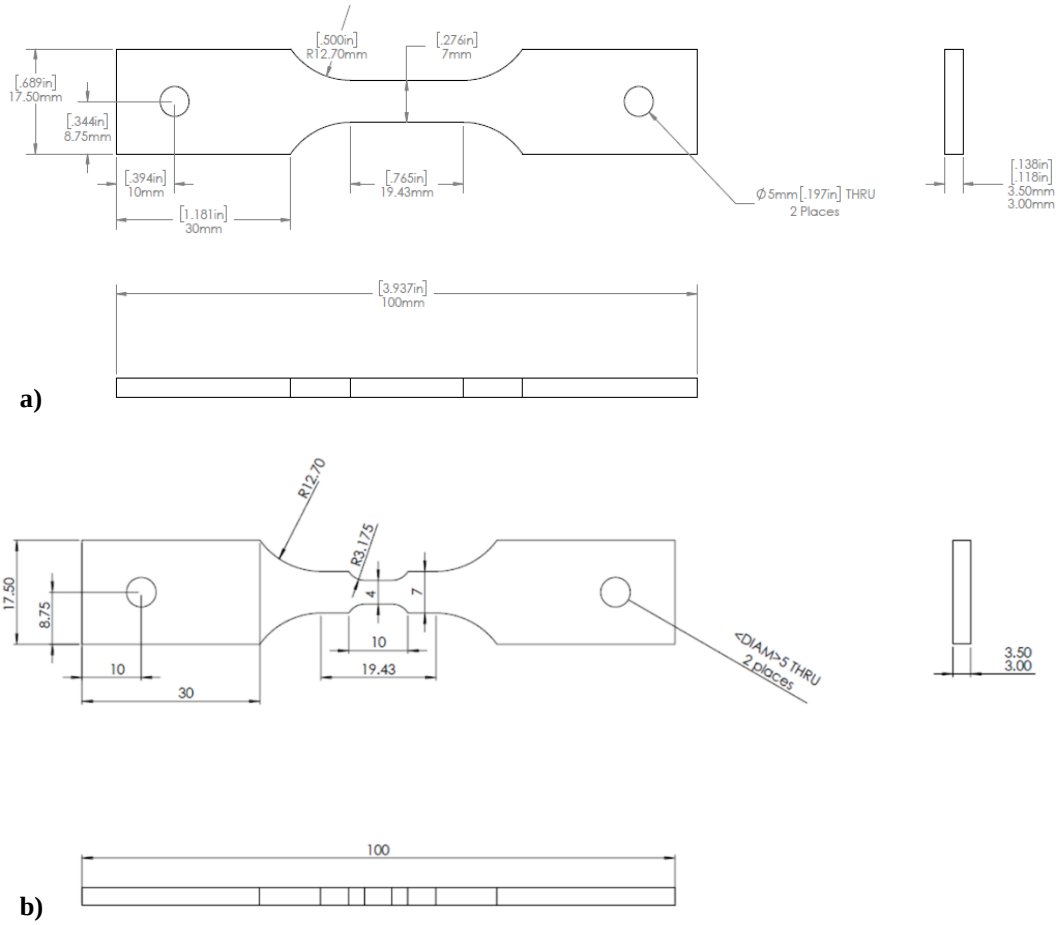


**Figure 2.** Specimen dimensions for Gleeble-based mechanical testing of HSLA-80 steel: **a)** single-reduced gauge section, **b)** double-reduced gauge section (dimensions in mm).

Thermal cycling and subsequent tensile testing were performed using the 'Pocket Jaw' setup with minimal-contact stainless steel grips used to fixture the specimen. These grips were selected to minimize

the longitudinal thermal gradient in the gauge length of the specimens during testing. Graphite foil was inserted between the specimen and the grips to further minimize the thermal gradient. Preliminary testing as part of the DH36 test program [5] indicated that for this setup, the temperature variation across the initial gauge length was 10 to 30 °C (18 to 54 °F). Strain in the specimens was measured using a longitudinal extensometer, and the initial gauge length for the tests varied between 8 and 10 mm (0.31 and 0.39 in.). Elevated temperature tension tests were performed in an argon atmosphere. The typical experimental setup for the tensile testing is shown in **Figure 3**.

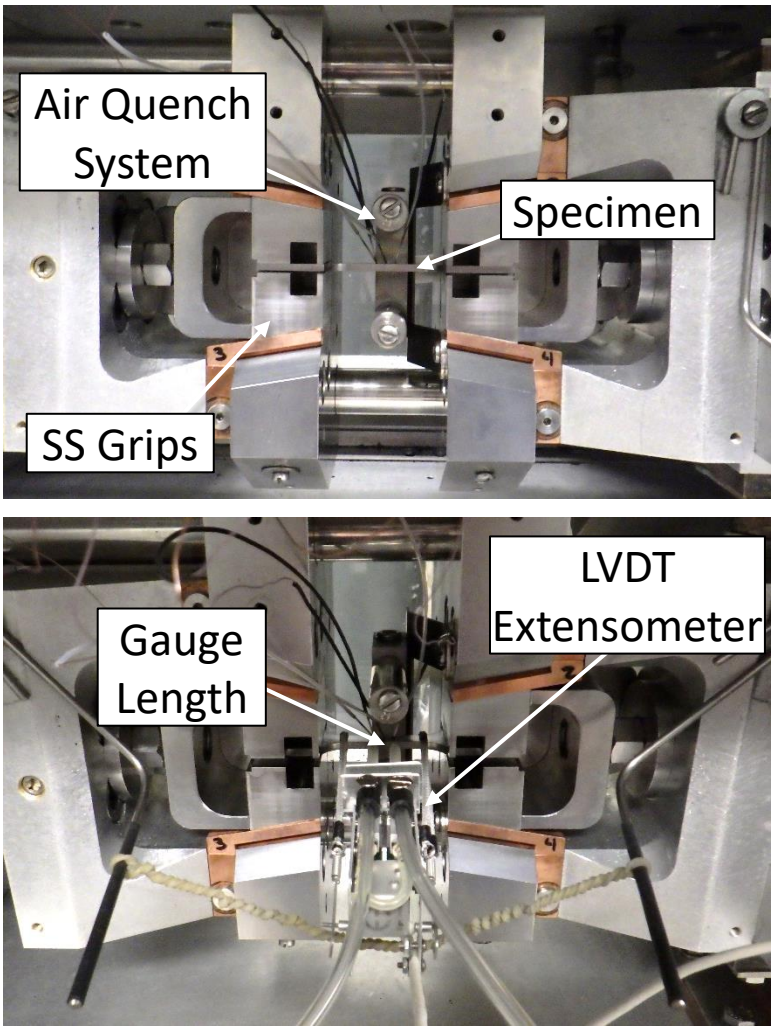


**Figure 3.** Photographs of the Gleeble-based mechanical testing experimental set-up.

### *Fabrication of Welded Specimens*

Two sets of HSLA-80 plates were welded together at HII-Ingalls and sent to OSU for investigation of the base material, weld metal, and heat-affected zone (HAZ) microstructures. The first set of plates were welded using submerged arc welding (SAW) in a two-sided butt joint configuration, as shown in **Figure 4a**. The second set of plates were welded using flux cored arc welding (FCAW) in a two-sided tee-joint configuration, as shown in **Figure 4b**. Welding parameters for both joints are given in **Table 2**. These weldments are representative of two primary types of joints used at HII-Ingalls for structural welds: seaming butt joints and fillet joint stiffener welds. These joint types were also the focus of larger fabrication efforts described in other tasks within the greater LIFT project as described in [13].

The weldments enabled correlation of the microstructures generated through thermal simulations for the CCT curves with those produced by arc welding.

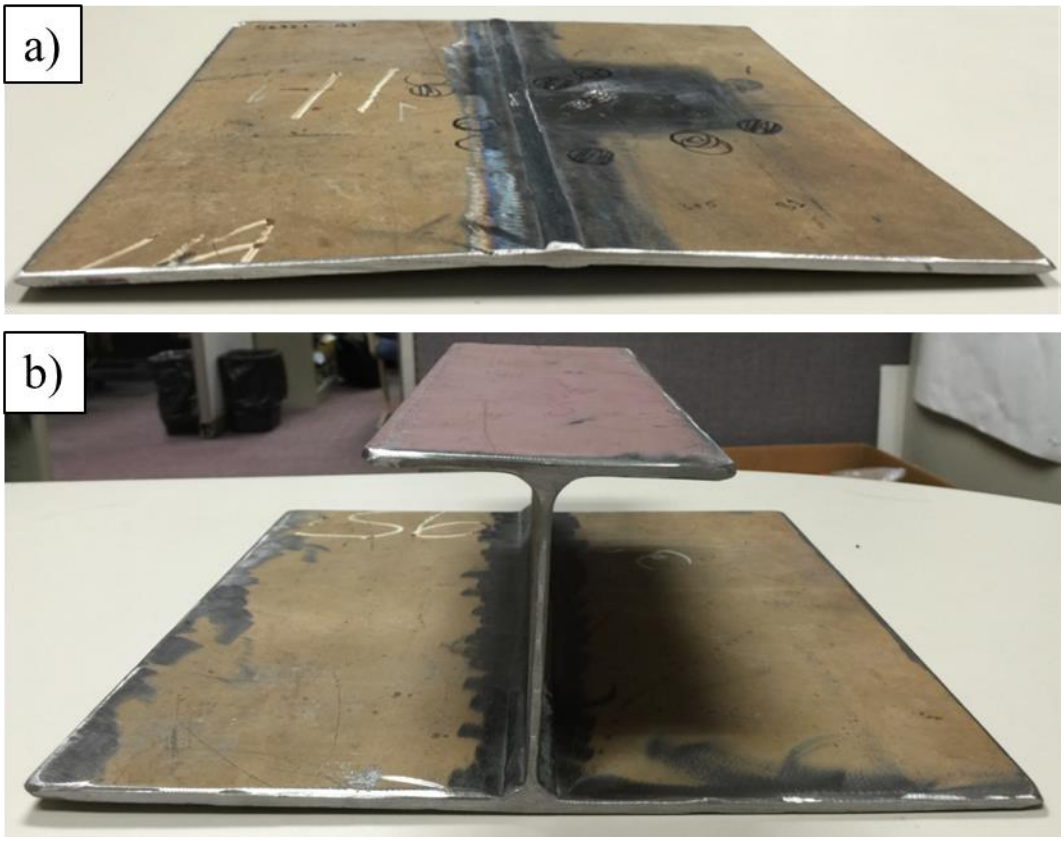


**Figure 4.** Representative **a)** butt and **b)** tee joint weldments investigated for plate, weld, and HAZ microstructures. Photos are for illustrative purposes only as they show weldments of DH36 material [5], though the same joint configurations were used for the HSLA-80 specimens.

**Table 2.** Nominal Welding Parameters Used to Fabricate HSLA-80 Butt and Tee Joints

| | **Butt Joint** | **Tee Joint** |
|---|---|---|
| **Welding Process** | Submerged arc (SAW) | Flux cored arc (FCAW) |
| **Current (A)** | 300 | 200 |
| **Voltage (V)** | 30 | 27 |
| **Travel Speed (mm/s [in/min])** | 14.8 (35) | 6.8-7.6 (16-18) |
| **Heat Input (kJ/mm [kJ/in])** | 0.61 (15.4) | 0.71-0.79 (18-20.3) |
| **Consumable Designation** | AWS A5.23 EM12K | AWS A5.20 E71T-1 |
| **Filler Wire Diameter (mm [in])** | 3.2 (0.125) | 1.3 (0.052) |
| **Interpass Temperature, Max. (°C [°F])** | 149 (300) | 149 (300) |

***Microstructural Analysis***

To quantify and characterize the HSLA-80 weldment microstructures, a cross-section of each of the weldments represented in **Figure 4** was analyzed. Each specimen was metallographically prepared to a final polish of 0.05 μm using standard techniques and etched by immersion in 4% Picral (4 g picric acid dissolved in 100 mL ethanol) for approximately 10 seconds followed by immersion in 2% Nital (2 mL nitric acid in 100 mL of ethanol) for 3-5 seconds. Metallographic preparation was followed by light optical microscopy (LOM) and scanning electron microscopy (SEM) analysis. Vickers microhardness values measured using a load of 200 g (7.05 oz.) were taken from the fusion zone through the HAZ to the base material for both weldments.

Thermally-cycled specimens from the HAZ CCT diagram development were metallographically prepared using the same procedure. Identification and phase fraction measurement of the microstructural constituents in each specimen were performed using analysis of LOM and SEM micrographs. Vickers microhardness testing was also used to determine the hardness of the constituent(s) in each CCT specimen. This analysis facilitated proper CCT analysis, provided phase fraction input for the HSLA-80 material property database, and helped determine which thermal cycles were the most appropriate for application in the mechanical testing portion of the program described in the previous section.

# RESULTS AND DISCUSSION

## Chemical Composition

**Table 3** shows the averaged results of three base material chemistry measurements for the HSLA-80 plate, plus the manufacturer's plate certification values (shown in **Appendix A**), the NAVSEA Tech Pub 300 HSLA-80 specifications [4], and results from a study conducted as part of a Navy Manufacturing Technology (ManTech) program with the Naval Metalworking Center from the mid-2000s [14]. Hereafter, data from the ManTech study are labeled "CTC" for Concurrent Technologies Corporation, where the testing was conducted. Plate material used in that study was nominally 19.05 mm (0.75-in) thick. As expected, the measured chemical compositions generally agreed with the manufacturer's plate certification and were well within Tech Pub 300 requirements. The carbon equivalent (CEN) was calculated according to Yurioka [15]. The individual measurements made by OSU to obtain the average composition values are located in **Appendix A**.

## Base Metal Microstructure

The microstructure of the HSLA-80 base metal is shown in the light optical micrograph of **Figure 5**. The microstructure is entirely quasipolygonal ferrite. As the base metal was subjected to a precipitation aging heat treatment by the manufacturer, the presence of ε-Cu precipitates is presumed, but they could not be resolved via LOM. The average Vickers microhardness of the base metal was 246 ± 8.2 $HV_{200}$.

Observing the HSLA-80 base metal in both the longitudinal and transverse planes revealed irregular grains with no significant evidence of rolling texture. The grain size was measured using the "intercept method" detailed in ASTM E1382 [16]. Using this technique, a circle is drawn at random locations within a micrograph, and the number of times a grain boundary intercepts that circle is used to calculate the average grain size. Using a circle instead of a line ensured that rolling texture that may have been present would not bias results. Measurements were taken three times on a sample of base metal with the average ASTM grain size calculated to be G = 13.2.

**Table 3.** Chemical Composition of HSLA-80 Plate (wt.%)

| Type | C | Mn | P | S | Si | Ni | Cr | Mo | Cu |
|---|---|---|---|---|---|---|---|---|---|
| **Measured Avg.** | 0.040 | 0.56 | 0.011 | 0.001 | 0.26 | 0.90 | 0.67 | 0.20 | 1.11 |
| **Plate Certificate** | 0.04 | 0.56 | 0.011 | 0.004 | 0.26 | 0.85 | 0.70 | 0.20 | 1.17 |
| | 0.04 | 0.58 | 0.012 | 0.004 | 0.27 | 0.88 | 0.70 | 0.20 | 1.18 |
| **Tech Pub 300** [4] | ≤0.06 | 0.40 – 0.70 | ≤0.020 | ≤0.004 | ≤0.40 | 0.70-1.00 | 0.60-0.90 | 0.15-0.25 | 1.00-1.30 |
| **CTC** [14] | 0.05 | 0.64 | 0.009 | 0.022 | 0.2 | 0.95 | 0.85 | 0.2 | 1.23 |

| Type | Nb | Al | Ti | As | Sb | V | Sn | N | Fe | CEN [15] |
|---|---|---|---|---|---|---|---|---|---|---|
| **Measured Avg.** | 0.030 | 0.036 | 0.001 | 0.005 | 0.023 | 0.003 | 0.011 | 0.010 | Bal. | 0.252 |
| **Plate Certificate** | 0.027 | 0.032 | 0.001 | 0.0030 | 0.0020 | 0.002 | 0.009 | 0.0082 | Bal. | 0.253 |
| | 0.030 | 0.033 | 0.001 | 0.0030 | 0.0020 | 0.002 | 0.010 | 0.0080 | Bal. | 0.257 |
| **Tech Pub 300** [4] | 0.02-0.06 | ≥0.015 | ≤0.02 | ≤0.025 | ≤0.025 | ≤0.03 | ≤0.03 | --- | Bal. | --- |
| **CTC** [14] | 0.04 | 0.01 | --- | --- | --- | <0.01 | --- | --- | Bal. | 0.295 |


**Figure 5.** Representative micrograph of HSLA-80 steel plate base metal microstructure at 1000x magnification using LOM.

## Heat Affected Zone Phase Transformation Analysis

### *Dilation Curve Analysis Method*

**Figure 6** shows a representative on-heating portion of a Gleeble-produced dilatometry curve. The black curve (left axis) represents the change in sample diameter with temperature, and non-linearity in the curve is indicative of a phase transformation's occurrence. Two methods are commonly used for extracting start and finish temperatures for phase transformations from Gleeble dilatometry data. The first

method involves superimposing a straight line of matching slope along the low temperature portion of the dilation curve and extrapolating it past the transformation. The point at which the experimental data begins to deviate from the straight line is then taken as the transformation start temperature. The same technique is then used to find the transformation finish temperature, with the straight line being extrapolated from the high-temperature portion of the curve after the transformation. The second method involves calculating and plotting the derivative of the dilation curve. Then the points at which the derivative begins to deviate from a constant value are taken as the transformation start and finish temperatures. Both methods for determining phase transformation temperatures are inherently somewhat subjective, and both also have advantages and disadvantages. The linear extrapolation method is faster and easier to interpret but is difficult to use when multiple transformations occur. The derivative method is more quantitative and can more easily distinguish multiple transformations but can be difficult to interpret when the dilation data is noisy. For this work, the linear extrapolation method was chosen as the primary method of data analysis, and the derivative method was used as a complementary technique for distinguishing concurrent phase transformations. Both methods are shown in **Figure 6**, wherein the transformation of interest is that of the HSLA-80 base metal microstructure to austenite. The derivative curve is displayed in red (right axis) and the linear extrapolations are displayed in blue.

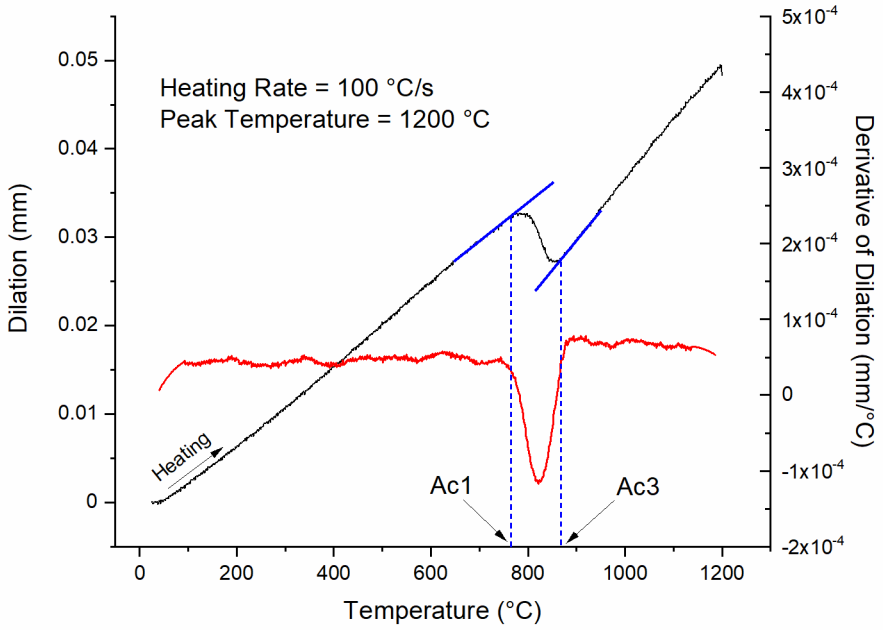


**Figure 6.** Representative on-heating dilatometry curve for HSLA-80 steel, showing the linear extrapolation and derivative curve methods for evaluating the ferrite to austenite reaction. Black curve, left axis: dilation data. Red curve, right axis: derivative of dilation data. Blue lines: extrapolation lines for determining transformation start ($A_{c1}$) and finish ($A_{c3}$) temperatures.

***Austenite Transformation Temperature Measurement***

**Figure 7** presents the variation in austenite transformation behavior as a function of heating rate for HSLA-80 base material. As shown, the austenite transformation start temperature ($A_{c1}$) increases significantly as heating rate increases toward 200 °C/s (360 °F/s). This is a consequence of thermal diffusion during increasingly rapid heating outpacing the mass diffusion required for the transformation to take place. In contrast, the austenite transformation finish temperature ($A_{c3}$) remains more stable across the experimental heating rate range. Researchers who have investigated similar behavior in other ferrous

materials have associated heating rate dependencies of the austenite transformation with those of the controlling diffusion mechanism (*i.e.*, volume carbon diffusion or grain boundary substitutional element diffusion), the ferrite recrystallization process, and/or austenite nucleation and growth rates [17] [18] [19]. These data are important for the refinement of welding simulation results because different regions of a weldment and its HAZ are subject to significantly different heating rates during the welding process. Thus, the on-heating transformation behavior must be incorporated in order to accurately predict which areas around the weld will transform to austenite, and will therefore be subject to re-transformation (and associated changes in mechanical properties and residual stresses) during cooling. Data from CTC as part of the Navy ManTech program are included for comparison [14]. The raw data points for **Figure 7** can be found in **Table 9** within **Appendix B**.

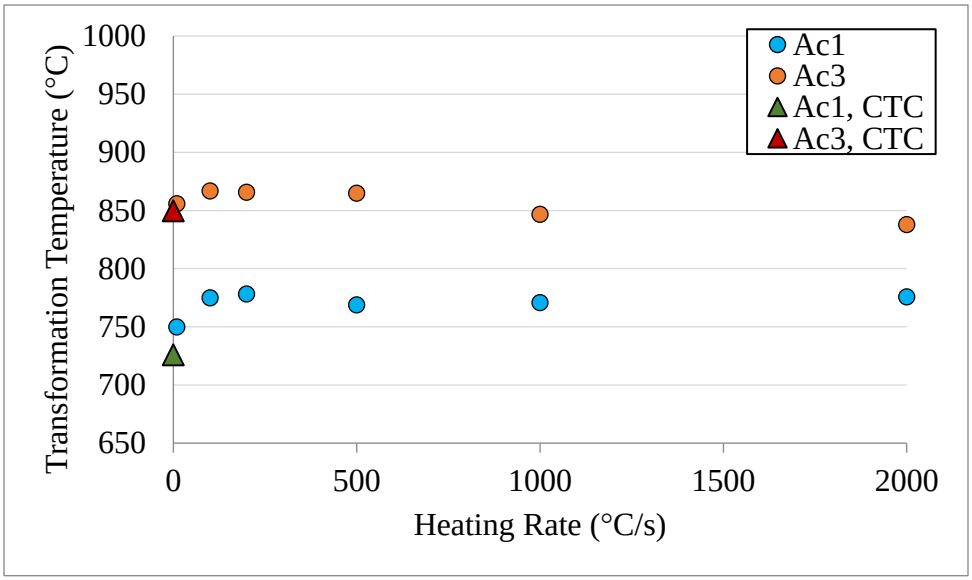


**Figure 7.** Variation in austenite transformation start and finish temperatures with heating rate for HSLA-80 material. CTC data from [14].

***Continuous Cooling Transformation Diagrams***

On-cooling, solid-state phase transformation temperatures and products in steels can vary substantially with peak temperature due to differences in austenite grain size at different peak temperatures [20] [21] [22] [23]. It was therefore expected that each of the investigated HAZ regions would produce slightly different CCT diagrams. The residual stress (and subsequent distortion) that develops during weld cooling is greatly influenced by: 1) the microstructure that forms on cooling and 2) the temperature difference between the end of the on-cooling transformations and the final temperature of the component. Thus, full analysis must include as much HAZ phase transformation behavior as possible in order to provide the most complete and accurate material database for welding simulations.

CCT diagrams assembled from dilatometry of HSLA-80 thermally cycled to peak temperatures representative of the four selected HAZ regions are given in **Figures 8-11**. The austenite transformation temperatures described above allowed for use of an ICHAZ simulation temperature of 825 °C (1517 °F) for HSLA-80, which was the same as that used for HSLA-65 [6] but 50 °C (90 °F) lower than the temperature used for DH36 [5]. The $A_{c1}$ and $A_{c3}$ temperatures labeled on the CCT diagrams are averages calculated from the individual $A_{c1}$ and $A_{c3}$ values for all of the CCT specimens. The black curves are the actual specimen cooling curves. The target cooling rates for all specimens except those cooled at 100 and 200 °C/s (180 and 360 °F/s) were maintained through the on-cooling phase transformations. The latent

heat released during low temperature transformation slowed the cooling rates of both the 100 °C/s (180 °F/s) and the 200 °C/s (360 °F/s) tests with peak temperatures of 1150 and 1350 °C (2102 and 2462 °F). As a result the target cooling rate was maintained until the start of the transformation, but was slowed as the transformations occurred for samples cooled at 100 and 200 °C/s (180 and 360 °F/s). The raw data for these figures are given in **Tables 10-13** of **Appendix B**, and the individual dilation curves are given in **Figures 38-61** of **Appendix B**.

The colored symbols in **Figures 8-11** correspond to the start and finish temperatures for the various on-cooling phase transformations. Three regimes of on-cooling transformation start temperatures were observed across the cooling rate range assessed in this work. The first, associated with ferrite, occurred at high temperatures (567 to 761 °C [1053 to 1402 °F]) and is denoted in **Figures 8-11** by blue square symbols. The start of this transformation generally occurred near $A_{c1}$, though it decreased with increasing peak temperature and increasing cooling rate. The second type of transformation identified is indicated by green triangle symbols, representing the bainite transformation. This transformation started from 38 to 78 °C (100 to 172 °F) below the start of the higher temperature transformation, with the difference in temperatures dropping as peak temperature increased. The third transformation product identified in the CCT diagrams, indicated as orange triangle symbols, generally started forming at temperatures of 472 to 498 °C (882 to 928 °F) and was only observed at cooling rates of 25 °C/s (45 °F/s) and higher. The association of this transformation with high peak temperatures indicates that this transformation product is influenced by precipitate dissolution and prior austenite grain (PAG) size. Identification of these transformations is discussed in more detail below, but for interpretation of the diagrams presented in **Figures 8-11**, the blue, green, and orange symbols reflect ferrite, bainite, and martensite transformations, respectively.

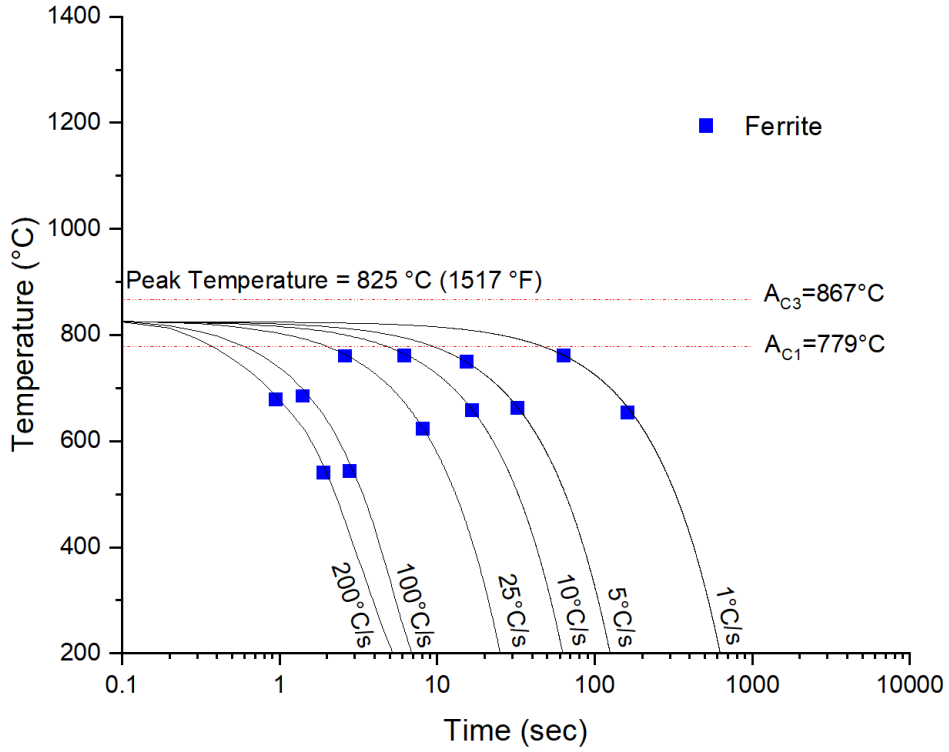


**Figure 8**. CCT diagram for HSLA-80 heated to peak temperature of 825 °C (1517 °F).

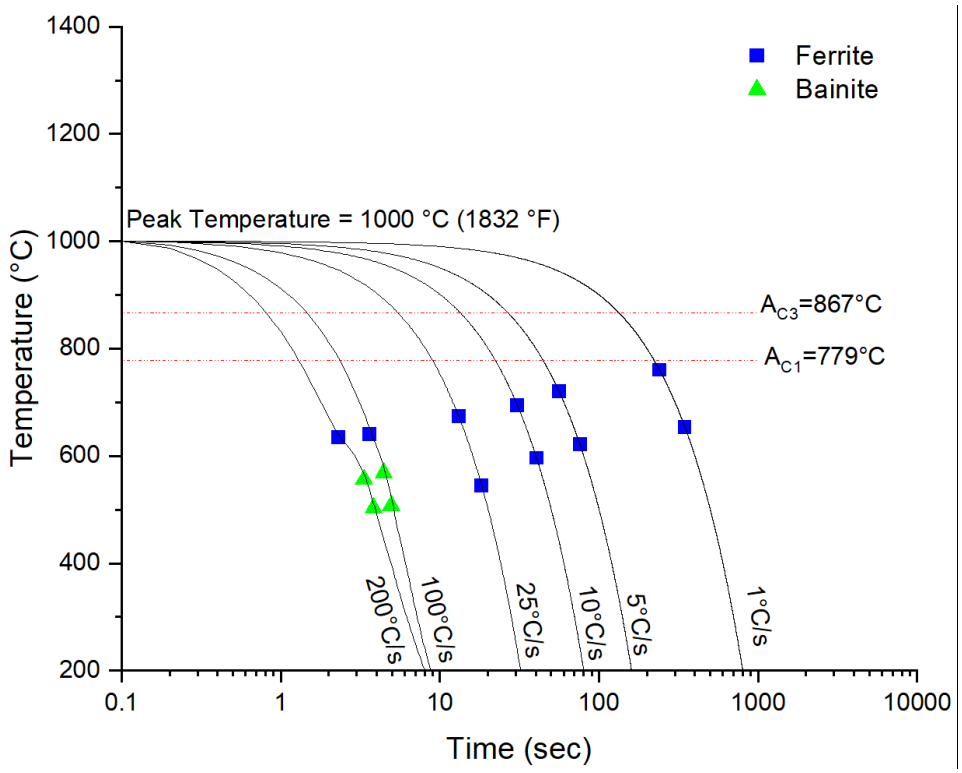


**Figure 9.** CCT diagram for HSLA-80 heated to peak temperature of 1000 °C (1832 °F).

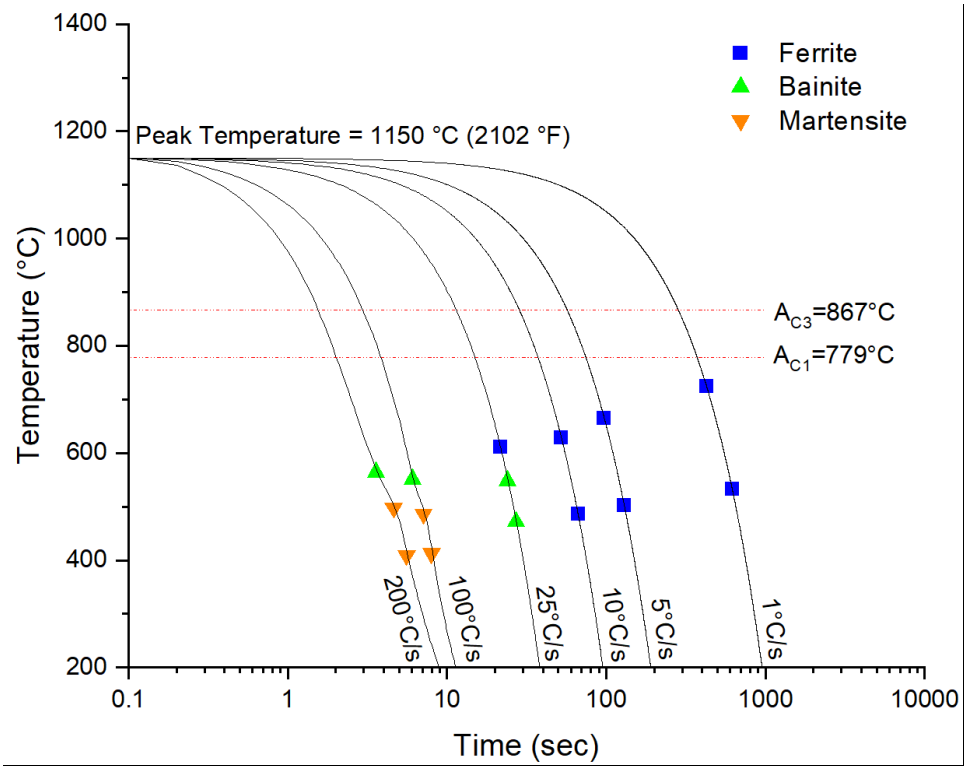


**Figure 10.** CCT diagram for HSLA-80 heated to peak temperature of 1150 °C (2102 °F).

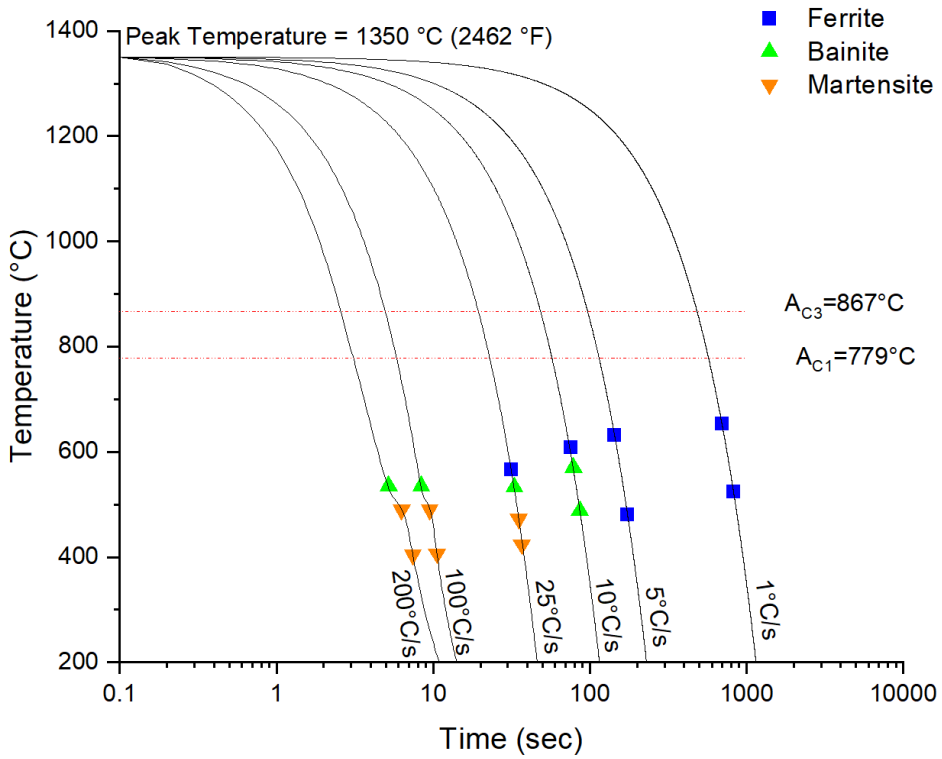


**Figure 11.** CCT diagram for HSLA-80 heated to peak temperature of 1350 °C (2462 °F).

The effects described above are summarized in an alternate way in **Figures 12-14**. **Figure 12** gives the variation in transformation start temperature for the ferrite transformation as a function of peak temperature and cooling rate. As shown, for a given cooling rate, increasing the peak temperature generally suppresses the onset of the transformation, resulting in lower start temperatures. This most likely occurs because PAG size increases with increasing peak temperature, resulting in less grain boundary area and therefore fewer nucleation sites for transformation. For each cooling rate, transformation start temperatures decreased by an average of 48 ± 23 °C (118 ± 73 °F) when compared to the temperature associated with the next highest peak temperature. The onset of transformation is additionally suppressed by undercooling as cooling rate is increased. As a result, transformation start temperature decreased by an average of 26 ± 23 °C (79 ± 74 °F) for each step in cooling rate tested.

**Figure 13** shows that the bainite transformation start temperature did not vary substantially with either peak temperature or cooling rate. All transformation start temperatures fell within the range of 533 to 570 °C (991 to 1058 °F). It was expected that the bainite transformation temperatures would follow similar trends to those observed for the ferrite transformation, but the small dataset makes trends difficult to confirm.

**Figure 14** shows how the measured transformation behavior for martensite varied. As was the case for bainitic transformation temperatures, the small sample size did not reveal any strong trends associated with peak temperature. Transformations for samples cooled at or above 100 °C/s (180 °F/s) began in the range of 486-498 °C (907-928 °F). The specimen heated to a peak temperature of 1350 °C (2462 °F) and cooled at 25 °C/s (45 °F/s) had a slightly lower transformation start temperature of 472 °C (882 °F). This may be due to the formation of primary ferrite, which was not observed in the more rapidly cooled samples. The low solubility of carbon in ferrite would have enriched the remaining austenite in carbon prior to transformation, thereby stabilizing it to lower temperatures.

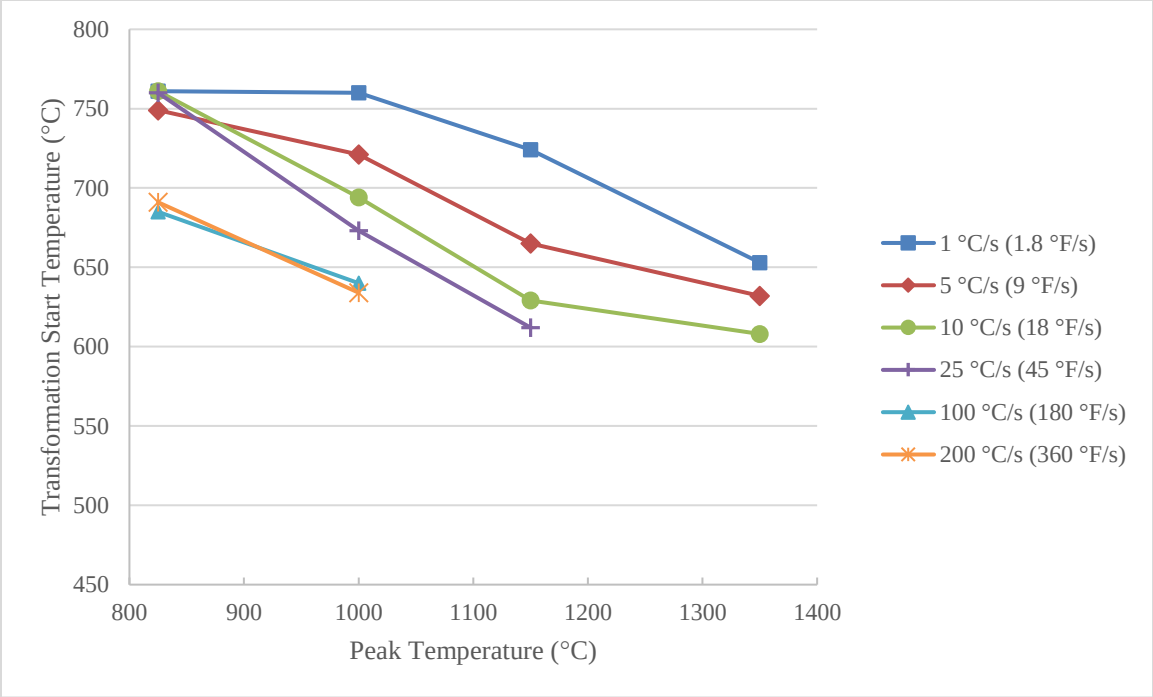


**Figure 12.** Variation of start temperature for the ferrite transformation shown in **Figures 8-11**.

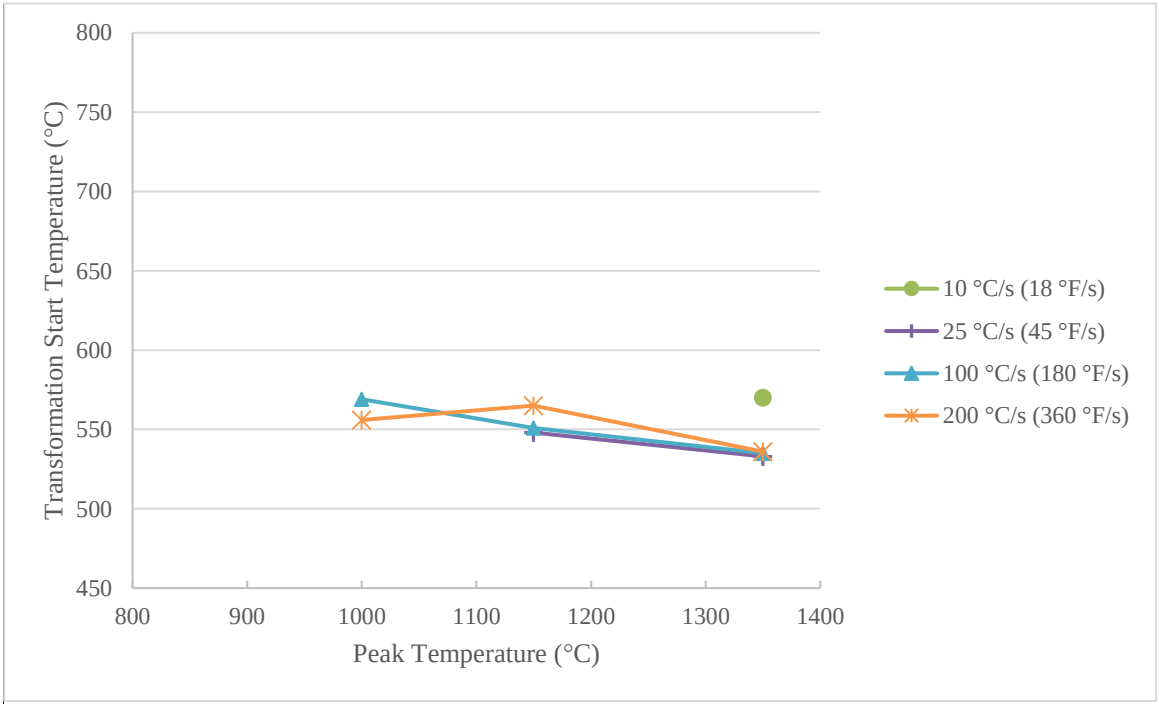


**Figure 13.** Variation of start temperature for the bainite transformation shown in **Figures 8-11**.

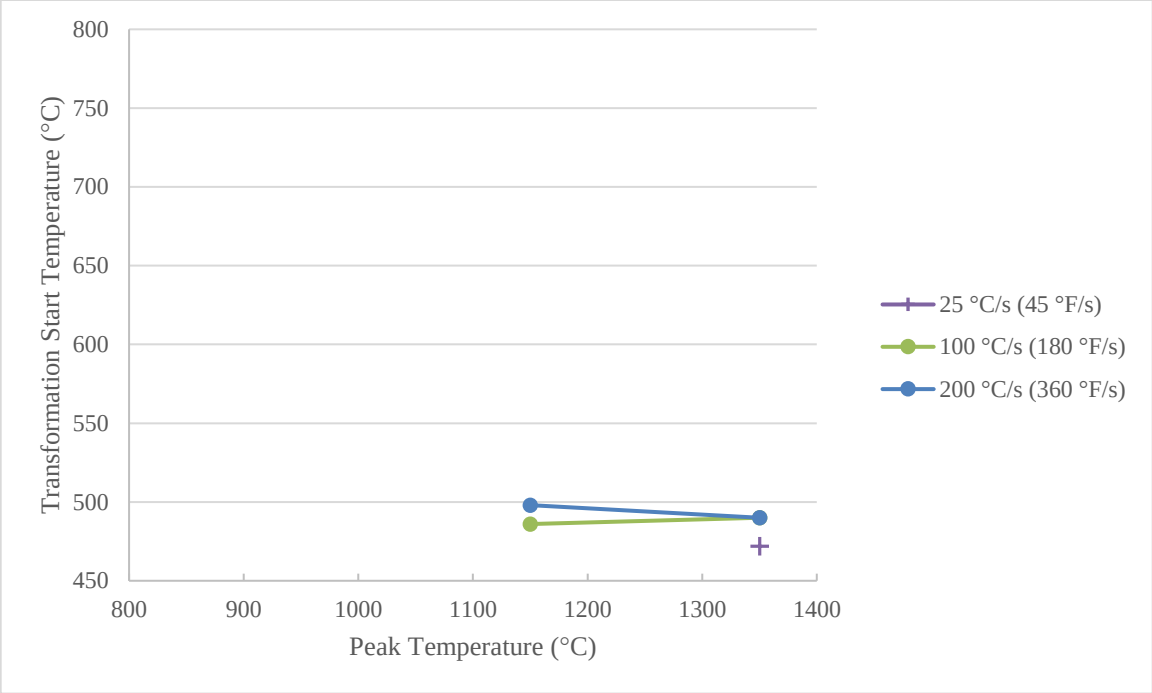


**Figure 14.** Variation of start temperature for the martensite transformation shown in **Figures 8-11**.

In order to confidently establish the identities of the on-cooling phase transformations, LOM was performed on all dilatometry specimens, and select specimens were analyzed via SEM. Micrographs collected from the dilatometry specimens are given in **Figures 62-67** of **Appendix C**. Additionally, the measured microhardness for each specimen is given in **Figure 15** below and **Table 14** of **Appendix D**. For this discussion, the following definitions for the morphology of microstructural constituents are adopted [24] [25] [26] [27] [28]. The typical definitions for crystal structure and composition of the constituents are assumed.

*Primary ferrite ($F_P$)* – Carbide-free grain boundary or intragranular allotriomorphic or idiomorphic ferrite, encompassing polygonal and quasipolygonal morphologies
*Acicular ferrite (AF)* – Fine, interlocking structure formed by impingement of multiple Widmanstätten plates growing from intragranular inclusions
*Martensite-austenite constituent (M/A)* – Structure represented by a combination of martensite and residual austenite
*Bainite (B)* – General term for fine aggregates of ferrite laths or plates and cementite particles
*Lath martensite ($M_L$)* – Martensite laths with highly dislocated substructure which are grouped into larger packets

Representative micrographs of all CCT specimens heated to 825 °C (1517 °F) are shown in **Figures 62-63** of **Appendix C**. This peak temperature falls between $A_{c1}$ and $A_{c3}$ (779 and 867 °C [1434 and 1593 °F], respectively) in order to achieve partial transformation to austenite prior to cooling. This partial transformation is expected to occur via austenite nucleation at the triple points and grain boundaries as the ferrite solvus temperature is exceeded [26].

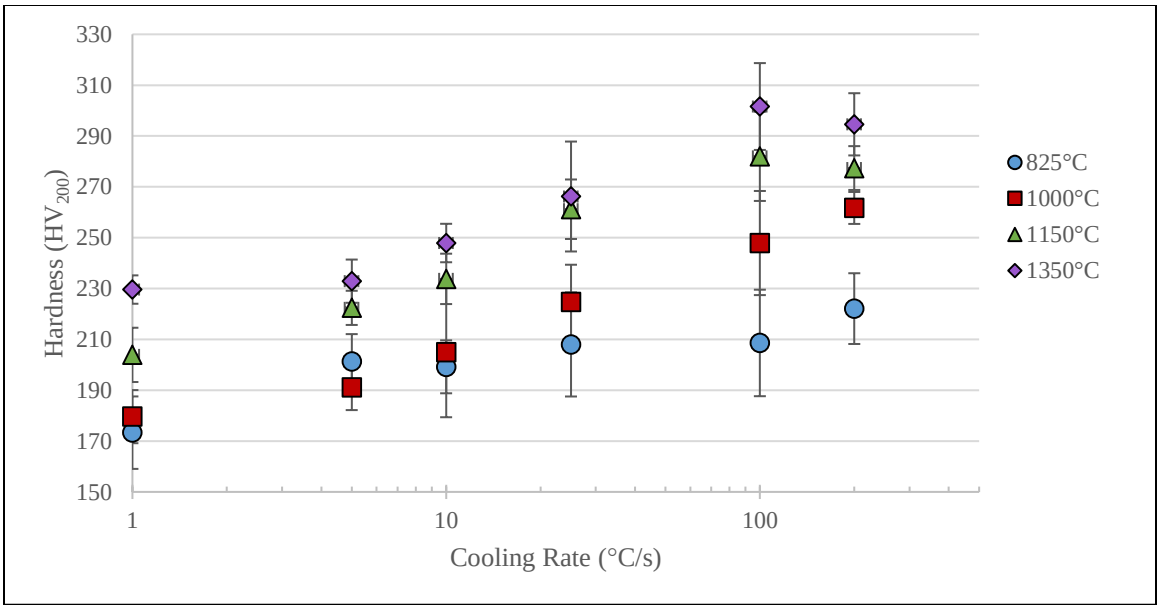


**Figure 15.** Measured Vickers microhardness for HSLA-80 dilatometry specimens as a function of peak temperature and cooling rate. Error bars are one standard deviation. Values are the average of 10 indents. Data is tabulated in **Table 14**.

Slowly cooled samples did not retain microstructures from the original base material. The samples subjected to 1, 5, 10, and 25 °C/s (1.8, 9, 18, and 45 °F/s) cooling rates (shown in **Figure 62a-d**) all exhibited a mixture of primary ferrite with quasipolygonal morphology and M/A constituent. The proportions of martensite and austenite in the M/A constituents could not be determined through optical or electron microscopy. Additionally, ε-Cu precipitates in HSLA-80 have been reported to be less than 5 nm (2 x $10^{-7}$-in.) in size, so observation of changes to these precipitates during HAZ thermal cycling was not within the scope of microscopy in this work. Any volumetric change associated with ε-Cu dissolution was not large enough to identify on dilation curves. For HSLA-80, the dissolution of second phases including ε-Cu was determined in CTC tests to finish at 880 °C (1616 °F) at slow heating rates [14]. Further, a study by Bhagat *et al.* indicated that under isothermal aging conditions, dissolution of copper precipitates in an HSLA steel sample began at 650 and 700 °C (1202 and 1292 °F) after being held for 20 and 4 minutes, respectively, as evidenced by an increase in experimentally measured resistivity [29]. The sample studied by Bhagat *et al.* had a composition that was similar to that of HSLA-80, but the Ni content of 3.39 wt.% fell well outside the range of 0.70-1.00 wt.% specified by Tech Pub 300 [4]. Mn, Cr, Mo, and Cu were also slightly higher than the respective allowable ranges for HSLA-80. Thermo-Calc 2020b and the TCFE9 database were used in this study to calculate an ε-Cu dissolution temperature of approximately 730 °C (1346 °F) for the HSLA-80 composition reported in **Table 3** above [30]. It is therefore unclear whether ε-Cu precipitates persisted at the 825 °C (1517 °F) ICHAZ peak temperature, but complete dissolution was expected for all higher peak temperature samples. *SYSWELD* does not explicitly account for M/A constituent or precipitates of any kind, so phase fractions of these specimens were reported to be entirely ferrite, as shown in **Table 4**.

The average size of the M/A constituent appeared to decrease as cooling rate increased. Evidence of M/A constituent banding was present in the 1 °C/s (1.8 °F/s) and, to a lesser degree, in the 5 °C/s (9 °F/s) specimens. M/A constituent formation requires local carbon enrichment. Austenite has a significantly higher solubility for carbon than ferrite does, so partial transformation of the ferritic base material into austenite would have encouraged diffusion of carbon from ferritic regions to austenitic ones.

Further, banding of alloying elements or impurities is a common phenomenon in rolled plate. A calculation performed using Thermo-Calc 2020b and the TCFE9 thermodynamic database [30] predicted that the chemical potential of carbon would be lower in areas where remnant macrosegregation of substitutional elements was present, further driving diffusion towards those areas. This effect was predicted for every intentional alloying addition with the exception of Si and Mo, which had the opposite effect.

Diffusion of carbon towards banded regions of alloying elements explains the presence of M/A constituent in bands upon cooling. The absence of such banding in specimens heated to higher peak temperatures is expected, as these samples spent more time in high temperature regimes. These temperatures are associated with higher mobility of alloying elements, and with sufficient time they are able to thoroughly diffuse and create a homogeneous distribution rather than one with locally enriched regions. Increased cooling rates were also associated with an increasing number of small precipitates. Microhardness increased slightly from 173 to 208 $HV_{200}$ for samples cooled from 1 to 25 °C/s (1.8 to 45 °F/s). This is likely due to two simultaneous phenomena: first, strengthening from the increased number of precipitates; and second, a Hall-Petch effect from the decreased ferrite grain size in recrystallized areas, as is qualitatively apparent in **Figure 62a-d**. Only one transformation was detected in the on-cooling dilation data for each of these samples. Transformation start temperatures remained stable at approximately 761 °C (1402 °F) across this range of cooling rates, with the exception of the sample cooled at 5 °C/s (9 °F/s), with a measured transformation start temperature of 749 °C (1380 °F). Transformation finish temperatures fell from 653 to 624 °C (1207 to 1155 °F), with a slight increase to 663 °C (1225 °F) for the sample cooled at 5 °C/s (9 °F/s). As was seen during previous investigations of DH36 [5] and HSLA-65 [6] steels, there was no discernible transformation temperature for M/A constituent; rather, the temperatures described were associated with transformation from austenite to ferrite.

Samples cooled at 100 and 200 °C/s (180 and 360 °F/s) were composed of fine quasipolygonal ferrite, M/A constituent, and precipitates of approximately 0.1-0.2 μm ($3.9\text{-}7.9 \times 10^{-6}$-in.) in diameter, as shown in **Figure 63**. Identification of precipitation composition was outside the scope of the present investigation, as such attributes are not explicitly accounted for in finite element welding process models. It is assumed that these include niobium-carbonitride [Nb(CN)] precipitates, as these are intentionally induced in HSLA-80 base material for precipitation strengthening but would not have dissolved into solid solution at such a low peak temperature [21]. Transformation start temperatures of 685 and 691 °C (1265 and 1276 °F) were slightly lower than those measured for more slowly cooled specimens, with finish temperatures of 543 and 540 °C (1009 and 1004 °F), respectively.

It is acknowledged that the phase fraction of the two rapidly cooled specimens qualitatively appears to have a high proportion of M/A constituent. This dark-etched constituent bears a resemblance to martensite and, as the name implies, may be partially composed of martensite. Despite this, the high transformation temperatures, the low microhardness values of 209 and 220 $HV_{200}$, and the absence of martensite in rapidly cooled samples heated to the next highest peak temperature of 1000 °C (1832 °F) support the identification of M/A constituent. As discussed previously, for the purposes of *SYSWELD* simulations this is not considered to be a distinct phase and has been reported as 100% ferrite in **Table 4**. However, due to the sheer quantity in these samples, other investigations may benefit from closer examination and characterization of this constituent.

Optical micrographs of HSLA-80 specimens heated to 1000 °C (1832 °F) are shown in **Figure 64** with measured phase fractions in **Table 5**. These samples were intended to reproduce FGHAZ microstructures and thus were fully austenitized prior to cooling. The microstructures observed in samples cooled from 1-25 °C/s (1.8-45 °F/s) were the same as those formed in the corresponding ICHAZ samples:

primary ferrite and M/A constituent. The higher peak temperature produced a slightly larger grain size in the sample cooled at 1 °C/s (1.8 °F/s) due to the increased time available for grain growth above $A_{c3}$. The M/A constituent banding that was observed in slowly cooled ICHAZ samples was absent in samples heated to 1000 °C (1832 °F), likely because increased time at high temperature allowed diffusion of alloying elements and partial homogenization of the austenitic solid solution. Microhardness values mirrored those of the lower peak temperature at cooling rates less than 25 °C/s (45 °F/s), falling between 180 and 205 $HV_{200}$. Microhardness for the 25 °C/s (45 °F/s) cooled sample was 225 ± 15 $HV_{200}$, which is 17 $HV_{200}$ lower than the corresponding ICHAZ sample as a result of the finer grain structure. Transformation start temperatures for these four cooling rates fell from 760 to 673 °C (1400 to 1243 °F) as cooling rate increased.

**Table 4.** Measured Phase Fraction of HSLA-80 CCT Specimens Thermally Cycled to a Peak Temperature of 825 °C (1517 °F)

| Cooling Rate | | Peak Temperature = 825 °C (1517 °F) | | |
|---|---|---|---|---|
| °C/s | °F/s | F + M/A | B | M |
| 1 | 1.8 | 1.0 | 0 | 0 |
| 5 | 9 | 1.0 | 0 | 0 |
| 10 | 18 | 1.0 | 0 | 0 |
| 25 | 45 | 1.0 | 0 | 0 |
| 100 | 180 | 1.0 | 0 | 0 |
| 200 | 360 | 1.0 | 0 | 0 |

**Table 5.** Measured Phase Fraction of HSLA-80 CCT Specimens Thermally Cycled to a Peak Temperature of 1000 °C (1832 °F)

| Cooling Rate | | Peak Temperature = 1000 °C (1832 °F) | | |
|---|---|---|---|---|
| °C/s | °F/s | F + M/A | B | M |
| 1 | 1.8 | 1.0 | 0 | 0 |
| 5 | 9 | 1.0 | 0 | 0 |
| 10 | 18 | 1.0 | 0 | 0 |
| 25 | 45 | 1.0 | 0 | 0 |
| 100 | 180 | 0.98 | 0.02 | 0 |
| 200 | 360 | 0.94 | 0.06 | 0 |

Samples cooled at 100 and 200 °C/s (180 and 360 °F/s) were predominantly composed of fine quasipolygonal ferrite. Undercooling caused a drop in transformation temperatures to 640 and 634 °C (1183 and 1243 °F), respectively, driving a morphological shift from the relatively equiaxed ferrite found in more slowly cooled samples. A substantial increase in microhardness was associated with this change in morphology, rising to 248 ± 21 and 262 ± 6 $HV_{200}$ for the 100 and 200 °C/s (180 and 360 °F/s), respectively. In addition to ferrite, there appeared to be small packets of bainite. These are visible in **Figure 65** as small packets of aligned ferrite laths.

The visual difference between ferrite and bainite can be subtle, particularly when small prior austenite grain sizes do not allow for the growth of long, high aspect ratio laths. Various constitutive equations for predicting the start temperatures for bainite and martensite transformations based on alloy chemistry are available in the literature [31] [32]. Such models are generally oversimplifications and often are only accurate for alloys similar to those used to create them, but they can act as a guide for reasonable temperatures at which to expect formation of intermediate and low temperature phases. As such, the

models developed by Capdevilla *et al.* [33] and Kirkaldy [34] were applied to the averaged HSLA-80 composition given in **Table 3**:

$$M_s = 491.05 - 302.6w_C - 30.6w_{Mn} - 16.6w_{Ni} - 8.9w_{Cr} + 2.4w_{Mo} - 11.3w_{Cu} + 8.58w_{Co} + 7.4w_W - 14.5w_{Si} \quad \textbf{(5)}$$

$$B_s = 656 - 57.7w_C - 75w_{Si} - 35w_{Mn} - 15.3w_{Ni} - 32w_{Cr} - 41.2w_{Mo} \quad \textbf{(6)}$$

where $M_s \equiv$ martensite start temperature (°C)
$B_s \equiv$ bainite start temperature (°C)
$w_i \equiv$ concentration of element $i$ (wt.%)

From **Equations 5** and **6**, the $M_s$ and $B_s$ temperatures for HSLA-80 are predicted to be 425 °C (798 °F) and 571 °C (1060 °F), respectively. The temperature ranges observed in rapidly cooled samples heated to 1000 °C (1832 °F) are 640-507 °C (1184-945 °F) and 634-503 °C (1173-937 °F), encompassing the predicted bainite transformation temperature. This and the relatively high microhardness values of 248 ± 20 and 262 ± 6 $HV_{200}$ both support identification of the secondary phase as bainite. Primary ferrite and bainite are both shown in the micrographs in **Figure 65e-f**.

Representative microstructures of samples heated to 1150 °C (2102 °F) are shown in **Figure 66** with measured phase fractions reported in **Table 6**. Samples cooled at rates from 1-10 °C/s (1.8-18 °F/s) resulted in mixtures of polygonal and quasipolygonal ferrite interspersed with small islands of M/A constituent. These are the same phases associated with slow cooling for the two lower peak temperatures, but the 1150 °C (2102 °F) temperature was sufficient for grain growth. Increasing cooling rate to 25 °C/s (45 °F/s) introduced acicular ferrite and bainite to the quasipolygonal ferrite and M/A constituent observed in more slowly cooled samples. Transformation start and finish temperatures both fell as cooling rate increased, dropping from 665 to 612 °C (1129 to 1134 °F) and from 503 to 472 °C (937 to 882 °F), respectively. Similarly, microhardness increased from 222 ± 7 to 261 ± 12 $HV_{200}$ with the shift from the softer phases formed during slow cooling.

**Table 6.** Measured Phase Fraction of HSLA-80 CCT Specimens Thermally Cycled to a Peak Temperature of 1150 °C (2102 °F)

| **Cooling Rate** | | **Peak Temperature = 1150 °C (2102 °F)** | | |
|---|---|---|---|---|
| **°C/s** | **°F/s** | **F + M/A** | **B** | **M** |
| 1 | 1.8 | 1.0 | 0 | 0 |
| 5 | 9 | 1.0 | 0 | 0 |
| 10 | 18 | 1.0 | 0 | 0 |
| 25 | 45 | 0.85 | 0.15 | 0 |
| 100 | 180 | 0 | 0.76 | 0.24 |
| 200 | 360 | 0 | 0.62 | 0.38 |

Cooling rates of 100 and 200 °C/s (180 and 360 °F/s) were too rapid for formation of ferrite. Instead, microstructures consisted of a mixture of bainite and martensite, as shown in **Figure 66e-f**. The bainite start temperature was measured to be 551 and 565 °C (1024 and 1049 °F) for the 100 and 200 °C/s (180 and 360 °F/s) samples, respectively. While the martensite start temperature was difficult to discern from the dilation data, the finish temperatures were 412 and 409 °C (774 and 768 °F). As expected, microhardness was higher than all previously discussed specimens at 282 ± 18 and 277 ± 9 $HV_{200}$.

The last set of samples were heated to 1350 °C (2462 °F) in order to simulate the CGHAZ. Representative optical micrographs are presented in **Figure 67** and corresponding phase fractions are reported in **Table 7**. HSLA-80 derives strength from both ε-Cu and Nb(CN) precipitates, which pin austenite grain boundaries and maintain a fine grain structure [21]. At temperatures above equilibrium dissolution temperature, precipitates dissolve into solid solution and allow for unhindered austenite grain growth. This is demonstrated in the specimen cooled at 1 °C/s (1.8 °F/s), which presented significantly larger ferrite grains than those formed at lower peak temperatures. As noted above, Bhagat *et al.* indicated that under isothermal aging conditions, dissolution of copper precipitates occurred at 650 °C (1202 °F) [29], and calculations in this study predicted an ε-Cu dissolution temperature near 730 °C. From this, it can be assumed that dissolution of ε-Cu precipitates was complete for each peak temperature investigated, and thus does not explain the increased grain size only observed at the 1350 °C (2462 °F) peak temperature. Shome and Mohanty [21] calculated Nb(CN) precipitate dissolution by applying the invariant size model to a precipitate size of 0.02 μm (7.9 x $10^{-7}$-in.). For heat inputs of 10 and 40 kJ/cm (25.4 and 101.6 kJ/in), dissolution temperature was predicted to be 1245 and 1200 °C (2273 and 2192 °F), respectively. No attempt was made to identify precipitate dissolution temperatures in the present study, but the significant increase in grain size between peak temperatures of 1150 and 1350 °C (2102 and 2462 °F) is consistent with dissolution temperatures predicted by Shome and Mohanty [21]. High temperature phase dissolution was also predicted using Thermo-Calc 2020b and the TCFE9 database [30]. Under the equilibrium conditions assumed in the calculations, dissolution of Nb(CN) was predicted to occur at approximately 1115 °C (2039 °F). Though precipitate size was not quantified during this study, it is likely that Gleeble test conditions more closely mirrored those examined in the study by Shome and Mohanty, with precipitate dissolution temperatures approaching temperatures at or above 1200 °C (2192 °F) [21]. This is further suggested by the lack of significant grain growth observed in samples heated to 1150 °C (2102 °F). The minute volumetric change associated with precipitate evolution and dissolution meant that neither could be detected in dilatometry curves to confirm this conclusion.

**Table 7.** Measured Phase Fraction of HSLA-80 CCT Specimens Thermally Cycled to a Peak Temperature of 1350 °C (2462 °F)

| **Cooling Rate** | | **Peak Temperature = 1350 °C (2462 °F)** | | |
|---|---|---|---|---|
| **°C/s** | **°F/s** | **F + M/A** | **B** | **M** |
| 1 | 1.8 | 1.0 | 0 | 0 |
| 5 | 9 | 1.0 | 0 | 0 |
| 10 | 18 | 0.80 | 0.20 | 0 |
| 25 | 45 | 0.04 | 0.96 | 0 |
| 100 | 180 | 0 | 0.43 | 0.57 |
| 200 | 360 | 0 | 0.62 | 0.38 |

As shown in **Figure 67a**, the sample cooled at 1 °C/s consisted of primary ferrite decorating large prior austenite grain boundaries along with quasipolygonal ferrite that had formed intragranularly. Small islands of M/A constituent were present as well. The large prior austenite grain size corresponds with a smaller total length of grain boundary. Without these energetically favorable ferrite nucleation points, ferrite formation was suppressed below transformation temperatures observed in previous specimens—transformation start and finish temperatures were 653 and 524 °C (1207 and 975 °F), respectively. The increased proportion of quasipolygonal ferrite is associated with a higher hardness than seen in slow-cooled samples with lower peak temperatures, measuring 230 ± 6 $HV_{200}$. Grain boundary ferrite was eliminated from the sample cooled at 5 °C/s (9 °F/s), leaving a mixture of quasipolygonal ferrite and M/A constituent. Bainite was added to that mixture in the sample cooled at 10 °C/s (18 °F/s). The large grain size discussed previously precluded formation of polygonal ferrite entirely, allowing formation of bainite

at lower cooling rates than observed for lower peak temperatures. Transformation start temperatures fell from 632 to 603 °C (1170 to 1117 °F) as cooling rate increased, though transformation finish temperatures remained approximately steady at 494 and 493 °C (921 and 919 °F). Microhardness increased 233 ± 9 to 248 ± 8 $HV_{200}$ with increased cooling rate, indicative of the introduction of bainite.

Increasing cooling rate to 25 °C/s (45 °F/s) produced a microstructure that was primarily bainite with a small amount of acicular ferrite, as shown in **Figure 67d**. The initial transformation from austenite fell further from that of more slowly cooled samples, measured to be 567 °C (1053 °F). This likely corresponded with the bainite transformation, with the proportion of acicular ferrite too small to discern in the dilation curve, though acicular ferrite is also associated with low transformation temperatures. Martensite was not observed in micrographs, though the low transformation finish temperature of 424 °C (795 °F) supports its presence in very small amounts. The large standard deviation of microhardness data is also indicative of the wide range of phases: microhardness was measured to be 266 ± 22 $HV_{200}$. Further increases in cooling rate to 100 and 200 °C/s (180 and 360 °F/s) resulted in dual phase microstructures of bainite and martensite, with bainite transformation start temperatures of 535 and 536 °C (995 and 997 °F), respectively. Martensite start temperature was difficult to discern, but appeared to be 490 °C (914 °F) for both specimens. This transformation completed at 408 and 404 °C (766 and 759 °F) for the 100 and 200 °C/s (180 and 360 °F/s) samples, respectively. Microhardness values were also quite similar, measuring 302 ± 17 and 295 ± 12 $HV_{200}$. Optical micrographs of these two specimens are shown in **Figure 67e-f**.

It is noted that in several dilation curves, there is a high temperature anomaly which is not associated with the microstructural evolution discussed previously. Under ideal experimental conditions the austenitic portion of the dilation curve would have an approximately linear slope. The dilation curves for samples heated to 1350 °C (2462 °F) each show two distinct portions, with the high temperature portion appearing to decrease in dilation more rapidly with respect to temperature. This is not the result of a phase transformation; rather, it reflects deformation of the specimen by the small force exerted by the Gleeble jaws. The low strength of the material at such a high temperature was evidenced by the dip in the cooling portion of the CCT curves and was further supported by micrographs showing enlarged austenite grains, which were present due to dissolution of strengthening precipitates and indicated a low strength microstructure in the high temperature regime. The dilation curve returns to a linear rate of contraction as specimens recover strength at temperatures lower than approximately 1100 °C (2012 °F). The same phenomenon was observed in samples heated to 1150 °C (2102 °F) but the reduced time at high temperatures rendered the effect less pronounced.

The phase transformation information developed here is critically important for ensuring that weld simulation software can draw on thermo-physical and thermo-mechanical property information from the appropriate phases at the appropriate times during calculations. The results in **Figures 8-11** highlight the importance of developing multiple HAZ-related CCT diagrams.

## Weldment Microstructures

Metallographic specimens were removed from both weldments and analyzed in a manner similar to the Gleeble specimens. Discussion of microstructures present correspond to the HAZ of the second pass for each weldment, as the reheating experienced by the first pass confounded the analysis and did not directly correlate with thermal cycles undergone by Gleeble CCT specimens.

The tee joint fusion zone was a mixture of coarse primary ferrite, acicular ferrite, and unidentified carbides. **Figure 16** presents representative micrographs from HAZ of the tee joint. **Figure 16a** shows that the CGHAZ was composed of upper bainite with quasipolygonal primary ferrite. **Figure 16b** shows that the FGHAZ directly adjacent to the CGHAZ was composed of the same microstructures, with an

increased proportion of ferrite. **Figure 16c** shows that as distance increased from the fusion line, bainite was no longer present in the FGHAZ. Instead, phases present included quasipolygonal ferrite and islands of M/A constituent. These same phases appeared in the ICHAZ, as shown in **Figure 16d**, with a finer grain size. The dilatometry specimen microstructures that most closely correspond with those observed in the fillet weld CGHAZ, FGHAZ, and ICHAZ are those associated with 10 °C/s (18 °F/s) cooling. There is good agreement with the microhardness values of the Gleeble samples cooled at 10 °C/s (18 °F/s), which fell within the range of 199-248 $HV_{200}$, and those of the weldment HAZ, falling within the range of 165-255 $HV_{200}$.

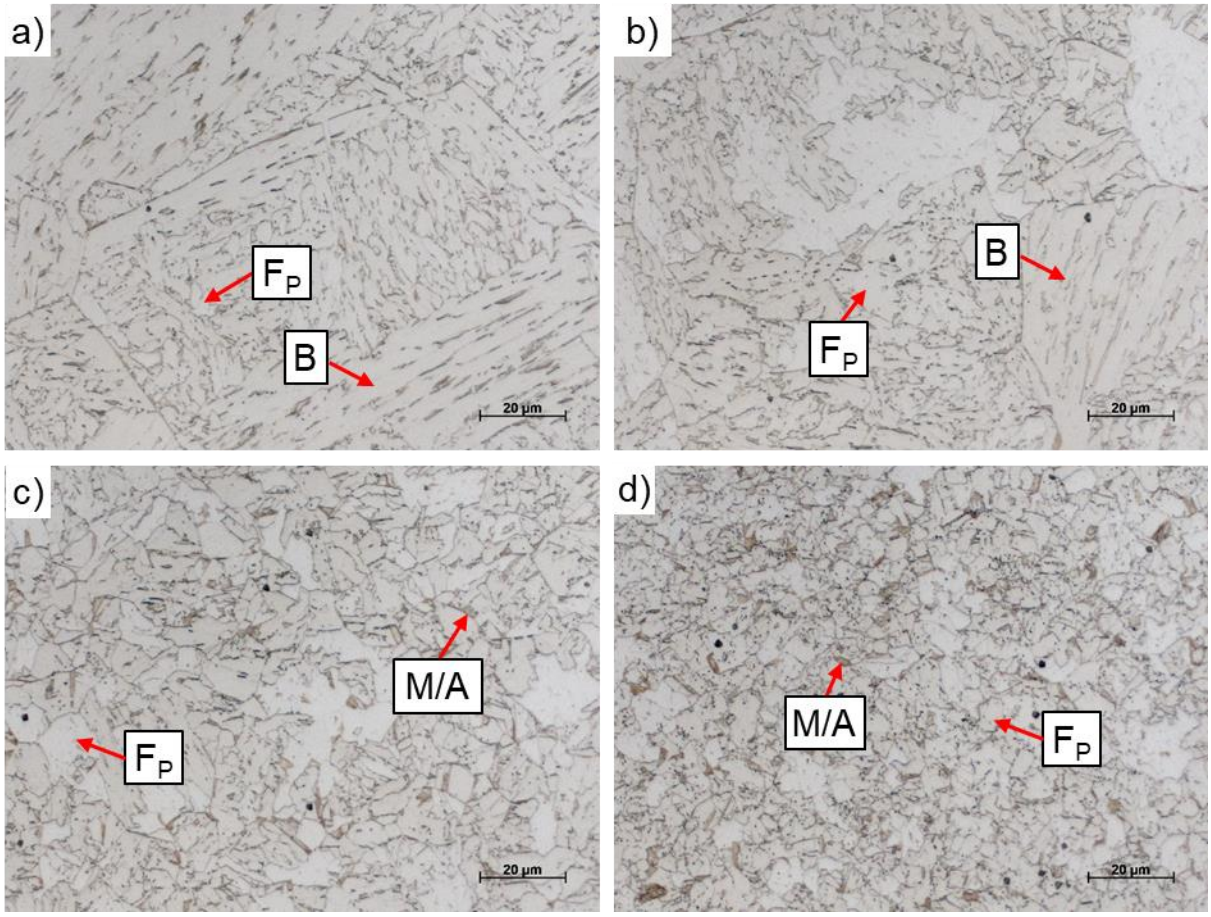


**Figure 16.** Representative light optical micrographs of the second pass of the HSLA-80 tee joint showing the **a)** CGHAZ, **b)** FGHAZ close to the CGHAZ, **c)** FGHAZ close to the ICHAZ, and **d)** ICHAZ.

The light optical micrographs in **Figure 17** demonstrate placement of microhardness indents within the microstructural gradient of the tee joint's HAZs. **Figure 18** shows the averaged measurements from the three linear patterns associated with each weld bead. Microhardness data is presented as distance from the fusion line, though the width of the heat affected zone varied depending on location within the weldment (*i.e.*, near the surface or the center of the plate) because of the small plate thickness. As such, care should be taken when comparing values taken at the same distance from the fusion line, as they do not necessarily correspond with the same region of the HAZ. Inconsistencies also exist between microhardness values at the same linear distance from the fusion line due to challenges associated with

collecting hardness traverses perpendicular to the non-semicircular HAZ boundaries in thin plates. Nevertheless, trends for the HAZ microhardness were consistent for microhardness patterns measured in comparable locations of each bead (*e.g.*, patterns 1 and 2). There was a significant increase of approximately 26 $HV_{200}$ for measurements in the fusion zone and CGHAZ. Microhardness then fell steadily with distance from the fusion line. The softest region was the ICHAZ, with values reaching as low as 203 $HV_{200}$ before beginning a steady increase towards the average base metal hardness of 246 $HV_{200}$. Pattern 3 did not follow this trend. Due to its placement between the two weld beads, this material experienced reheating from deposition of the second weld bead and it was difficult to discern a clear pattern over the length of this traverse.


**Figure 17.** Composite image of light optical micrographs of the HSLA-80 fillet weld showing placement of microhardness indents. Indents appear as sets of parallel lines of black dots on the left, center, and right sides of the image.

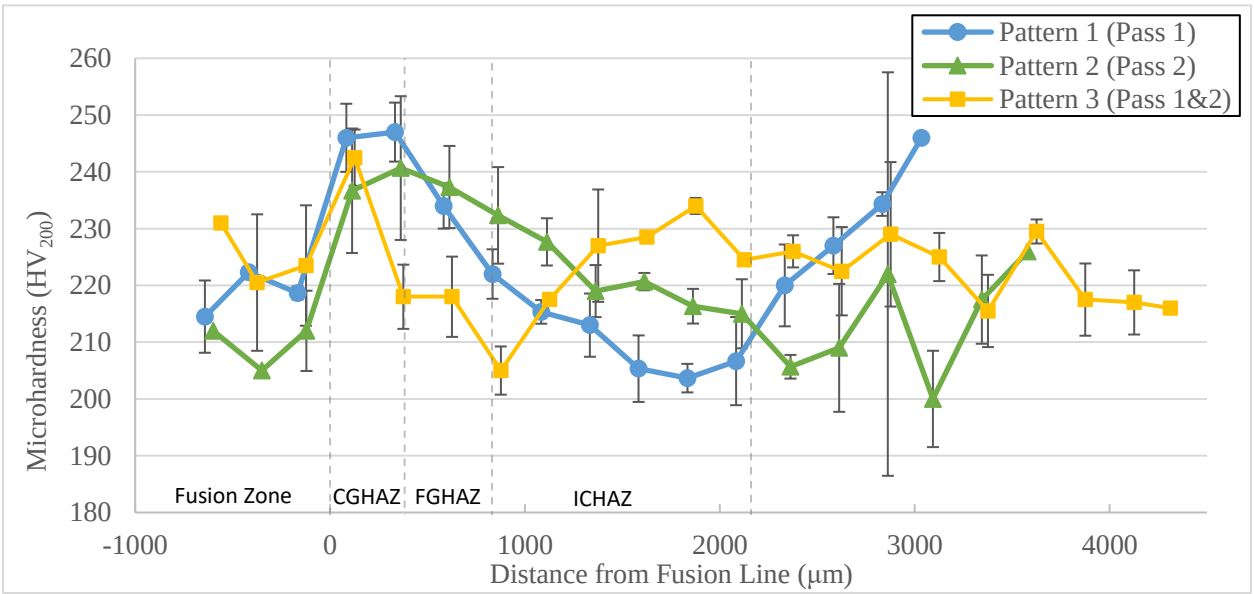


**Figure 18.** Average Vickers microhardness across the indents made for each fillet weld pass, as shown in **Figure 17**. Error bars are one standard deviation. Values with a negative distance from the fusion line are in the fusion zone. Approximated HAZ regions are delineated by vertical dashed lines.

The same analysis was carried out for the butt joint weldment. The fusion zone of the butt joint mirrored that of the tee joint, with a mixture of acicular ferrite, primary ferrite, and unidentified carbides. Heat from the second pass was sufficient to anneal the edge of the fusion zone of the first pass, resulting in polygonal ferrite near the fusion line. Optical micrographs of the HAZ are shown in **Figure 19**. Similar microstructures were found in the butt joint and tee joint HAZs. The CGHAZ, shown in **Figure 19a**, consisted of bainite and quasipolygonal ferrite. Neither region of the FGHAZ, shown in **Figure 19b-c**, showed evidence of bainite. The region adjacent to the CGHAZ consisted of quasipolygonal ferrite and M/A constituent, with more refined ferrite observed in the region adjacent to the ICHAZ. The ICHAZ is shown in **Figure 19d** and has a similar microstructural composition as the FGHAZ, with only polygonal ferrite and M/A constituent present. The ferrite grains in the ICHAZ had a much more equiaxed morphology than those in the FGHAZ.

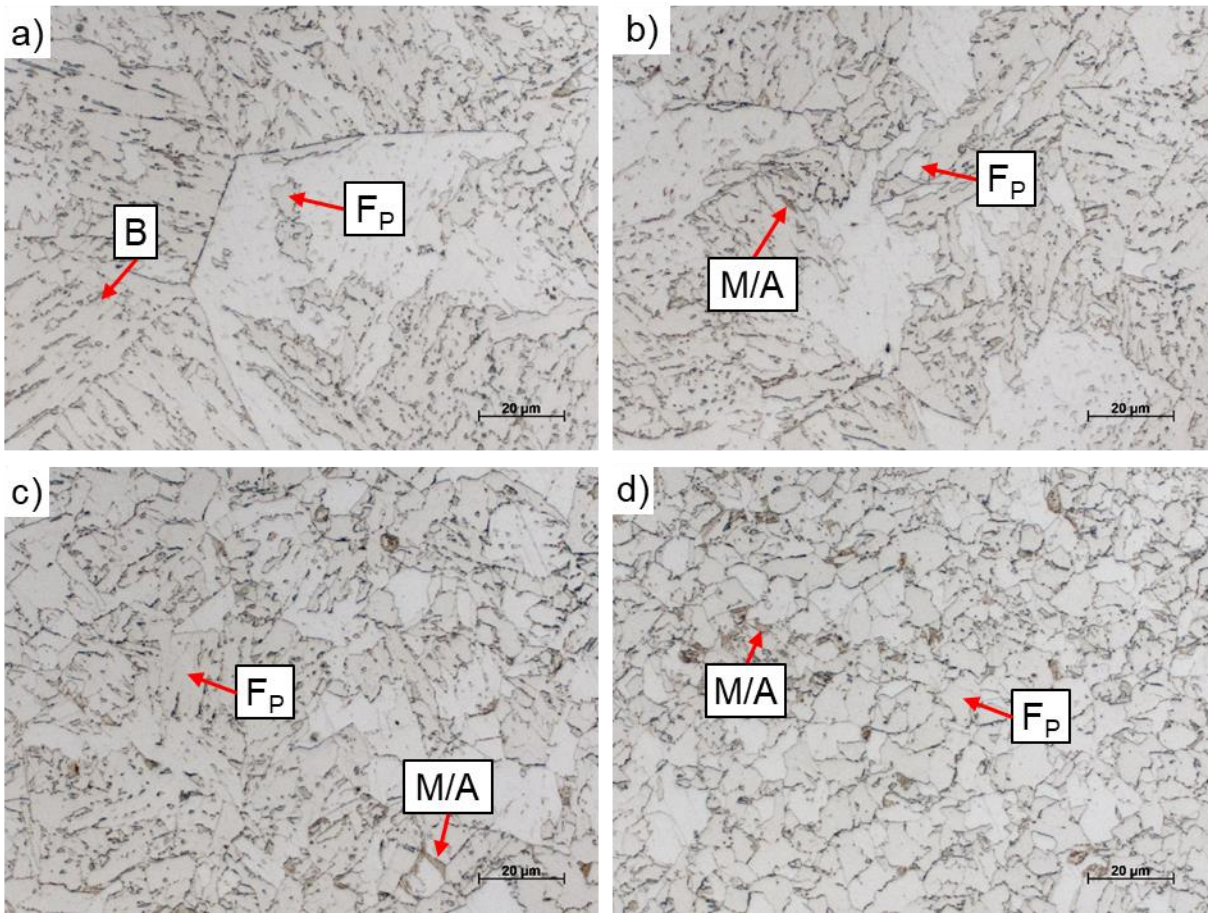


**Figure 19.** Representative light optical micrographs of the second pass of the HSLA-80 butt joint showing the **a)** CGHAZ, **b)** FGHAZ close to the CGHAZ, **c)** FGHAZ close to the ICHAZ, and **d)** ICHAZ.

Microhardness testing similar to that reported for the tee joint was performed on the butt joint, with a composite light optical micrograph shown in **Figure 20** that demonstrates placement of four linear microhardness patterns. Microhardness was assessed near each weld toe in the butt joint, with values presented in **Figure 21** and **Figure 22** for the first and second pass, respectively. Microhardness values associated with the first pass were inconsistent between each weld toe due to differences in the extent of reheating done by the second pass. Microhardness pattern 1 followed a similar trend as measurements in

the fillet joint, with a relatively high microhardness in the CGHAZ that fell as distance increased into the FGHAZ and ICHAZ before rising again to approach base metal values. Pattern 2 had similar microhardness values in the CGHAZ which also decreased through the ICHAZ, but there was no measured hardness increase in the pattern as it approached the base metal. As shown in the composite micrograph, this is due to the overlap of pattern 2 and the HAZ of the second pass; there is no portion of pattern 2 that reaches true base metal. The microhardness associated with the second pass follows the same pattern as those in the tee joint: relatively high microhardness in both the fusion zone and CGHAZ that dropped through the ICHAZ before increasing again towards base metal values. In general, microhardness values associated with the first pass of the butt joint were softer than those of the second, likely as a result of precipitate dissolution during reheating.

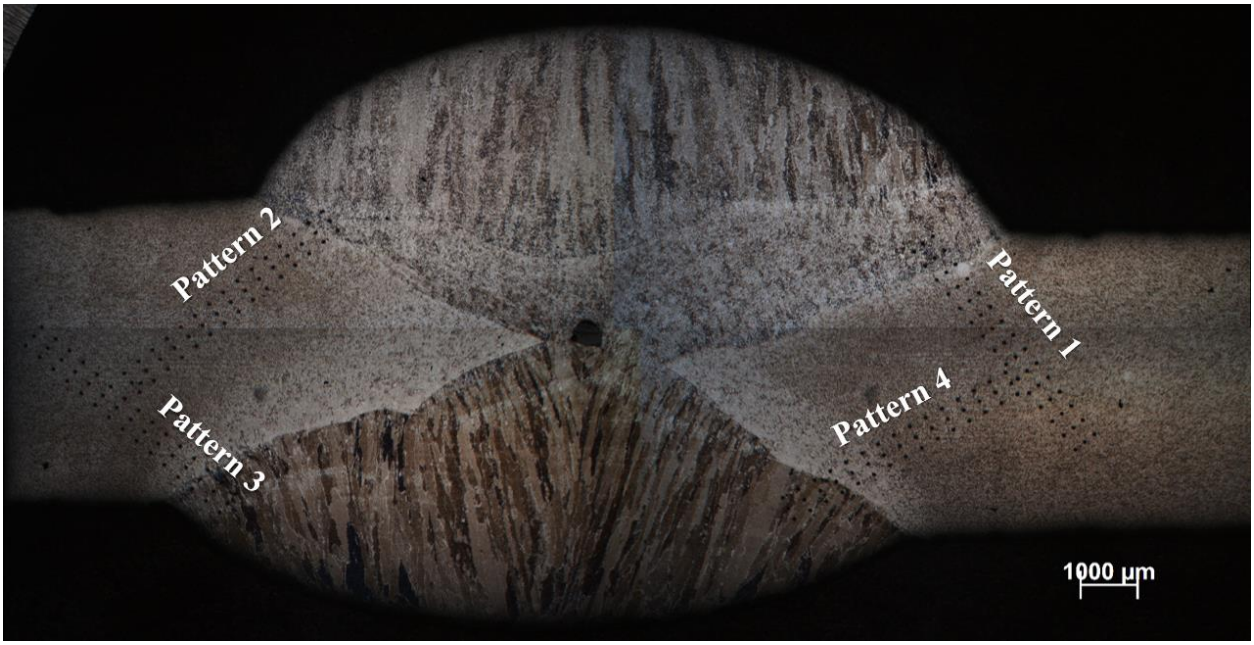


**Figure 20.** Composite image of light optical micrographs of the HSLA-80 butt joint weldment showing placement of microhardness indents. Indents appear as three sets of parallel lines of black dots on the left and right sides of the image.

Microhardness values measured in the butt joint were overall slightly lower than those of the tee joint. The butt and tee joints had microhardness ranges of 166-249 and 194-253 $HV_{200}$, respectively. This is likely due to the differences in heat distribution between the two joint designs. The weld beads in the tee joint are spaced slightly further apart than those in the butt joint. Additionally, the angle of the welding torch used to deposit weld beads resulted in comparatively less overlap in thermal energy distribution. These two geometric factors somewhat isolated the two welded regions from one another in the tee joint configuration. Conversely, the two weld beads in the butt joint were directly opposite one another, with heat input from the second pass reheating and effectively tempering the first weld bead. The differences in HAZ overlap are apparent in the low magnification images shown in **Figure 17** and **Figure 20**.

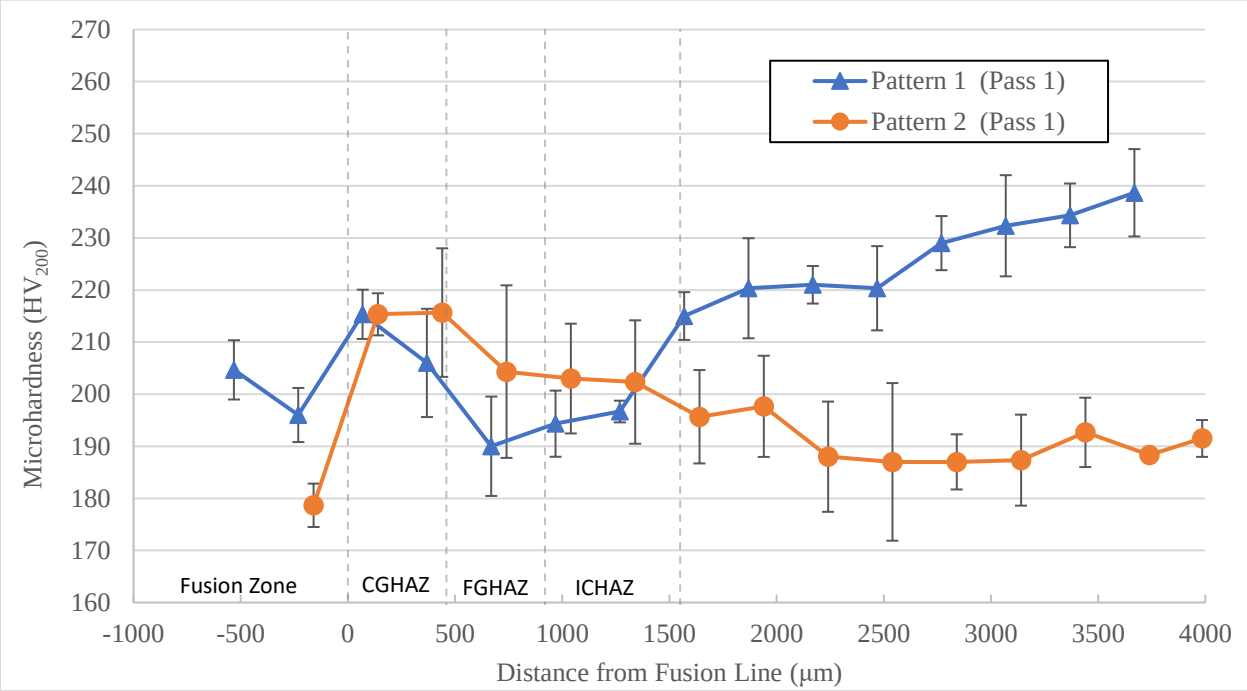


**Figure 21.** Vickers microhardness traverses corresponding to the indents shown in **Figure 20** for welding pass 1. Error bars of one standard deviation are shown where two measurements were taken at the same distance from the fusion line.

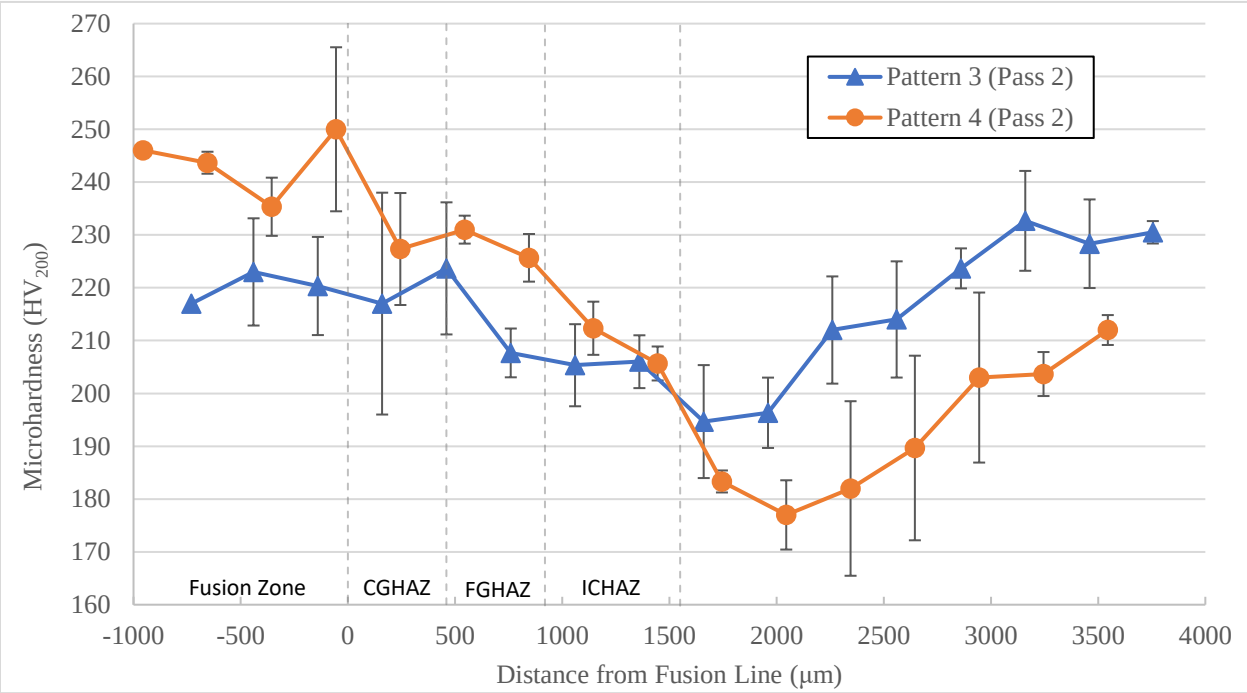


**Figure 22.** Vickers microhardness traverses corresponding to the indents shown in **Figure 20** for welding pass 2. Error bars of one standard deviation are shown where two measurements were taken at the same distance from the fusion line.

Despite the difference in thermal cycles experienced by each weldment, the observed phases are nominally the same. Increased reheating may have caused a higher degree of precipitate dissolution in the butt joint HAZ, which would have contributed to its lower microhardness without significantly changing phase balance. The HAZ for each joint design can be approximated by Gleeble samples cooled at 10 °C/s (18 °F/s).

### Thermo-Physical Property Analysis

The CTE values measured from the dilation curves (n=5) were $1.5 \times 10^{-5} \pm 1.9 \times 10^{-7}$ °C$^{-1}$ ($8.6 \times 10^{-6} \pm 1.0 \times 10^{-7}$ °F$^{-1}$) for the untransformed base metal below 650 °C (1202 °F) and $2.2 \times 10^{-5} \pm 9.1 \times 10^{-7}$ °C$^{-1}$ ($1.2 \times 10^{-5} \pm 5.0 \times 10^{-7}$ °F$^{-1}$) for austenite above 900 °C (1652 °F). A representative graph showing the CTE measurement is given in **Figure 23**.

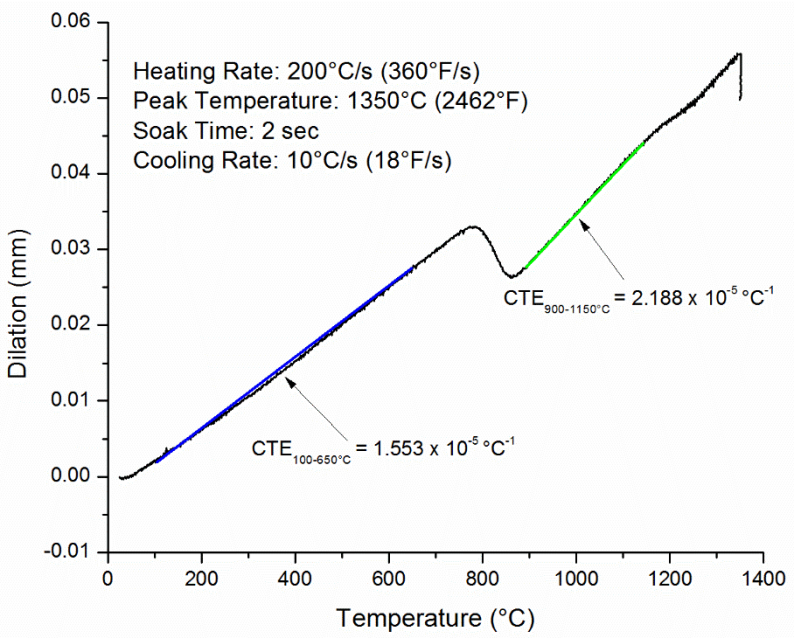


**Figure 23.** Representative on-heating dilatometry curve for HSLA-80, showing typical CTE analysis and results.

Temperature-dependent density values are shown in **Figure 24**. A comparison dataset from a Navy ManTech study [14] conducted at the Naval Metalworking Center from the mid-2000s is also included. Since the slopes of the lines (*i.e.*, the CTE) are nearly identical, differences between the data can be primarily attributed to a difference in the measured room temperature densities between the two studies.

The measured specific heat and thermal diffusivity data for HSLA-80 can be found in **Figures 25-26**. The peaks or cusps in the data correspond to the effects of thermal energy absorption during phase transformations, particularly during the austenitic transformation between approximately 700 to 900 °C (1292 to 1652 °F). As shown, the data from this study compare very well with the data generated in the Navy ManTech study [14]. The data from **Figures 24-26** were used in conjunction with **Equation 4** to calculate the temperature-dependent thermal conductivity as shown in **Figure 27**. Once again, the data coincides well with the previous reporting from CTC. The raw data points for all of the thermo-physical property graphs can be found in **Appendix E**.

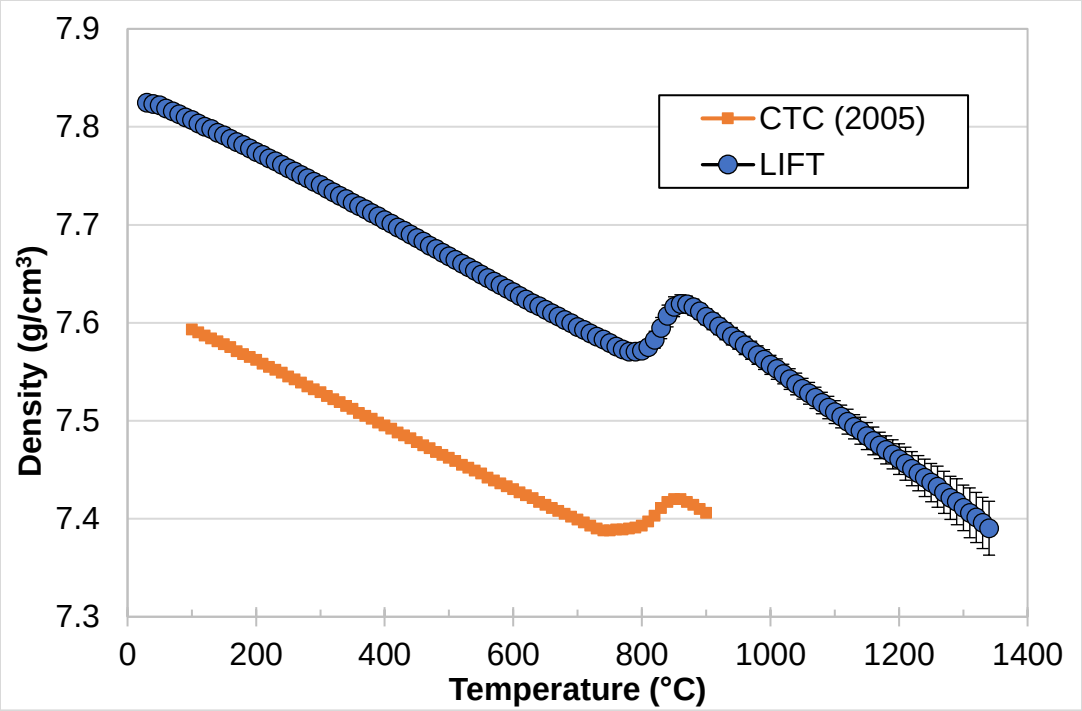


**Figure 24.** Density of HSLA-80 steel as a function of temperature. LIFT data measured using analysis of Gleeble-based dilation curves in accordance with **Equations 2** and **3**. CTC data is adapted from reference [14]. Error bars on LIFT data are one standard deviation from the mean of five tests.

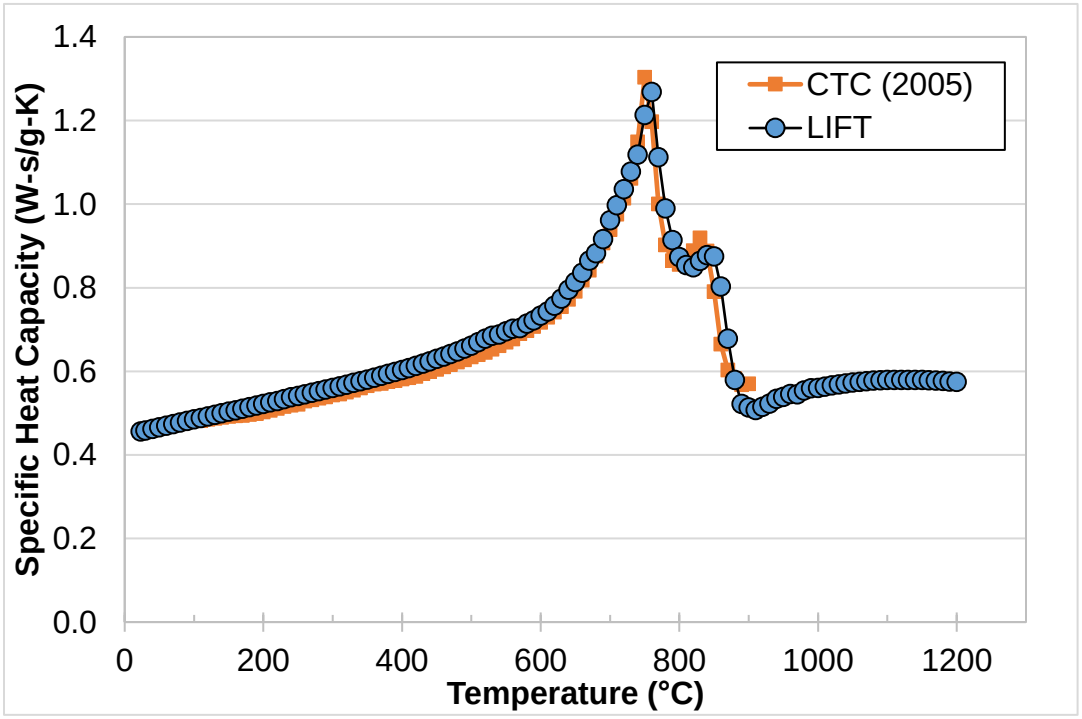


**Figure 25.** Measured specific heat for HSLA-80 steel at various temperatures. CTC data adapted from reference [14].

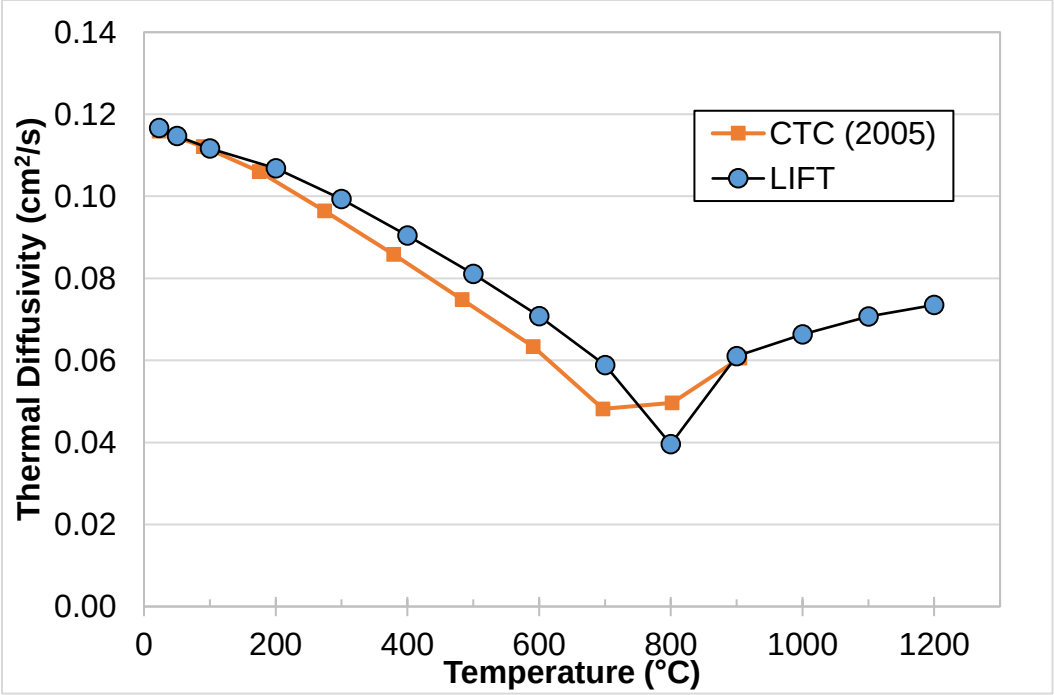


**Figure 26.** Measured thermal diffusivity for HSLA-80 steel at various temperatures. CTC data adapted from reference [14].

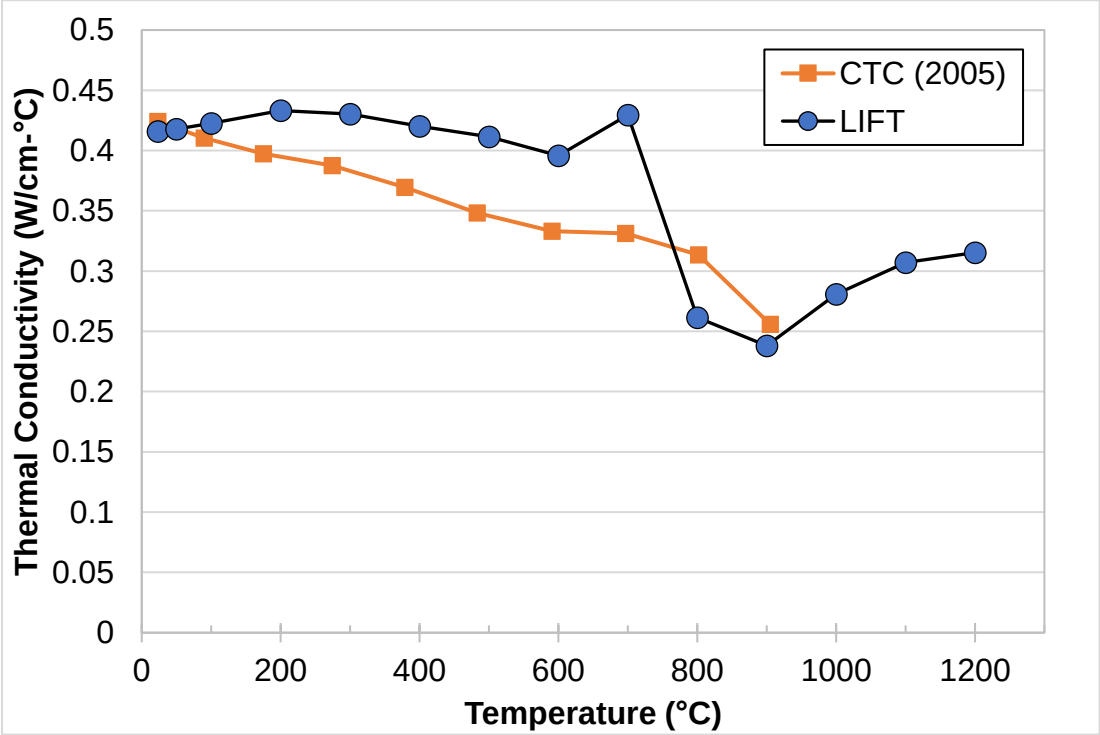


**Figure 27.** Calculated thermal conductivity for HSLA-80 steel at various temperatures. CTC data adapted from reference [14].

### Thermo-Mechanical Property Analysis

**Figure 28** shows the values for elastic modulus as a function of temperature that were assumed in this work. The elevated temperature mechanical testing described above was performed in accordance with ASTM E21 [12] rather than the stricter ASTM E111 [35], which is prescribed when elastic modulus measurements are to be made. As such, it was determined that the experimentally measured elevated temperature elastic moduli were likely inaccurate. In order to provide elevated temperature modulus values for a HSLA-80 property database, the data in **Figure 28** were adapted from the European standard for fire design of steel structures [36] [37]. Of the potential sources for this information, the European standard contained the most complete data covering temperatures relevant to this study. A room temperature elastic modulus of 210 GPa (30.5 Msi) was assumed [36], as it had been previously for DH36 [5] and HSLA-65 [6] steel. It was also assumed that rigorously measured elastic moduli for HSLA-80 steel would be very similar to data presented in **Figure 28** because elastic properties tend to be consistent within a given material class (*e.g.*, low alloy steel). **Figure 29** shows the experimentally measured temperature-dependent 0.2% offset yield strength for HSLA-80 base material, and **Figure 30** shows the measured temperature-dependent ultimate tensile strength (UTS). As expected, increased temperatures result in significant strength loss. At temperatures above 800 °C (1472 °F), the base metal microstructure is completely transformed to the weaker austenite phase, resulting in only minor differences in strength with increasing temperature.

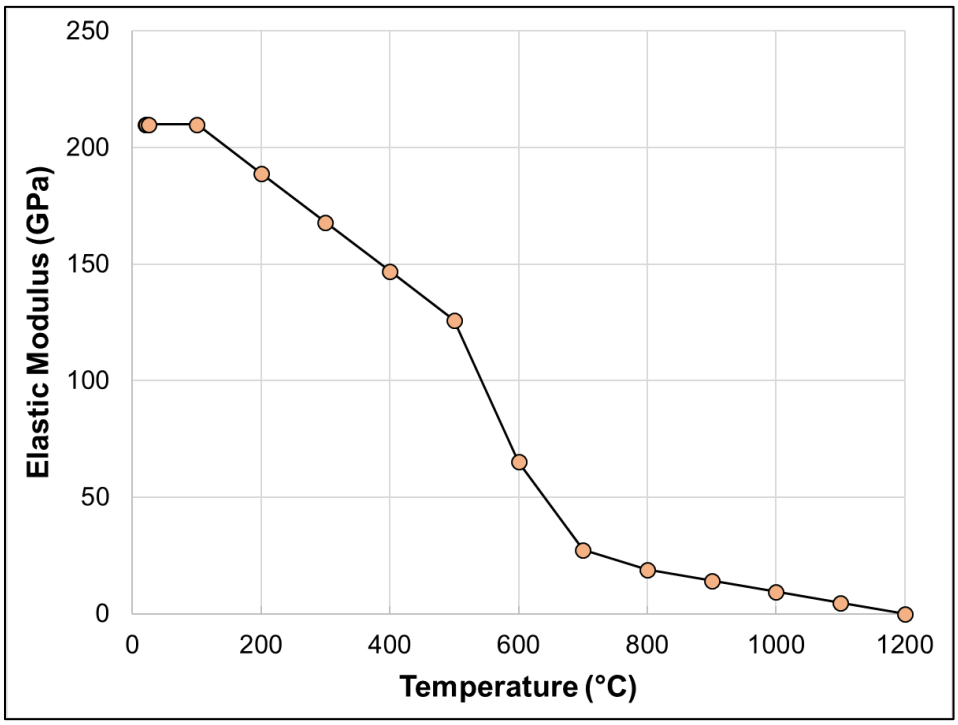


**Figure 28.** Assumed elevated temperature elastic modulus for HSLA-80 steel as adapted from references [36] [37].

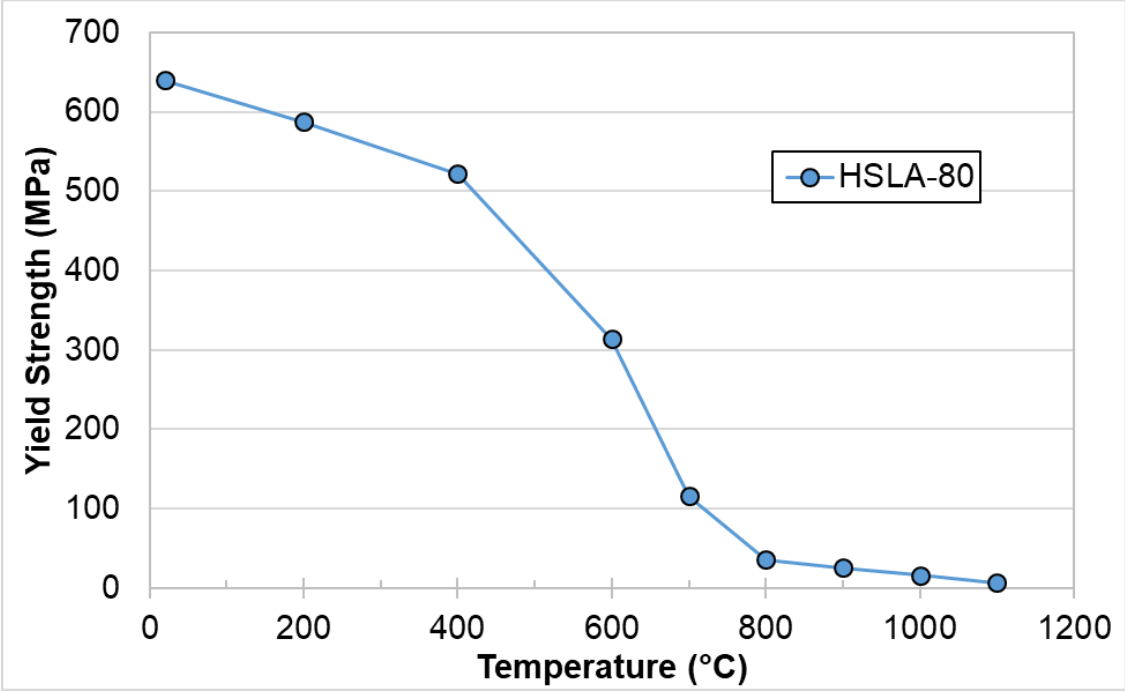


**Figure 29.** Measured elevated temperature 0.2% offset yield strength for HSLA-80 steel.

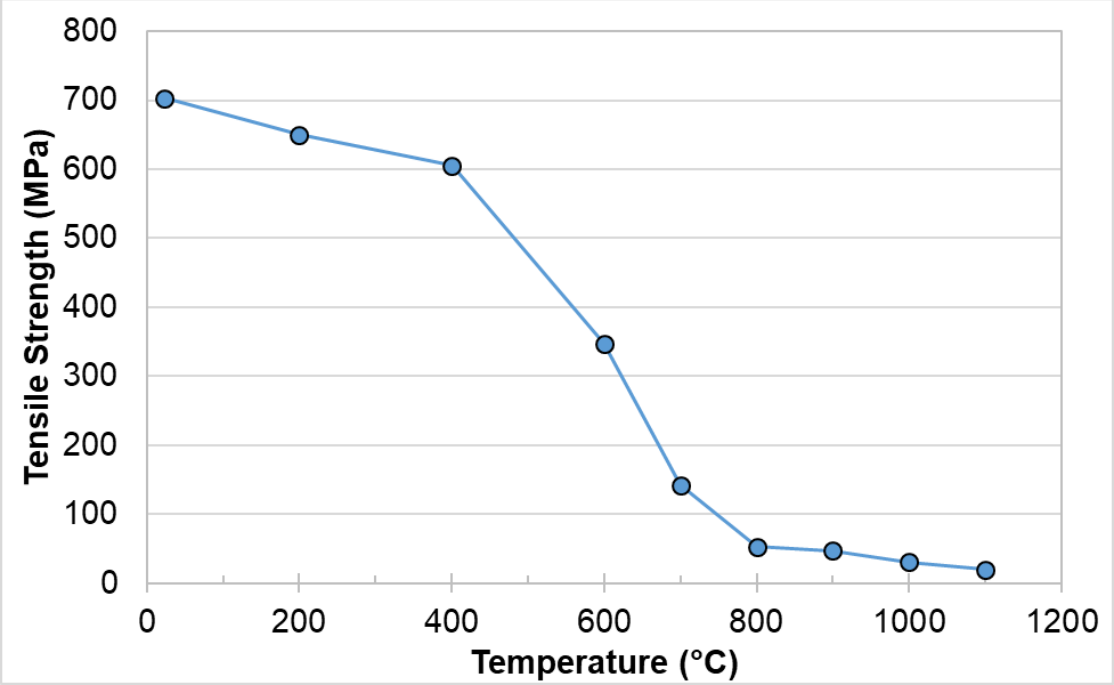


**Figure 30.** Measured elevated temperature ultimate tensile strength for HSLA-80 steel.

**Figure 31** shows the measured 0.2% offset yield strengths from specimens cycled to a peak temperature of 1350 °C (2462 °F) along with that of the base material yield strength for comparison. The stress-strain curves associated with the data are given in **Figures 68-71** of **Appendix F**. At room

temperature, only the yield strength of the 100 °C/s (180 °F/s) specimen exceeded that of the base material. This is the result of the formation of a martensitic microstructure as opposed to the ferritic microstructure of the base material. For testing temperatures below 600 °C (1112 °F), an increase of cooling rate was associated with higher yield strength. At room temperature the yield strength of the specimen cooled at 100 °C/s (180 °F/s) was 28% higher than the sample cooled at 1 °C/s (1.8 °F/s). While the base material experienced a distinct decrease in strength as testing temperature increased, the yield strength of thermally cycled specimens changed very little between the 22 °C and 200 °C (72 and 392 °F). For all temperatures higher than 200 °C (392 °F), strength decreased as testing temperature increased until values converged at the 600 °C (1112 °F) testing temperature.

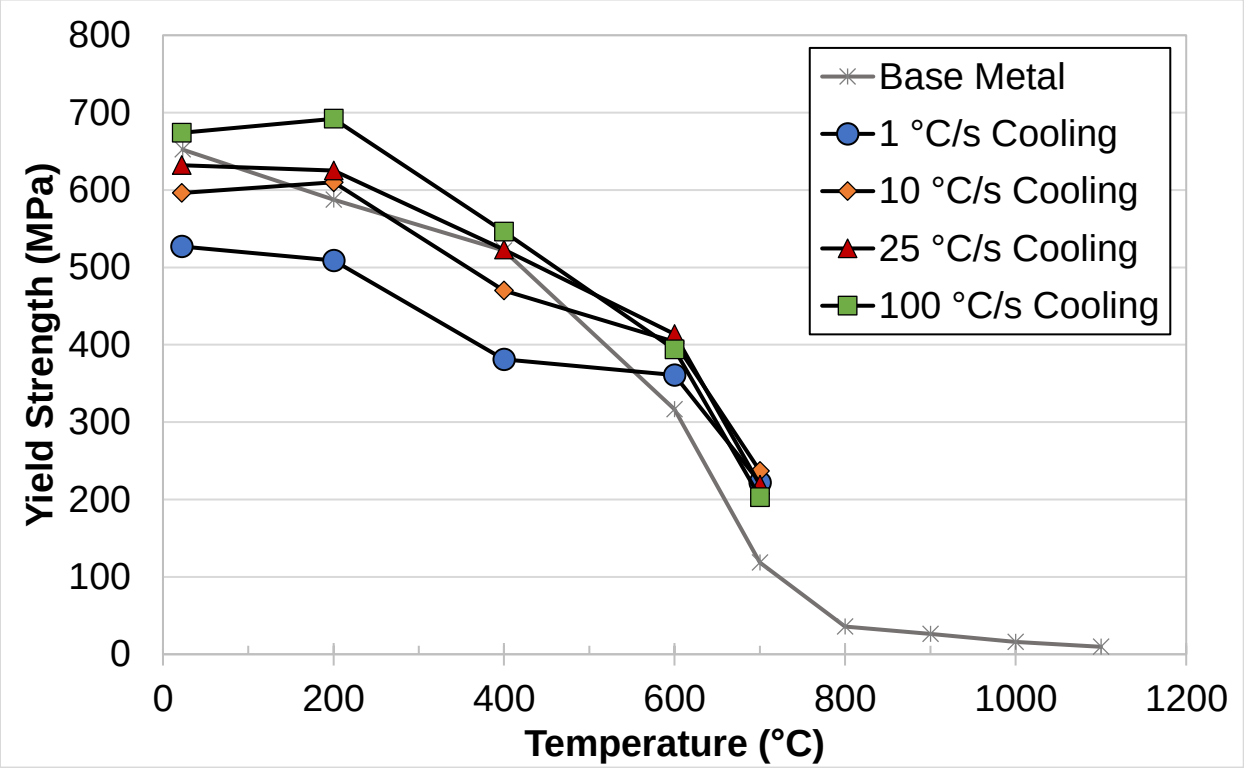


**Figure 31.** Yield strength of simulated HSLA-80 CGHAZs after heating to 1350 °C (2462 °F) and cooling at different rates as compared with base material yield strength.

Elevated temperature flow stress measurements for the HSLA-80 base material are shown in **Figure 32** for all temperatures, and **Figure 33** highlights the flow behavior for tests at temperatures of 800 °C (1472 °F) and above. The raw data for these graphs can be found in **Appendix F**. The data are true stresses and strains calculated by applying the traditional conversion equations to engineering stress-strain data provided by the test lab. Extensometers were used through yield, but for the protection of laboratory equipment, they were removed from each specimen between 2.0 and 5.7% strain at the discretion of the testing personnel. For all cases this removal occurred well before UTS was reached. As a result, the flow stress behavior is not fully characterized for those samples. It is possible, however, to extrapolate the work hardening behavior to the onset of necking using the UTS values, which are also provided in **Appendix F**. As expected, increasing the test temperature tends to flatten the flow stress curves, since work hardening is made more difficult by dynamic recovery and/or recrystallization effects.

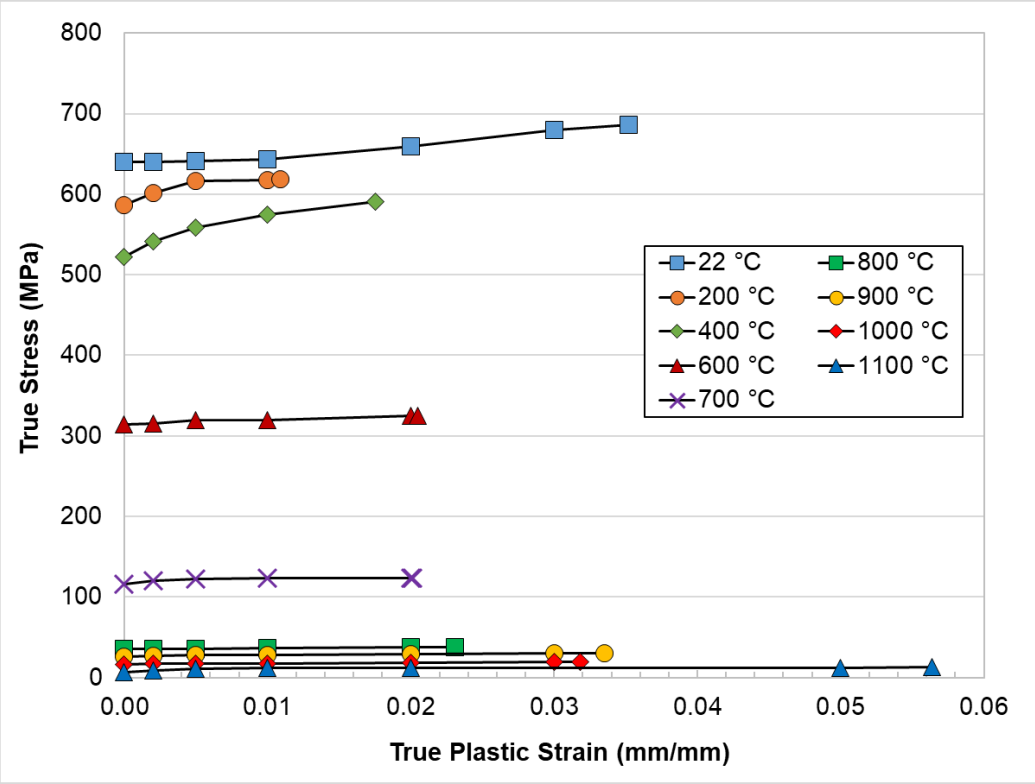


**Figure 32.** Elevated temperature flow stress behavior for HSLA-80 steel base material.

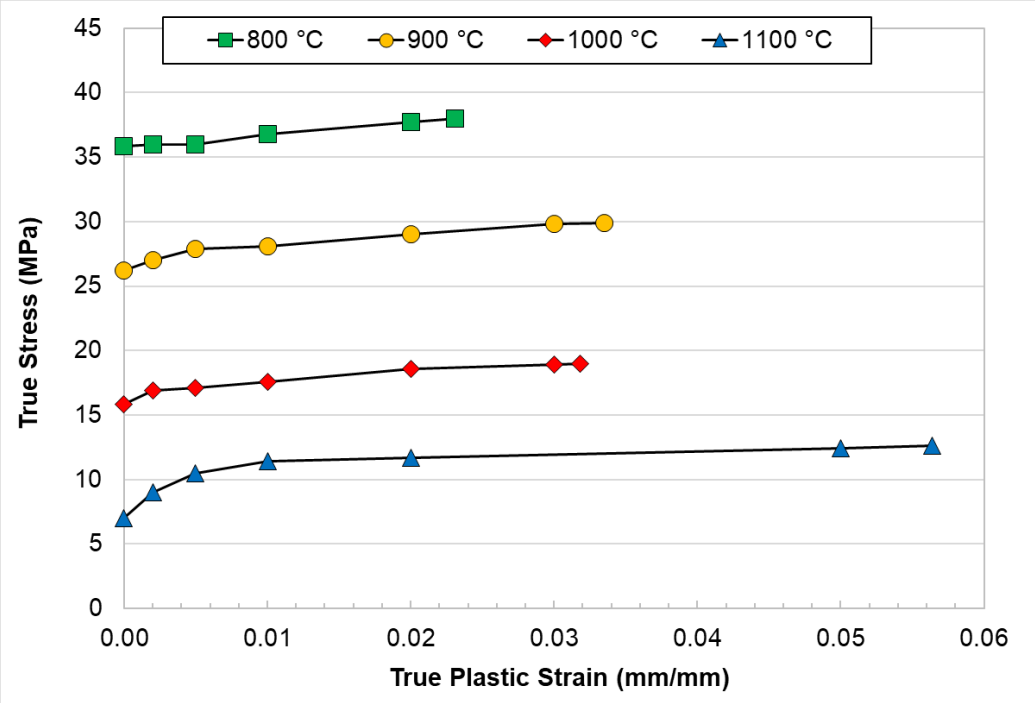


**Figure 33.** Elevated temperature flow stress behavior for HSLA-80 steel base material at test temperatures above the austenitic phase transformation.

Flow stress curves for the thermally cycled HSLA-80 are given in **Figures34-37**. Since these tests were performed under inert atmosphere at NSWCCD, the extensometer was not removed during the tests, and more complete flow stress information is available. Once again, the data are true stresses and strains calculated by conversion from engineering stress-strain data. Such conversions are invalid past the onset of necking, so the terminal data points in **Figures34-37** are at the UTS. All raw data for these figures, along with the engineering fracture strains for the specimens, are found in **Appendix F**.

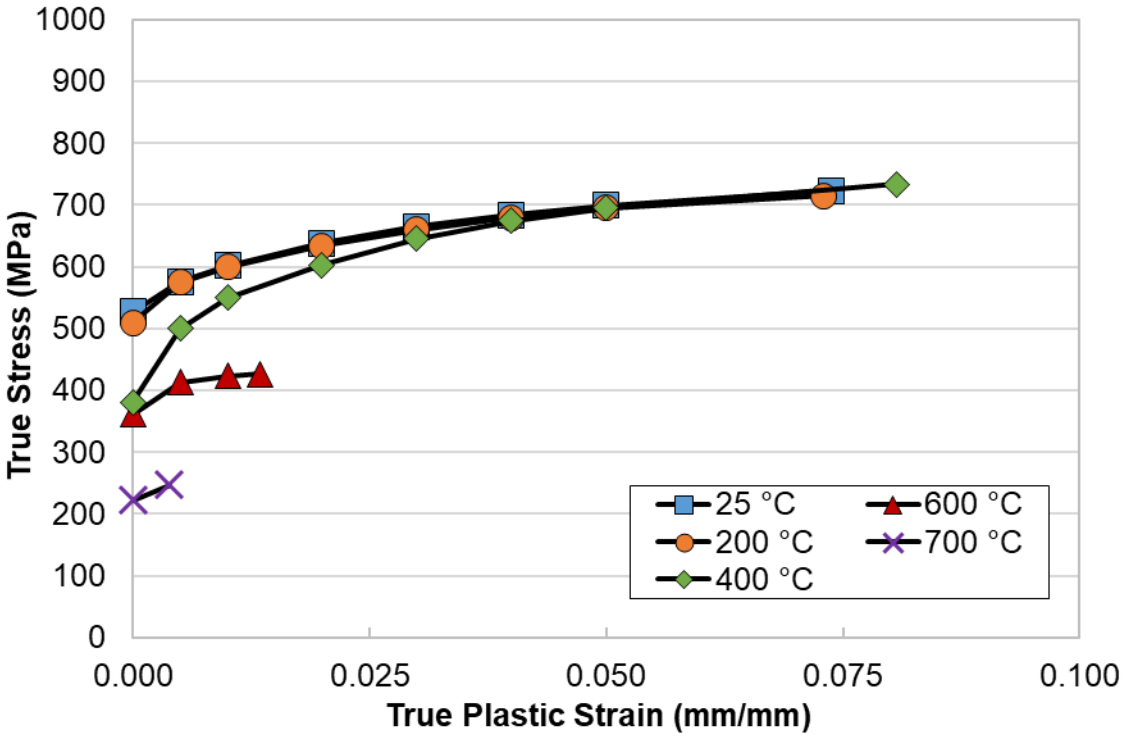


**Figure 34.** Flow stress behavior at various temperatures for HSLA-80 steel after cooling at 1 °C/s (1.8 °F/s) from a peak temperature of 1350 °C (2462 °F). Terminal data points are at the UTS.

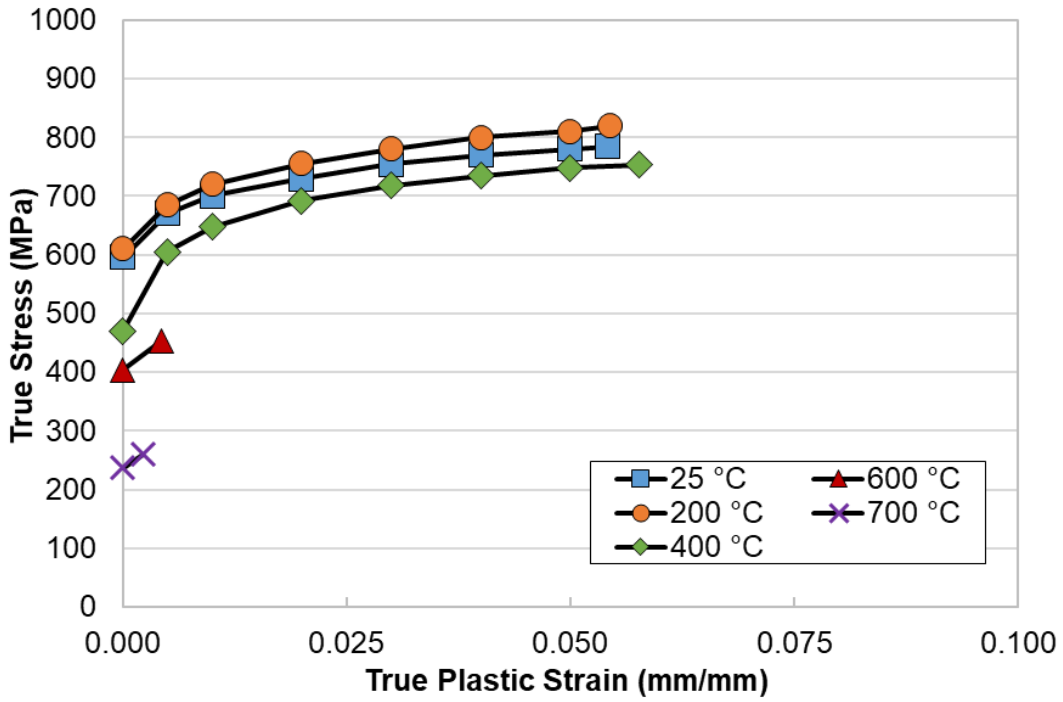


**Figure 35.** Flow stress behavior at various temperatures for HSLA-80 steel after cooling at 10 °C/s (18 °F/s) from a peak temperature of 1350 °C (2462 °F). Terminal data points are at the UTS.

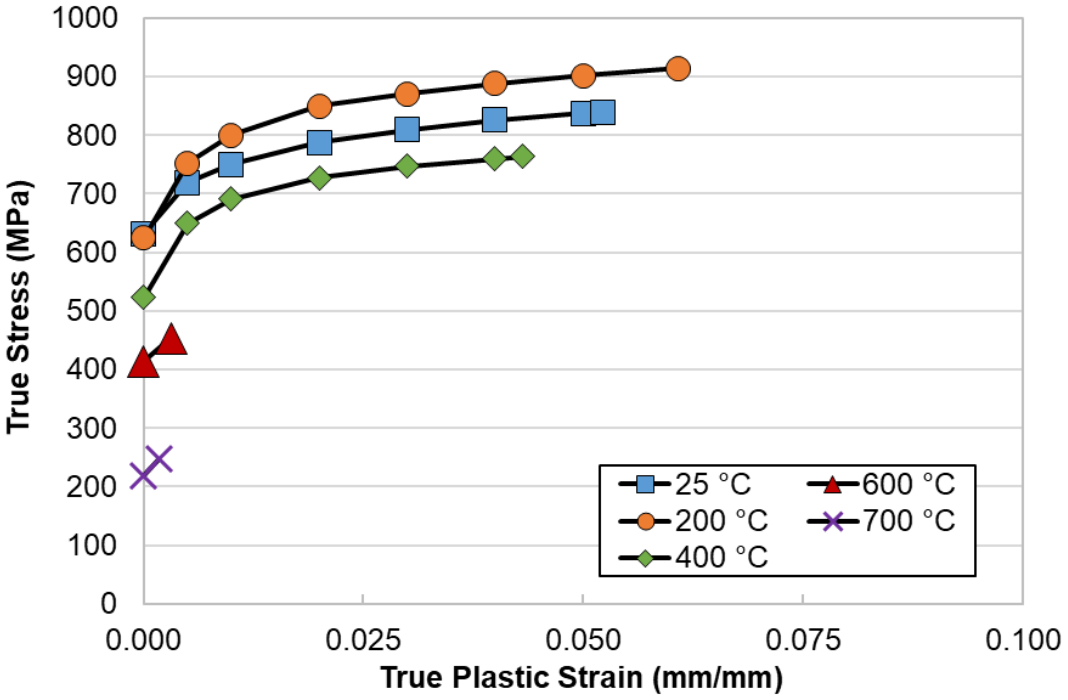


**Figure 36.** Flow stress behavior at various temperatures for HSLA-80 steel after cooling at 25 °C/s (45 °F/s) from a peak temperature of 1350 °C (2462 °F). Terminal data points are at the UTS.

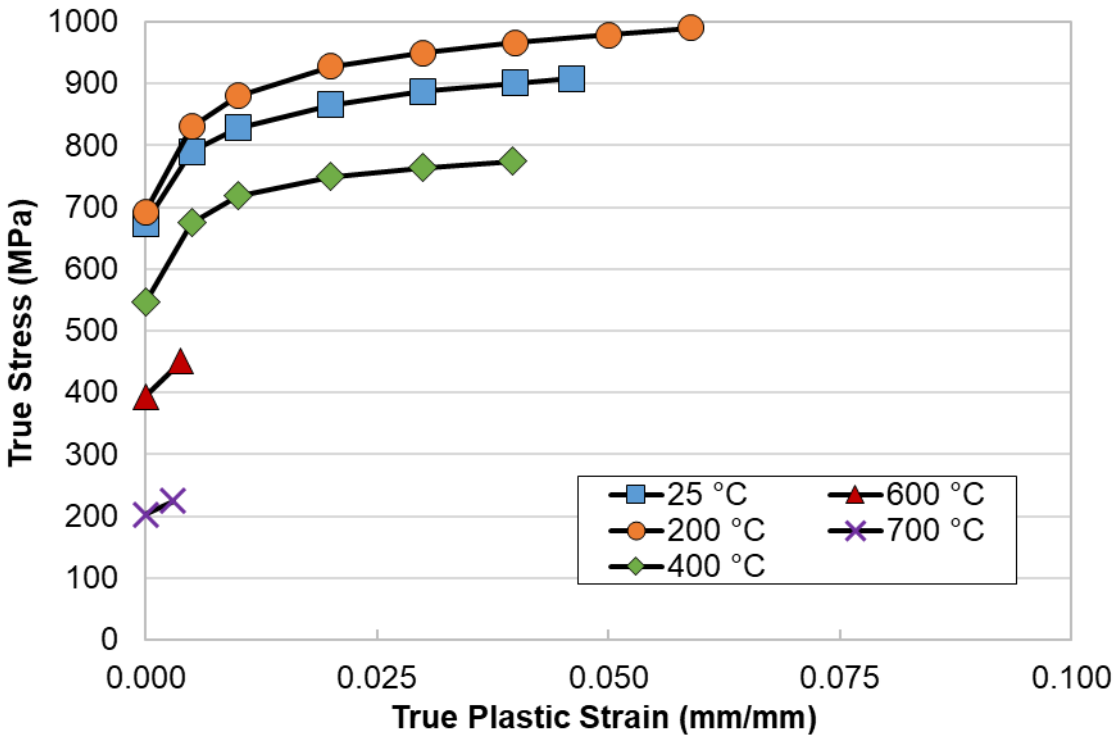


**Figure 37.** Flow stress behavior at various temperatures for HSLA-80 steel after cooling at 100 °C/s (180 °F/s) from a peak temperature of 1350 °C (2462 °F). Terminal data points are at the UTS.

## CONCLUSIONS

Temperature-dependent material property data of a pedigreed plate of HSLA-80 steel from room temperature up to nearly the steel's melting point were determined. The thermo-physical properties investigated include specific heat, thermal diffusivity, thermal conductivity, CTE, and density. Thermo-mechanical properties including yield strength, UTS, and flow stress were also measured. The temperatures associated with on-heating and on-cooling phase transformations and their variation with heating rate, cooling rate, and peak temperature were determined and used to develop welding-focused continuous cooling transformation (CCT) diagrams. Investigation of heat-affected zone microstructures from the CCT specimens and arc welds concluded the analysis. This effort is essential for increasing the fidelity of finite element models used to predict welding-induced distortion and residual stress in marine structures. The data generated in this program have been provided to ESI for immediate incorporation into their *SYSWELD* software. A machine-readable version of the collected data will be uploaded to the University of Michigan's *Materials Commons* data repository <https://materialscommons.org> at a later date.

## APPENDIX

### Appendix A: Plate Conformance Certificate and Chemical Composition for HSLA-80 Steel

TEST CERTIFICATE

ARCELORMITTAL PLATE LLC

PAGE NO: 01 OF 02
FILE NO: 2822-01-02
MILL ORDER NO: 60526-001
MELT NO: R9695
SLAB NO: 39CD
DATE: 08/03/11

SHIP TO:
RONSON TECHNICAL PRODUCTS
C/O HUDSON METAL PROCESSING
1500 NATIONAL CEMETARY ROAD
FLORENCE SC 29506

ORIGINAL

SOLD TO:
ENERGY & PROCESS CORPORATION
A FERGUSON ENTERPRISE
P.O. BOX 125
TUCKER GA 30085-0125

SEND TO: 01-C

PLATE DIMENSIONS / DESCRIPTION

| TOTAL QTY | GAUGE | WIDTH | LENGTH | DESCRIPTION | PIECE WEIGHT |
|---|---|---|---|---|---|
| 1 | 3/16" | 96" | 240" | RECTANGLE | 1225# |

CUSTOMER INFORMATION

CUSTOMER PO: G257-293

PART NO. HSLA80316N

SPECIFICATION(S)

THIS MATERIAL HAS BEEN MANUFACTURED AND TESTED IN ACCORDANCE WITH PURCHASE ORDER REQUIREMENTS AND SPECIFICATION(S).

NAVSE TECH-PUB-T9074 REV 0 YR 02 CL 3 HSLA80-TYI
MIL S-24645A(SH) AMEND#1 CLASS3 HSLA80-TYPE I
NAVSEA TECH. PUBLICATION T9074-BD-GIB-010/0300
REVISION 0 DATED 08/09/02 CLASS 3
HSLA80-TYI WITH ACN 1 OF 11 DEC. 2002
THE MANAGEMENT SYSTEMS FOR MANUFACTURE OF THIS PRODUCT ARE CERTIFIED TO ISO 9001:2000 (CERTIFICATE NO. 30130) AND ISO 14001 (CERTIFICATE NO. 009496).

CHEMICAL COMPOSITION

| | C | MN | P | S | CU | SI | NI | CR | MO |
|---|---|---|---|---|---|---|---|---|---|
| MELT:R9695 | .04 | .56 | .011 | .004 | 1.14 | .26 | .86 | .70 | .20 |
| PROD ANALYSIS | .04 | .56 | .011 | .004 | 1.17 | .26 | .85 | .70 | .20 |
| PROD ANALYSIS | .04 | .58 | .012 | .004 | 1.18 | .27 | .88 | .70 | .20 |

| | V | TI | AL | CB | SB | AS | SN | N |
|---|---|---|---|---|---|---|---|---|
| MELT:R9695 | .002 | .002 | .035 | .028 | .0010 | .0030 | .009 | .0075 |
| PROD ANALYSIS | .002 | .001 | .032 | .027 | .0020 | .0030 | .009 | .0082 |
| PROD ANALYSIS | .002 | .001 | .033 | .030 | .0020 | .0030 | .010 | .0080 |

MANUFACTURE

ELECTRIC FURNACE QUALITY - FINELINE - VACUUM DEGASSED - FINE GRAIN PRACTICE

Q.A. APPROVED
RONSON TECHNICAL PRODUCTS

WE HEREBY CERTIFY THE ABOVE INFORMATION IS CORRECT:

ARCELORMITTAL PLATE LLC
QUALITY ASSURANCE LABORATORY
139 MODENA ROAD
COATESVILLE, PA 19320

Elinore Zaplitny
SUPERVISOR - TEST REPORTING
ELINORE ZAPLITNY

# TEST CERTIFICATE

PAGE NO: 02 OF 02
FILE NO: 2822-01-02
MILL ORDER NO: 60526-001
MELT NO: R9695
SLAB NO: 39CD
DATE: 08/03/11

## HEAT TREAT CONDITION

| MATL OR TEST | HEAT TREAT DESCRIPTION | NOM TEMP | HOLD MINS | COOL MTHD |
|---|---|---|---|---|
| PL/TEST | HARDEN | 1660F | 14 | W.QUENCH |
| PL/TEST | PRECIP.AGED | 1160F | 36 | AIR COOL |

## TENSILE PROPERTIES

| SLAB NO. | LOC | DIR | YIELD STRENGTH PSI X 100 | TENSILE STRENGTH PSI X 100 | ELONGATION GAGE LGTH | % |
|---|---|---|---|---|---|---|
| 39CD | BOT. | TRANS. | 926 | 974 | 2.00" | 27.0 |
| 39CD | TOP | TRANS. | 975 | 1026 | 2.00" | 25.0 |

## GENERAL INFORMATION

ALL STEEL HAS BEEN MELTED AND MANUFACTURED IN THE U.S.A.
PRODUCED IN ACCORDANCE WITH INSPECTION SYSTEM
REQUIREMENTS OF MIL-I-45208A AMEND #1.
NO WELD REPAIR PERFORMED BY ARCELORMITTAL PLATE LLC.
MATERIAL HAS BEEN VACUUM DEGASSED AND CALCIUM TREATED
FOR SULFIDE SHAPE CONTROL.
FINELINE MOD FOR SULPHUR
THE TEST RESULTS SHOWN IN THIS REPORT ARE THE
RESULTS OF TESTING PERFORMED BY OUR ORGANIZATION.
LOW MELTING ALLOYS OR LOW MELTING COMPOUNDS ARE NOT
USED IN THE MANUFACTURE OF ARCELORMITTAL PLATE LLC
PRODUCTS OTHER THAN AS DEOXIDIZING AGENTS.
FOR MORE INFORMATION AND PROCESSING GUIDELINES, REFER TO
WWW.ARCELORMITTAL.COM/PLATEINFORMATION

MERCURY OR MERCURY COMPOUNDS ARE NOT USED IN THE MANUFACTURE OF
ARCELORMITTAL PLATE LLC PRODUCTS.

KNOWINGLY AND WILLFULLY FALSIFYING OR CONCEALING A MATERIAL FACT ON THIS
FORM, OR MAKING FALSE, FICTITIOUS OR FRAUDULENT ENTRIES OR REPRESENTATIONS
HEREIN, COULD CONSTITUTE A FELONY PUNISHABLE UNDER FEDERAL STATUTES.

CERTIFICATE OF CONFORMANCE - ALL ITEMS FURNISHED IN THE SHIPMENT ARE IN
FULL CONFORMANCE WITH ALL P.O. AND SPEC. REQ.; AND THAT THE T.R.'S
REPRESENT THE ACTUAL ATTRIBUTES OF THE ITEMS FURNISHED ON THE ORDER, AND
THAT THE TEST RESULTS ARE IN FULL CONFORMANCE WITH ALL P.O. & SPEC. REQ.
RECORDS TO SUBSTANTIATE THE ABOVE ARE ON FILE IN

OUR PLANT AND WILL BE MAINTAINED FOR A PERIOD OF 7 YRS. FROM THE DATE OF
THE SHIPMENT UNLESS FURNISHED TO THE PURCHASER IN ADVANCE OF OR AT TIME OF
SHIPMENT. WHEN RECORDS ARE RETAINED BY US, WE AGREE TO FURNISH SAME TO THE
PURCHASER AT ANY TIME DURING THE ABOVE PERIOD UPON REQUEST.

B/L #47800 JONES MOTOR CO.

WE HEREBY CERTIFY THE ABOVE
INFORMATION IS CORRECT:

ARCELORMITTAL PLATE LLC
QUALITY ASSURANCE LABORATORY
139 MODENA ROAD
COATESVILLE, PA 19320

Elinore Zaplitny
SUPERVISOR – TEST REPORTING
ELINORE ZAPLITNY

**Table 8.** Chemical Composition of HSLA-80 Base Plate as Measured by OSU

| Element | Wt | Test 1 | Test 2 | Test 3 | Average |
|---|---|---|---|---|---|
| **C** | % | 0.040 | 0.042 | 0.039 | 0.040 |
| **Si** | % | 0.26 | 0.26 | 0.26 | 0.26 |
| **Mn** | % | 0.56 | 0.56 | 0.55 | 0.56 |
| **P** | % | 0.012 | 0.012 | 0.010 | 0.011 |
| **S** | % | 0.0010 | 0.0020 | 0.0006 | 0.0012 |
| **Cr** | % | 0.670 | 0.670 | 0.670 | 0.670 |
| **Mo** | % | 0.200 | 0.200 | 0.200 | 0.200 |
| **Ni** | % | 0.910 | 0.900 | 0.890 | 0.900 |
| **Al** | % | 0.037 | 0.036 | 0.036 | 0.036 |
| **Co** | % | 0.005 | 0.005 | 0.005 | 0.005 |
| **Cu** | % | 1.120 | 1.120 | 1.090 | 1.110 |
| **Nb** | % | 0.031 | 0.031 | 0.029 | 0.030 |
| **Ti** | % | 0.002 | 0.001 | 0.001 | 0.001 |
| **V** | % | 0.003 | 0.003 | 0.003 | 0.003 |
| **W** | % | <0.0005 | <0.005 | <0.005 | <0.005 |
| **Pb** | % | <0.001 | <0.001 | <0.001 | <0.001 |
| **Sn** | % | 0.0110 | 0.0110 | 0.0100 | 0.0107 |
| **As** | % | 0.005 | 0.005 | 0.005 | 0.005 |
| **Zr** | % | <0.001 | <0.001 | <0.001 | <0.001 |
| **Bi** | % | <0.001 | <0.001 | <0.001 | <0.001 |
| **Ca** | % | 0.001 | 0.001 | 0.001 | 0.001 |
| **Ce** | % | <0.001 | <0.001 | <0.001 | <0.001 |
| **Sb** | % | 0.023 | 0.023 | 0.022 | 0.023 |
| **Se** | % | 0.004 | 0.004 | 0.004 | 0.004 |
| **Te** | % | 0.025 | 0.026 | 0.026 | 0.026 |
| **Ta** | % | <0.007 | <0.007 | <0.007 | <0.007 |
| **B** | % | 0.001 | 0.001 | 0.001 | 0.001 |
| **Zn** | % | 0.002 | <0.001 | <0.001 | -- |
| **La** | % | <0.003 | <0.003 | <0.003 | <0.003 |
| **N** | % | 0.011 | 0.010 | 0.009 | 0.010 |
| **Fe** | % | 96.0 | 96.1 | 96.1 | 96.1 |

## Appendix B: Continuous Cooling Transformation Curves

**Table 9.** Austenite Transformation Temperatures Illustrated in **Figure 7**.

| Heating Rate (°C/s) [°F/s] | $A_{c1}$ (°C) [°F] | $A_{c3}$ (°C) [°F] |
|---|---|---|
| 10 [18] | 750 [1382] | 856 [1573] |
| 100 [180] | 775 [1427] | 867 [1593] |
| 200 [360] | 778 [1432] | 866 [1591] |
| 500 [900] | 769 [1416] | 865 [1589] |
| 1000 [1800] | 771 [1419] | 847 [1557] |
| 2000 [2600] | 776 [1429] | 838 [1540] |
| **CTC: 0.75-in. (19.05 mm) nominal plate thickness** | **$A_{c1}$ (°C) [°F]** | **$A_{c3}$ (°C) [°F]** |
| 0.2 [0.36] | 726 [1339] | 850 [1562] |

**Table 10.** Experimentally Measured On-Cooling Transformation Temperatures for HSLA-80 Dilatometry Specimens Cooled from 825 °C (1517 °F). Note: Colors correspond to the transformation products discussed in **Figures 8-14**.

| Cooling Rate (°C/s) [°F/s] | 1 [1.8] | 5 [9] | 10 [18] | 25 [45] | 100 [180] | 200 [360] |
|---|---|---|---|---|---|---|
| Transformation Temperature (°C) [°F] | 761 [1402] | 749 [1380] | 761 [1402] | 760 [1400] | 685 [1265] | 678 [1252] |
| | 653 [1207] | 663 [1225] | 658 [1216] | 624 [1155] | 543 [1009] | 540 [1004] |

**Table 11.** Experimentally Measured On-Cooling Transformation Temperatures for HSLA-80 Dilatometry Specimens Cooled from 1000 °C (1832 °F). Note: Colors correspond to the transformation products discussed in **Figures 8-14**.

| Cooling Rate (°C/s) [°F/s] | 1 [1.8] | 5 [9] | 10 [18] | 25 [45] | 100 [180] | 200 [360] |
|---|---|---|---|---|---|---|
| Transformation Temperature (°C) [°F] | 760 [1400] | 721 [1330] | 694 [1281] | 673 [1243] | 640 [1184] | 634 [1173] |
| | 654 [1209] | 622 [1152] | 596 [1105] | 544 [1011] | 569 [1056] | 556 [1033] |
| | | | | | 507 [945] | 503 [937] |

**Table 12.** Experimentally Measured On-Cooling Transformation Temperatures for HSLA-80 Dilatometry Specimens Cooled from 1150 °C (2102 °F). Note: Colors correspond to the transformation products discussed in **Figures 8-14**.

| Cooling Rate (°C/s) [°F/s] | 1 [1.8] | 5 [9] | 10 [18] | 25 [45] | 100 [180] | 200 [360] |
|---|---|---|---|---|---|---|
| Transformation Temperature (°C) [°F] | 724 [1335] | 665 [1229] | 629 [1164] | 612 [1134] | 551 [1024] | 565 [1049] |
| | 533 [991] | 503 [937] | 487 [909] | 548 [1018] | 486 [907] | 498 [928] |
| | | | | 472 [882] | 412 [774] | 409 [768] |

**Table 13.** Experimentally Measured On-Cooling Transformation Temperatures for HSLA-80 Dilatometry Specimens Cooled from 1350 °C (2462 °F). Note: Colors correspond to the transformation products discussed in **Figures 8-14**.

| **Cooling Rate (°C/s) [°F/s]** | **1 [1.8]** | **5 [9]** | **10 [18]** | **25 [45]** | **100 [180]** | **200 [360]** |
|---|---|---|---|---|---|---|
| **Transformation Temperature (°C) [°F]** | 653 [1207] | 632 [1170] | 608 [1126] | 567 [1053] | 535 [995] | 536 [997] |
| | 524 [975] | 481 [898] | 570 [1058] | 533 [991] | 490 [914] | 490 [914] |
| | | | 488 [910] | 472 [882] | 406 [763] | 404 [759] |
| | | | | 424 [795] | | |

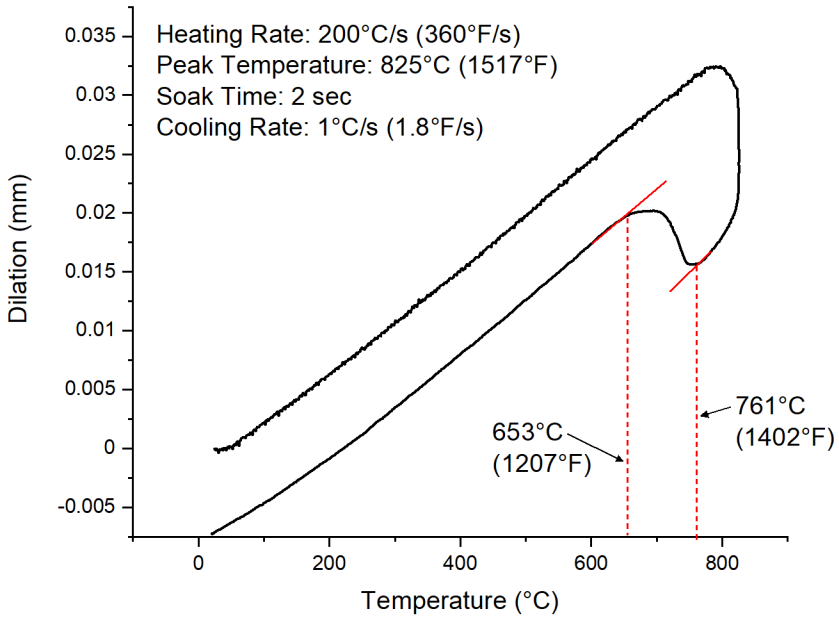


**Figure 38.** Dilation curve from a HSLA-80 Gleeble sample heated to a peak temperature of 825 °C and cooled at 1 °C/s.

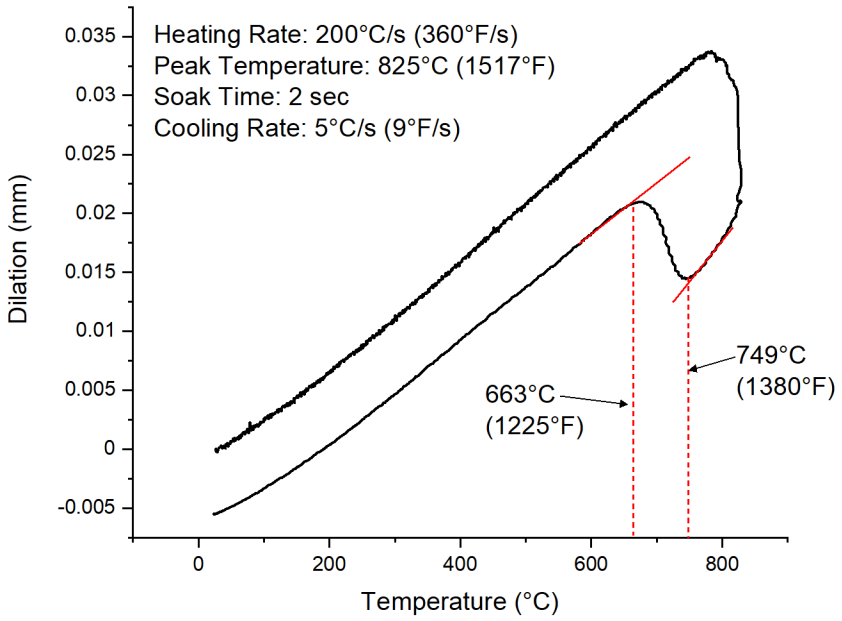


**Figure 39.** Dilation curve from a HSLA-80 Gleeble sample heated to a peak temperature of 825 °C and cooled at 5 °C/s.

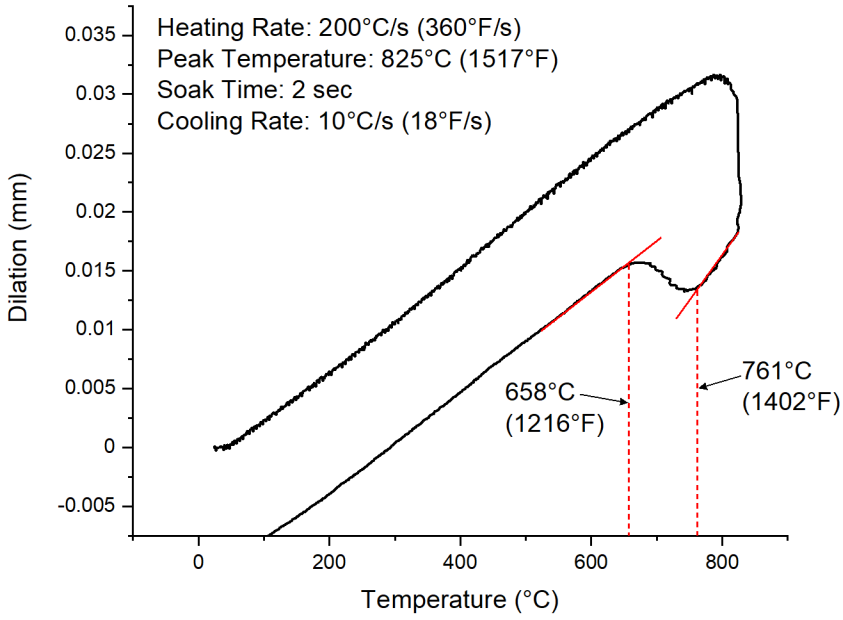


**Figure 40.** Dilation curve from a HSLA-80 Gleeble sample heated to a peak temperature of 825 °C and cooled at 10 °C/s.

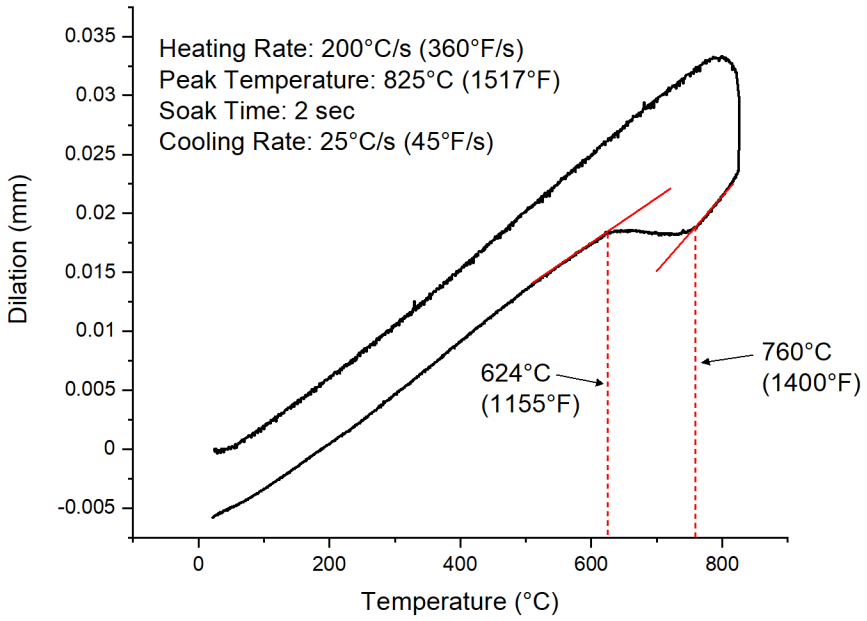


**Figure 41.** Dilation curve from a HSLA-80 Gleeble sample heated to a peak temperature of 825 °C and cooled at 25 °C/s.

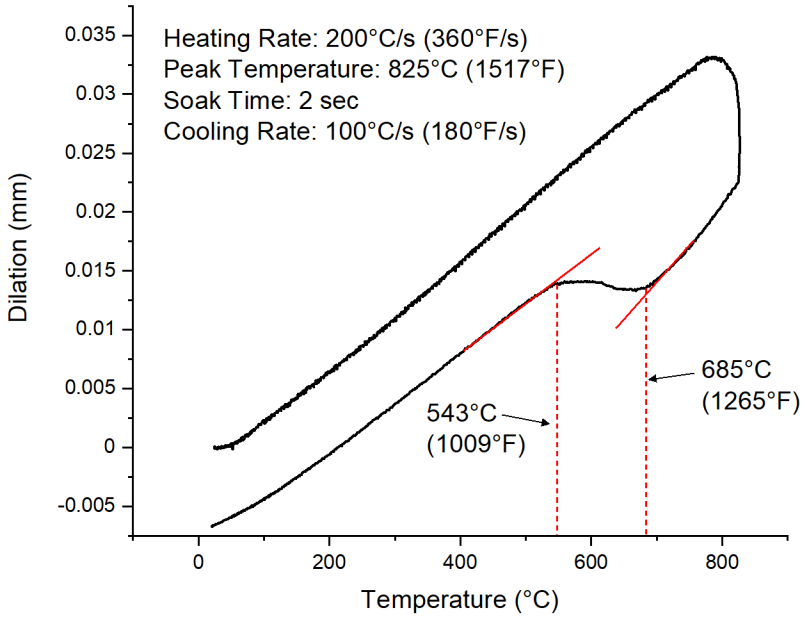


**Figure 42.** Dilation curve from a HSLA-80 Gleeble sample heated to a peak temperature of 825 °C and cooled at 100 °C/s.

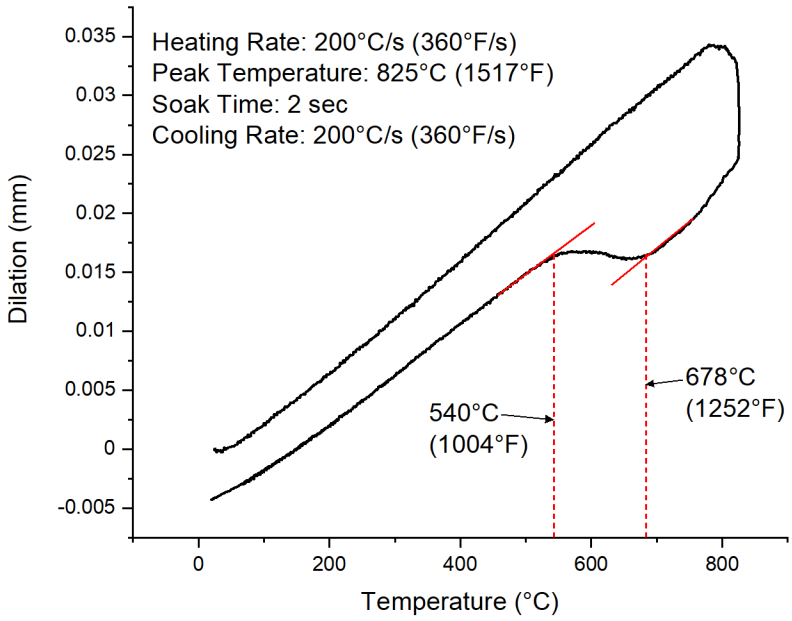


**Figure 43.** Dilation curve from a HSLA-80 Gleeble sample heated to a peak temperature of 825 °C and cooled at 200 °C/s.

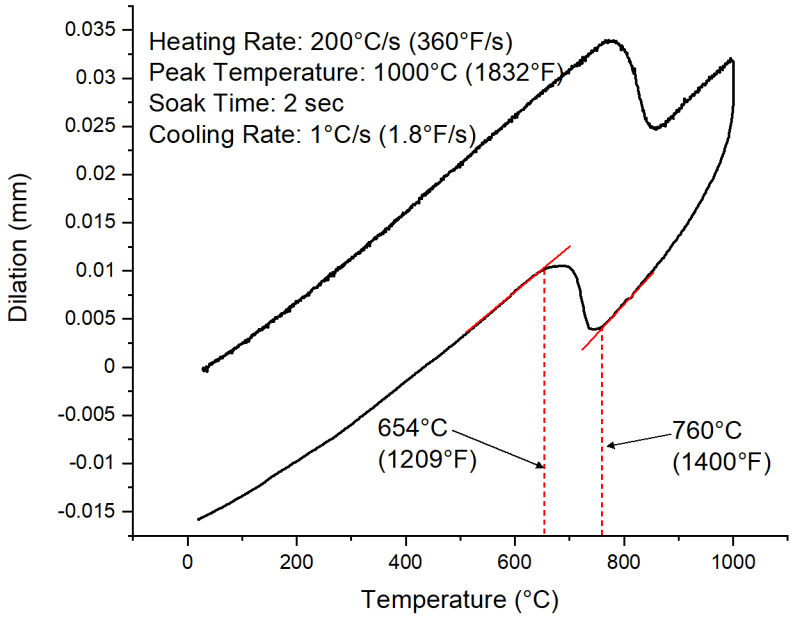


**Figure 44.** Dilation curve from a HSLA-80 Gleeble sample heated to a peak temperature of 1000 °C and cooled at 1 °C/s.

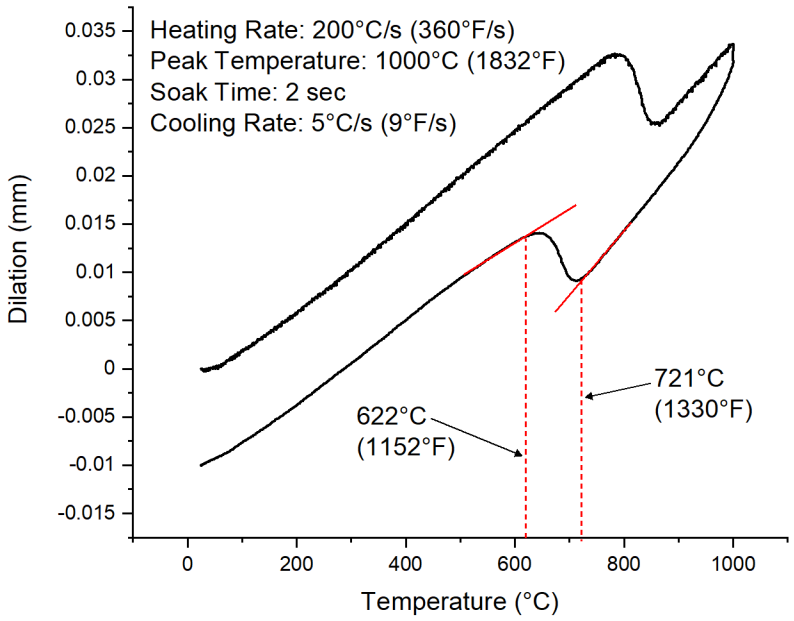


**Figure 45.** Dilation curve from a HSLA-80 Gleeble sample heated to a peak temperature of 1000 °C and cooled at 5 °C/s.

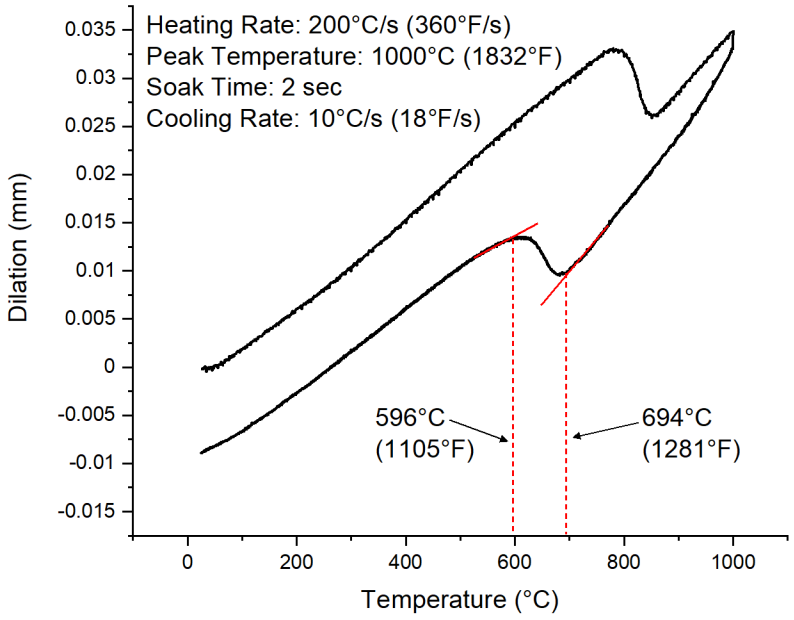


**Figure 46.** Dilation curve from a HSLA-80 Gleeble sample heated to a peak temperature of 1000 °C and cooled at 10 °C/s.

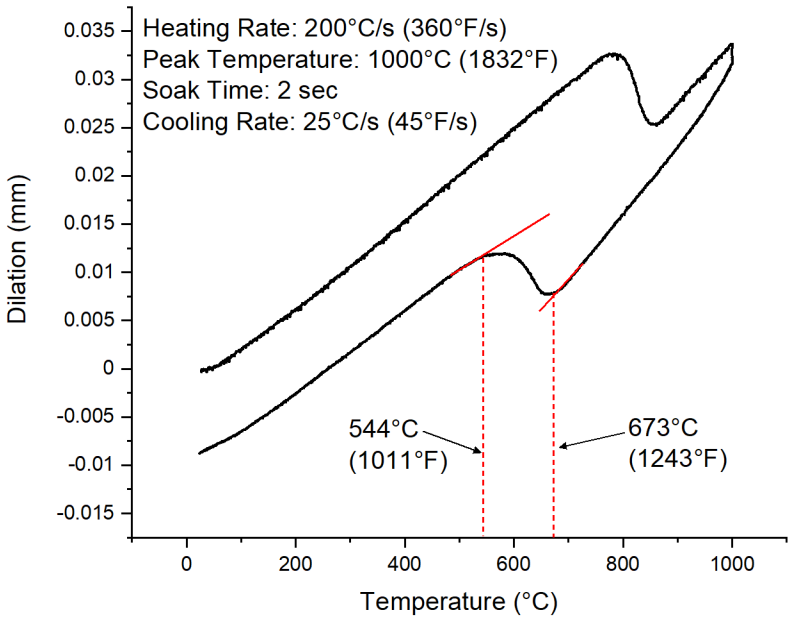


**Figure 47.** Dilation curve from a HSLA-80 Gleeble sample heated to a peak temperature of 1000 °C and cooled at 25 °C/s.

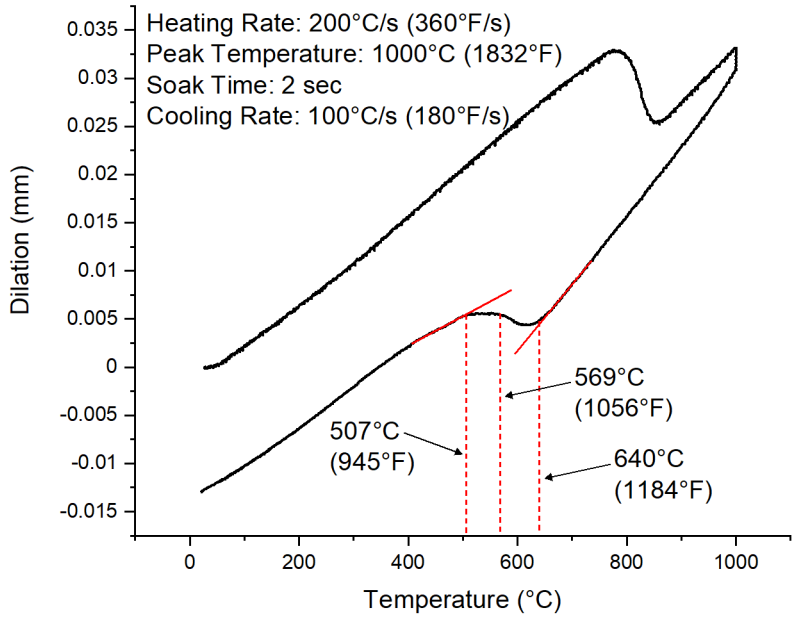


**Figure 48.** Dilation curve from a HSLA-80 Gleeble sample heated to a peak temperature of 1000 °C and cooled at 100 °C/s.

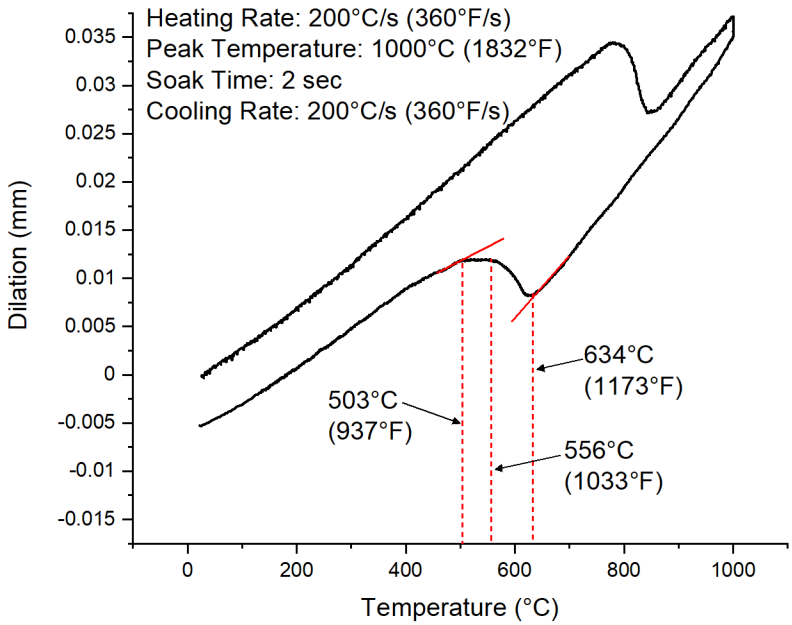


**Figure 49.** Dilation curve from a HSLA-80 Gleeble sample heated to a peak temperature of 1000 °C and cooled at 200 °C/s.

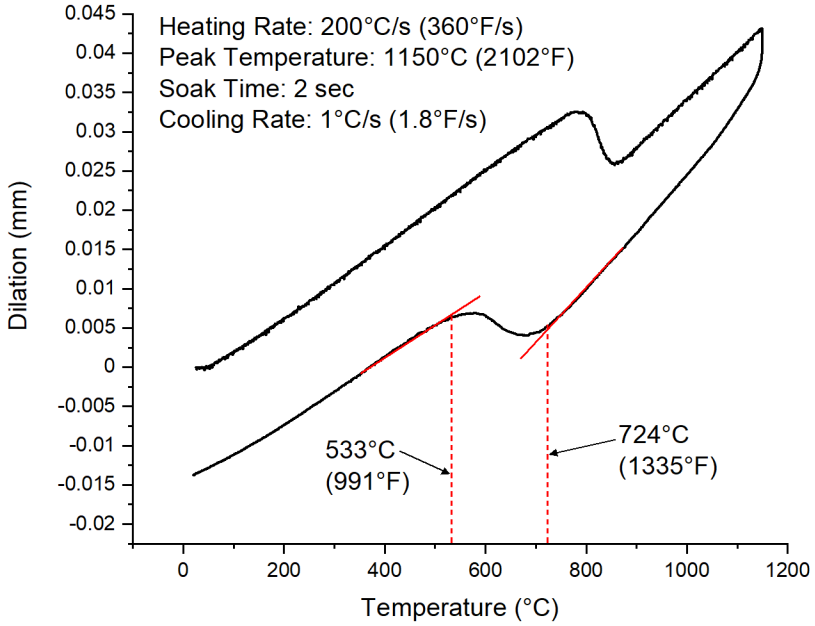


**Figure 50.** Dilation curve from a HSLA-80 Gleeble sample heated to a peak temperature of 1150 °C and cooled at 1 °C/s.

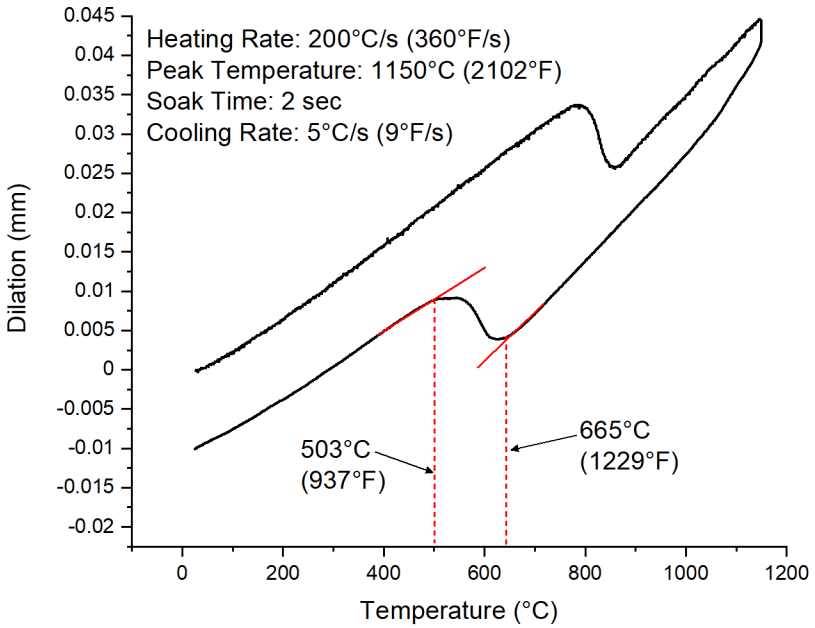


**Figure 51.** Dilation curve from a HSLA-80 Gleeble sample heated to a peak temperature of 1150 °C and cooled at 5 °C/s.

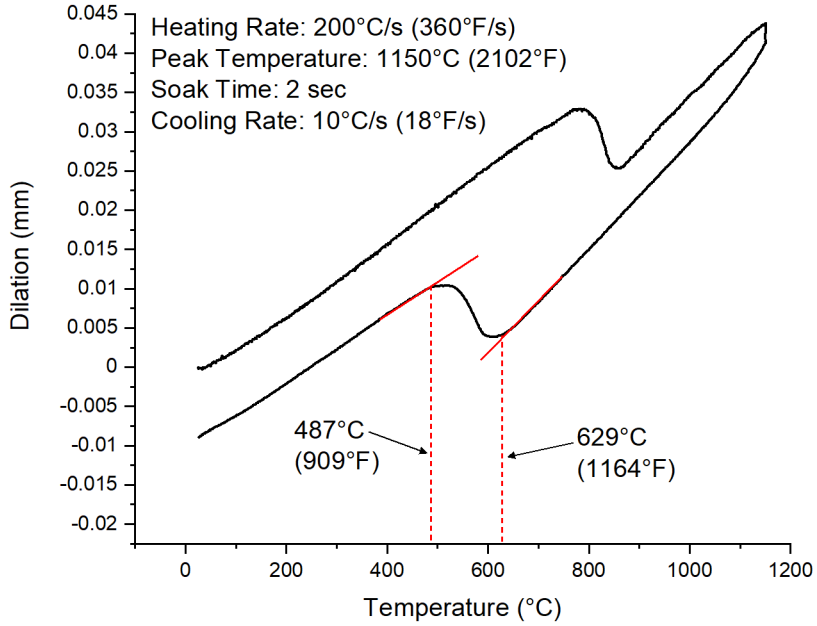


**Figure 52.** Dilation curve from a HSLA-80 Gleeble sample heated to a peak temperature of 1150 °C and cooled at 10 °C/s.

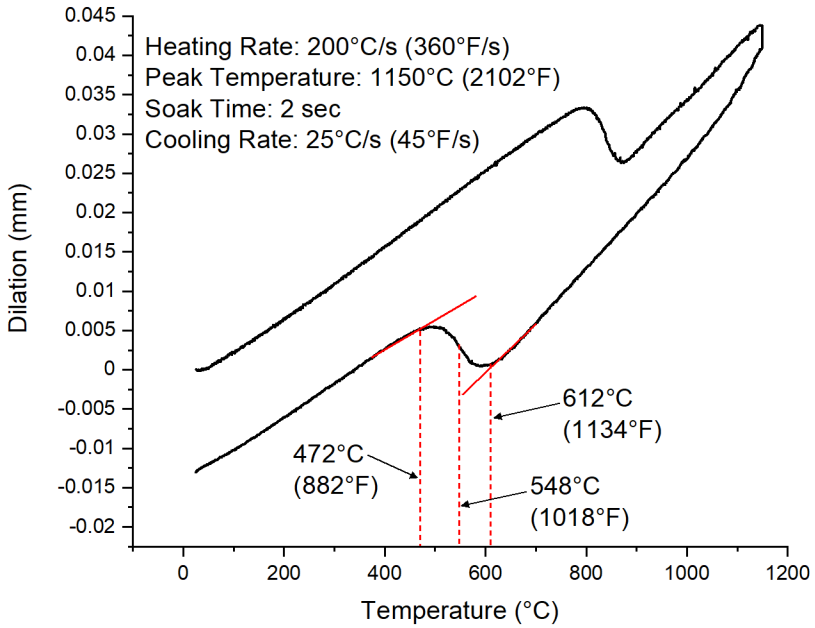


**Figure 53.** Dilation curve from a HSLA-80 Gleeble sample heated to a peak temperature of 1150 °C and cooled at 25 °C/s.

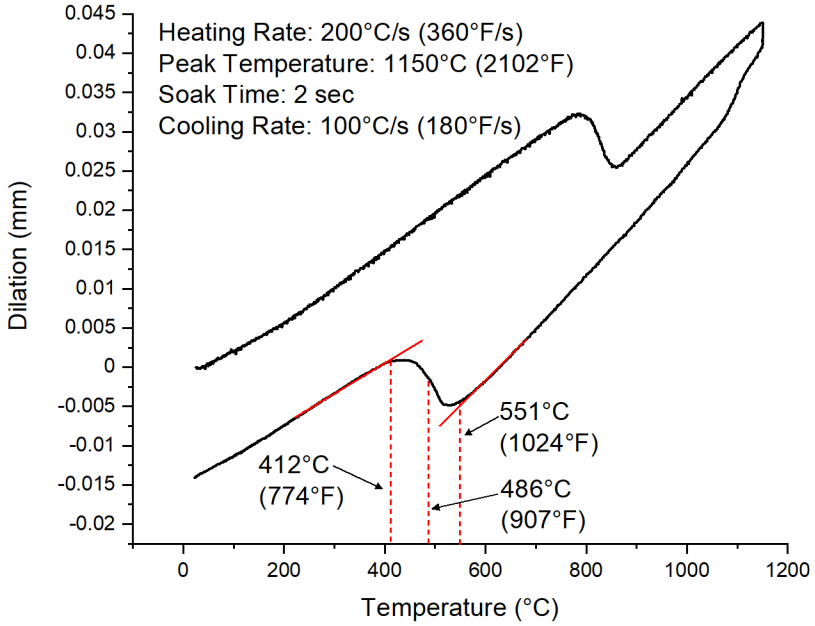


**Figure 54.** Dilation curve from a HSLA-80 Gleeble sample heated to a peak temperature of 1150 °C and cooled at 100 °C/s.

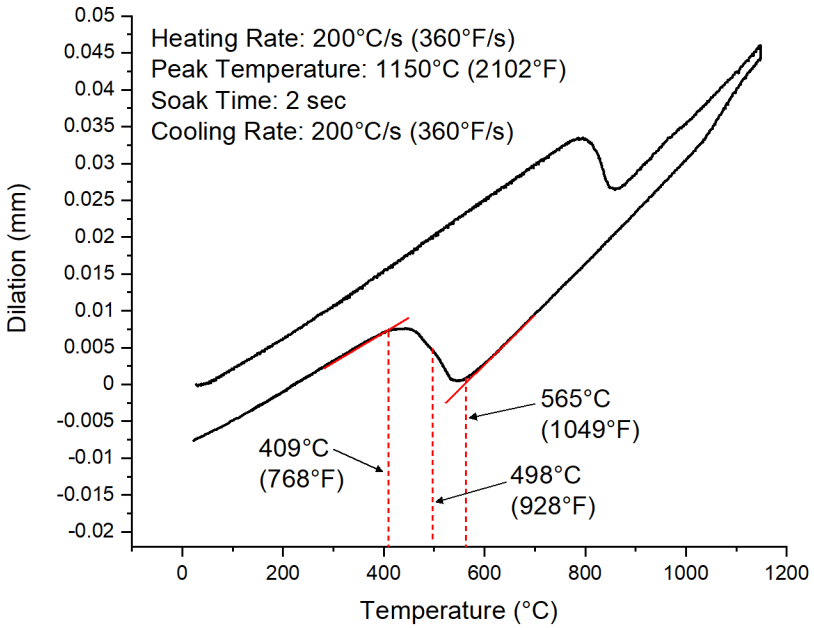


**Figure 55.** Dilation curve from a HSLA-80 Gleeble sample heated to a peak temperature of 1150 °C and cooled at 200 °C/s.

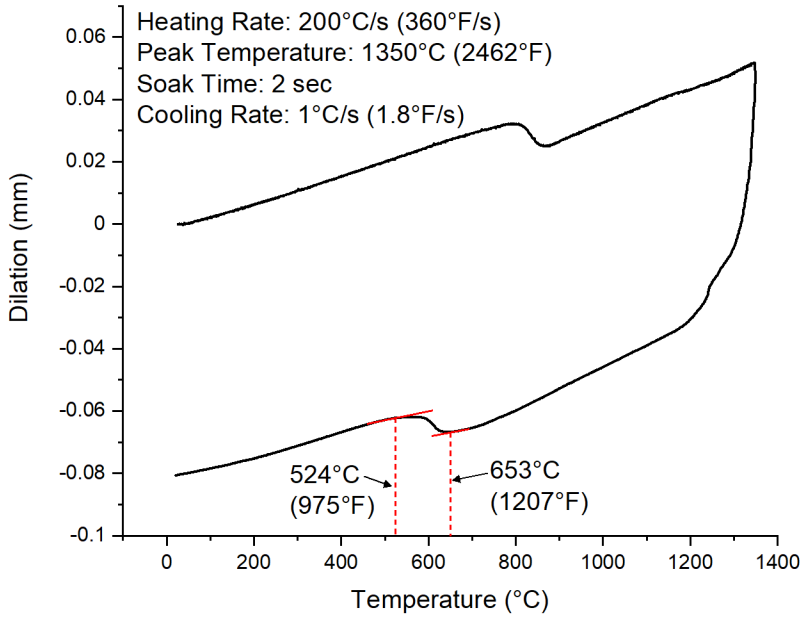


**Figure 56.** Dilation curve from a HSLA-80 Gleeble sample heated to a peak temperature of 1350 °C and cooled at 1 °C/s.

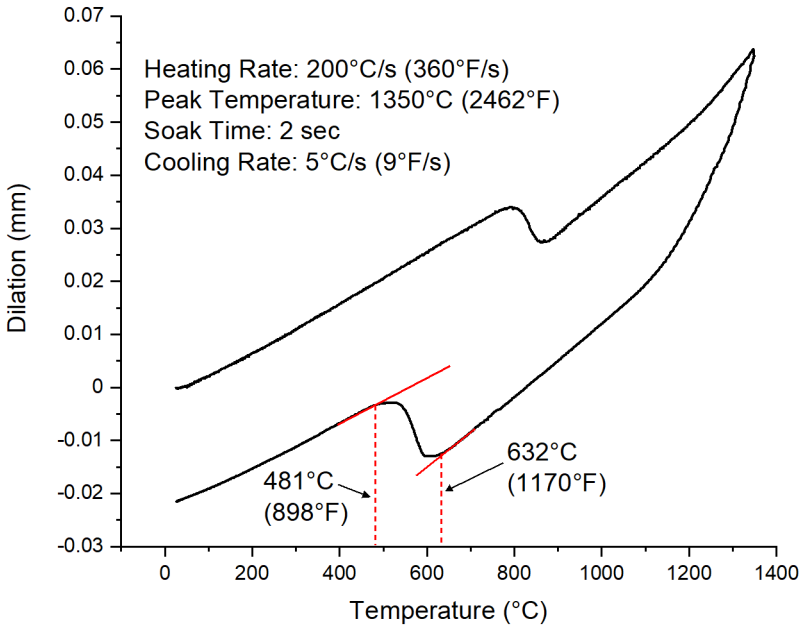


**Figure 57.** Dilation curve from a HSLA-80 Gleeble sample heated to a peak temperature of 1350 °C and cooled at 5 °C/s.

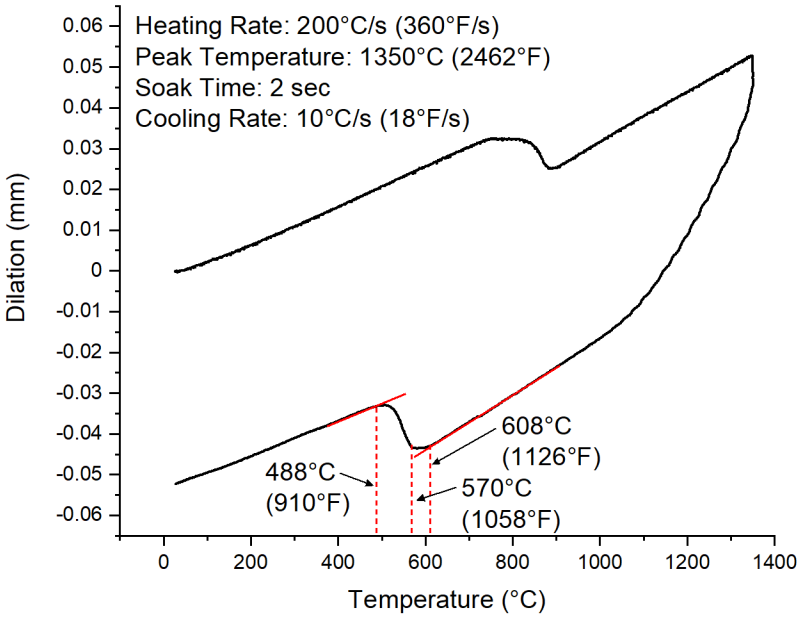


**Figure 58.** Dilation curve from a HSLA-80 Gleeble sample heated to a peak temperature of 1350 °C and cooled at 10 °C/s.

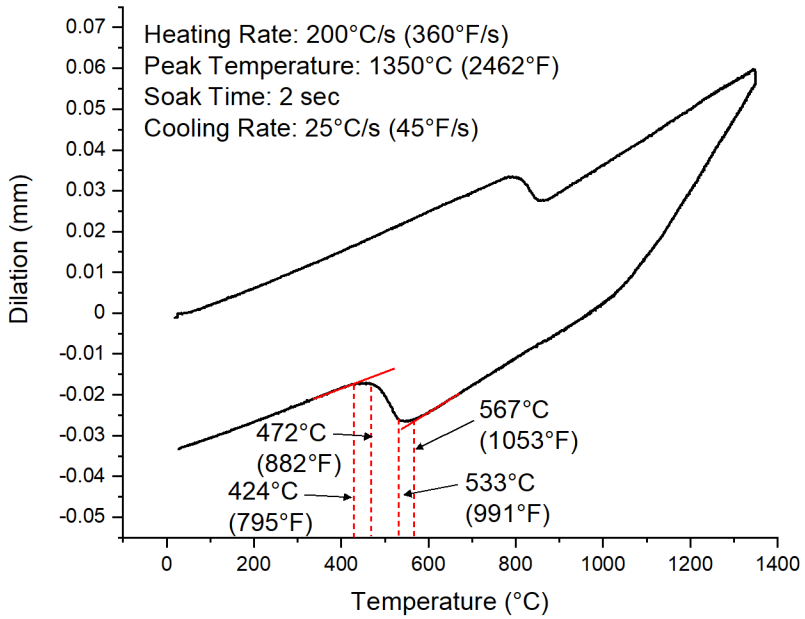


**Figure 59.** Dilation curve from a HSLA-80 Gleeble sample heated to a peak temperature of 1350 °C and cooled at 25 °C/s.

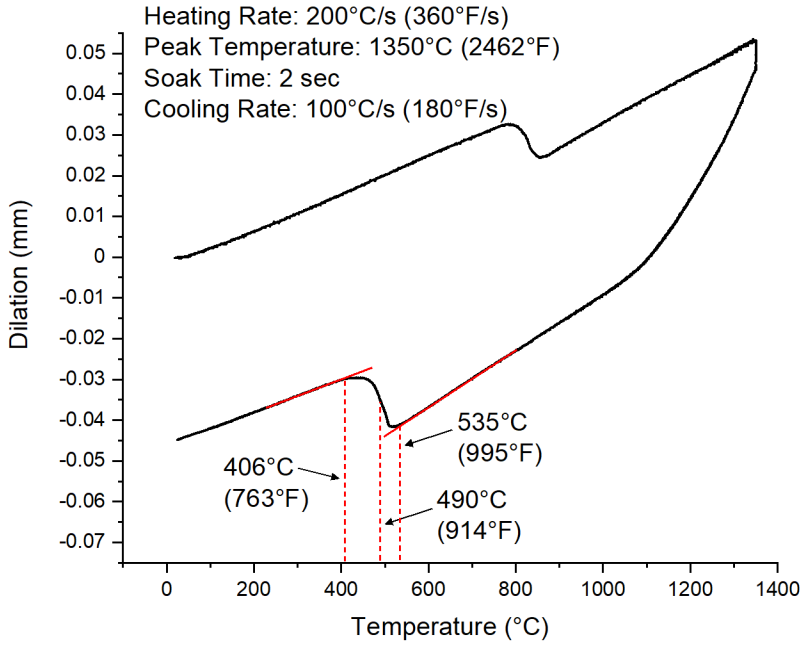


**Figure 60.** Dilation curve from a HSLA-80 Gleeble sample heated to a peak temperature of 1350 °C and cooled at 100 °C/s.

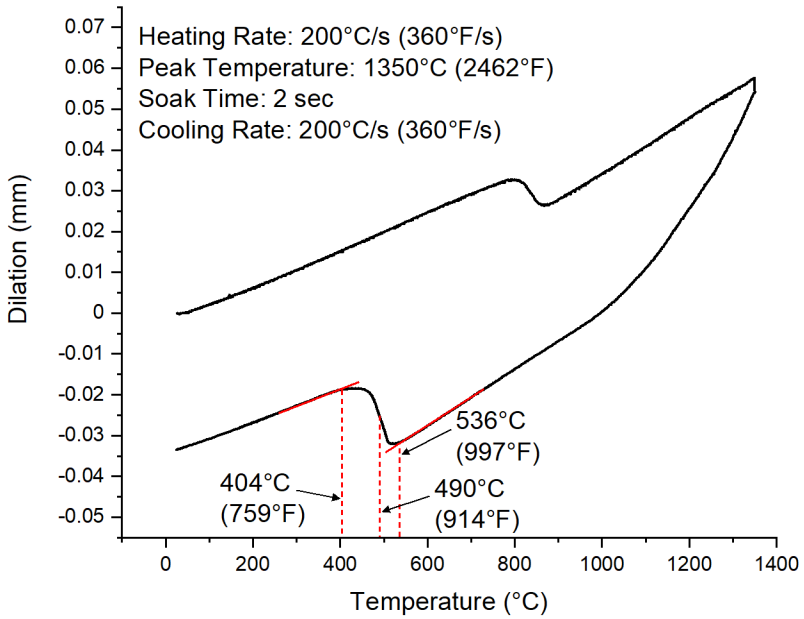


**Figure 61.** Dilation curve from a HSLA-80 Gleeble sample heated to a peak temperature of 1350 °C and cooled at 200 °C/s.

## Appendix C: Representative Microstructures of HSLA-80 CCT Specimens

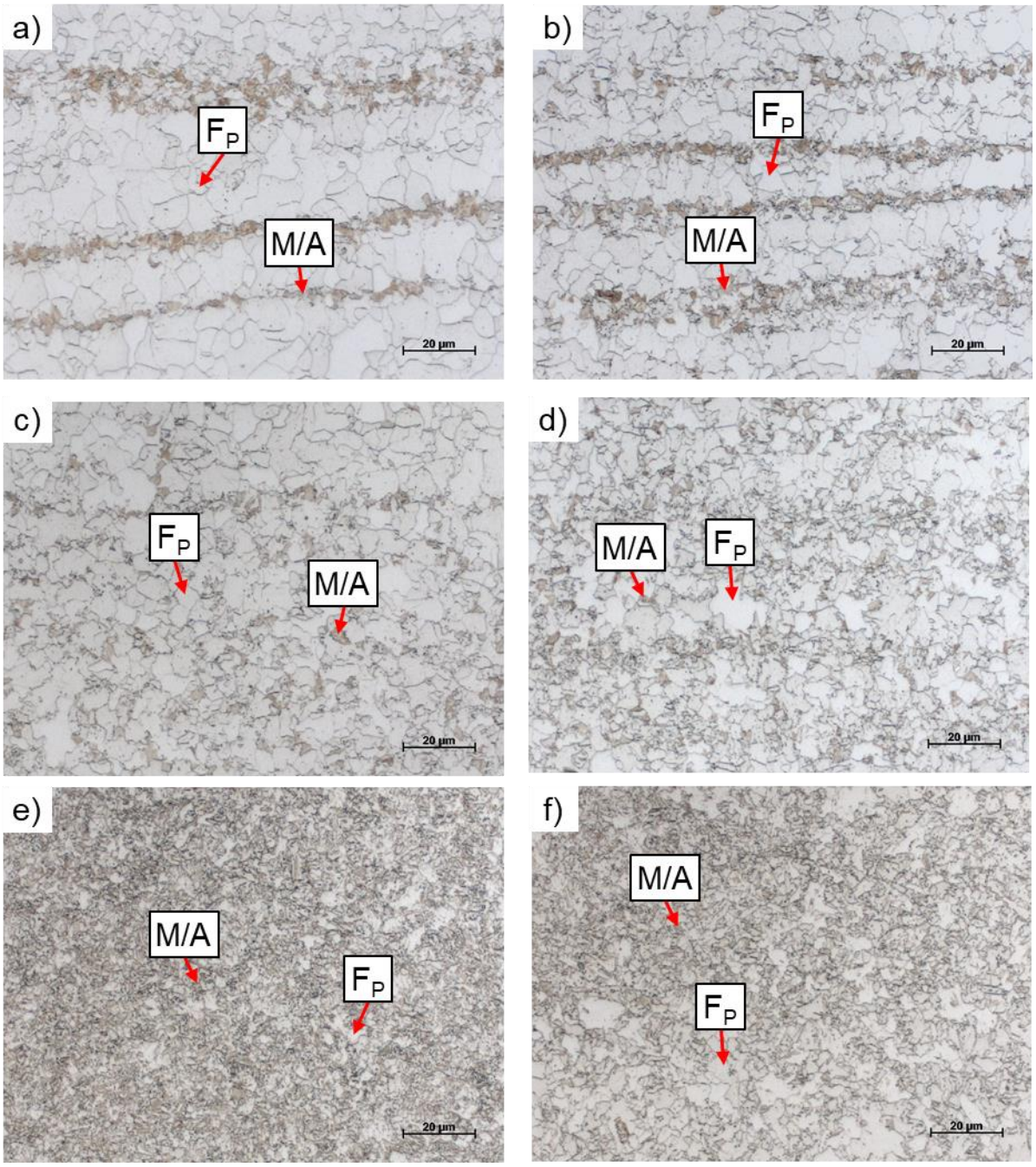


**Figure 62.** Representative microstructures from HSLA-80 dilatometry specimens heated to a peak temperature of 825 °C (1517 °F) and continuously cooled at various rates. **(a-f)**: 1, 5, 10, 25, 100, and 200 °C/s (1.8, 9, 18, 45, 180, and 360 °F/s).

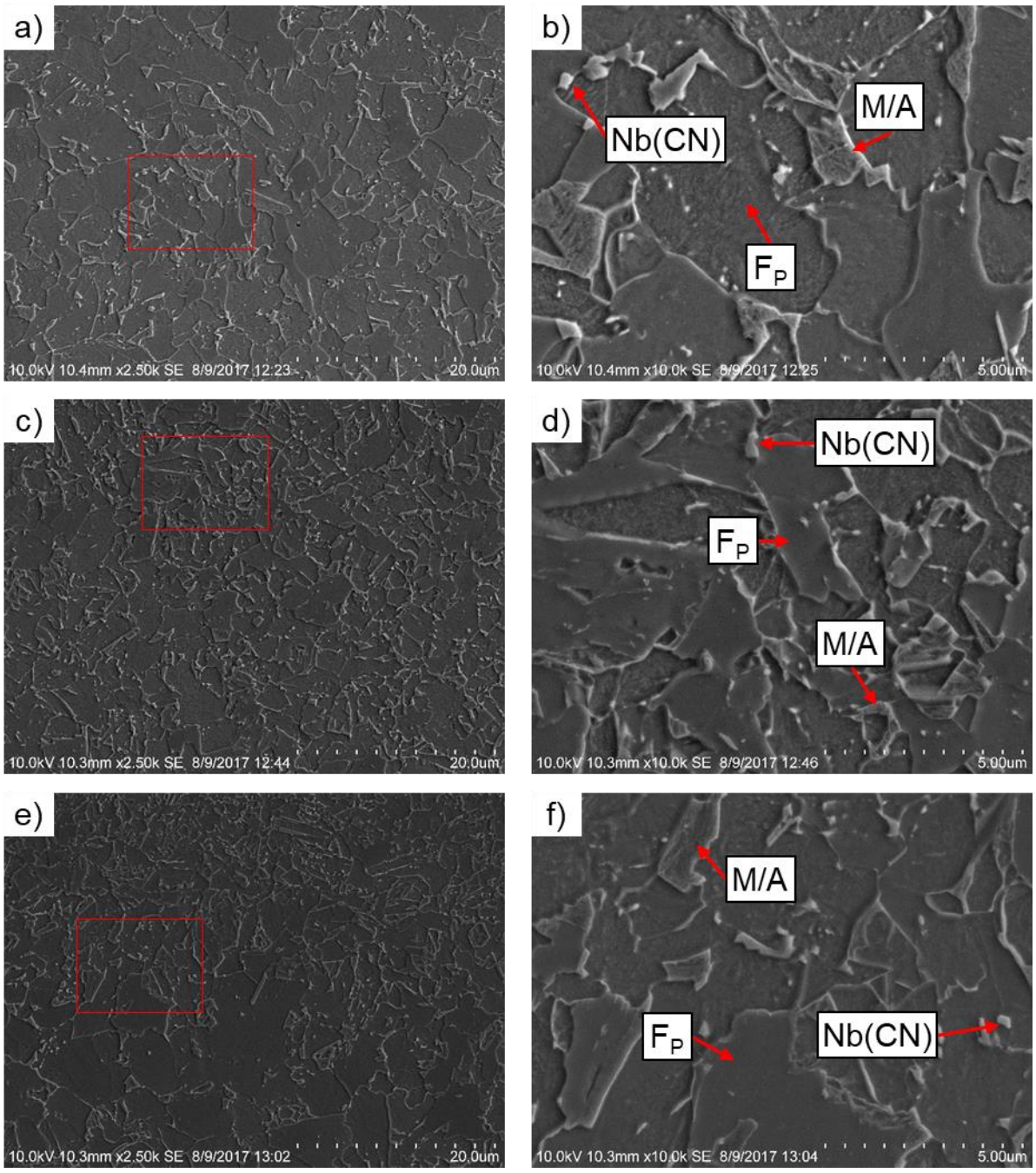


**Figure 63.** SEM images of the microstructure of a HSLA-80 dilatometry specimen heated to a peak temperature of 825 °C (1517 °F) and rapidly cooled. Red boxes overlaid on images in the left column demarcate the location of the higher magnification images in the right column. **(a-f):** 25, 25, 100, 100, 200, 200 °C/s (45, 45, 180, 180, 360, 360 °F/s). Constituents identified as carbonitrides (CN) were not compositionally characterized but are presumed based on the known metallurgy and composition of the alloy.

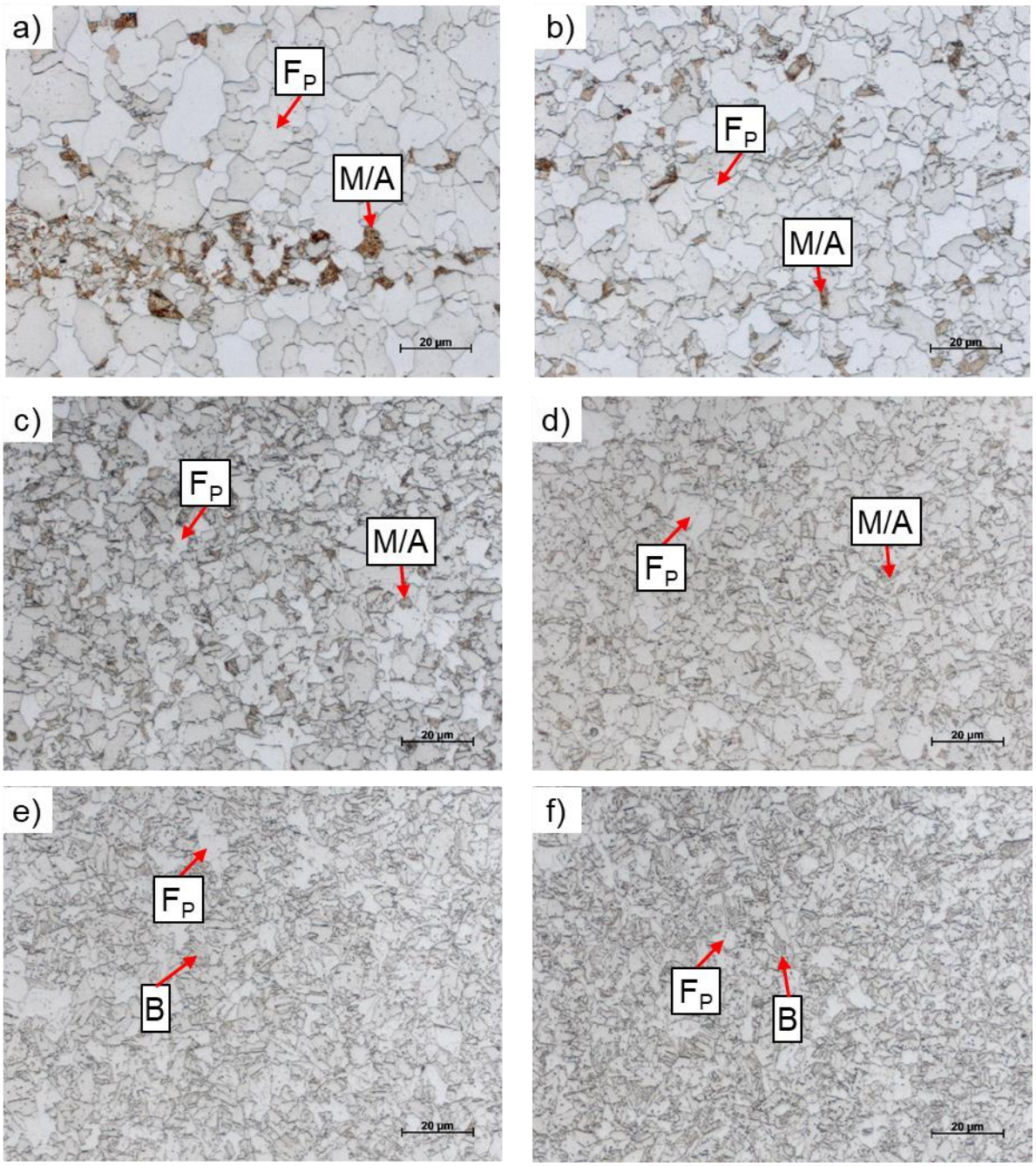


**Figure 64.** Representative microstructures from HSLA-80 dilatometry specimens heated to a peak temperature of 1000 °C (1832 °F) and continuously cooled at various rates. **(a-f)**: 1, 5, 10, 25, 100, and 200 °C/s (1.8, 9, 18, 45, 180, and 360 °F/s).

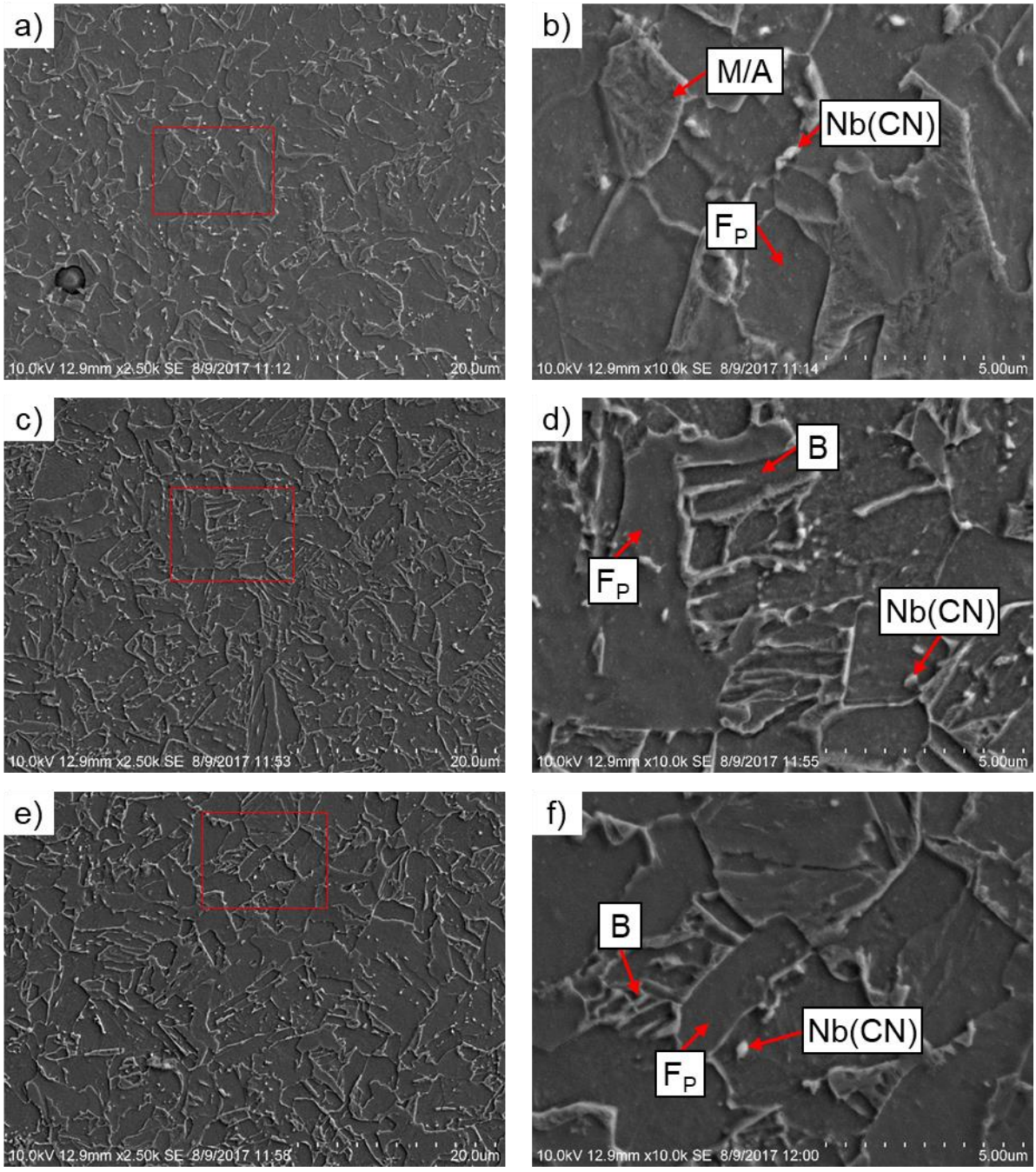


**Figure 65.** SEM images of the microstructure of a HSLA-80 dilatometry specimen heated to a peak temperature of 1000 °C (1832 °F) and rapidly cooled. Red boxes overlaid on images in the left column demarcate the location of the higher magnification images in the right column. **(a-f):** 25, 25, 100, 100, 200, 200 °C/s (45, 45, 180, 180, 360, 360 °F/s). Constituents identified as carbonitrides (CN) were not compositionally characterized but are presumed based on the known metallurgy and composition of the alloy.

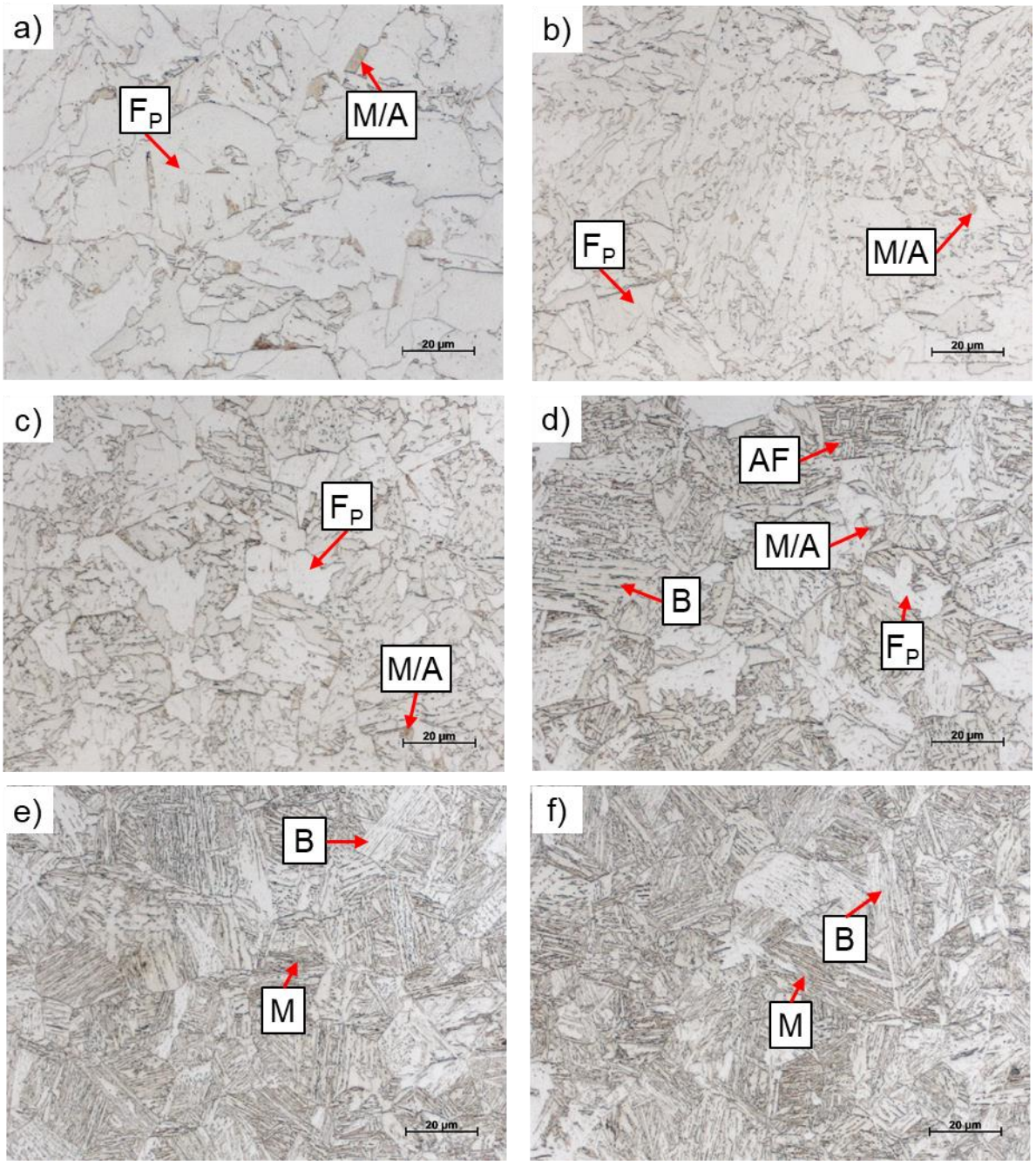


**Figure 66.** Representative microstructures from HSLA-80 dilatometry specimens heated to a peak temperature of 1150 °C (2102 °F) and continuously cooled at various rates. **(a-f)**: 1, 5, 10, 25, 100, and 200 °C/s (1.8, 9, 18, 45, 180, and 360 °F/s).

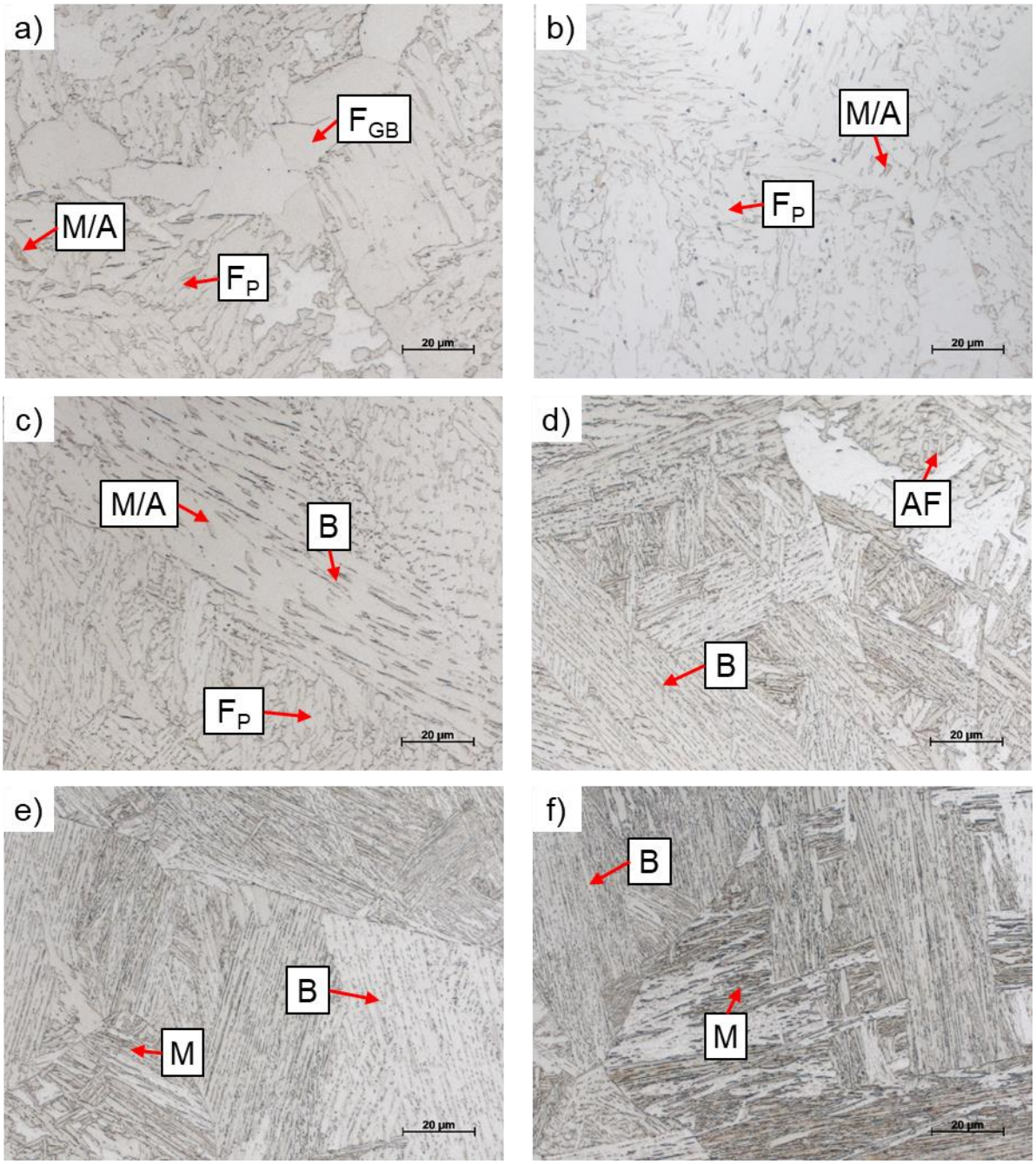


**Figure 67.** Representative microstructures from HSLA-80 dilatometry specimens heated to a peak temperature of 1350 °C (2462 °F) and continuously cooled at various rates. **(a-f)**: 1, 5, 10, 25, 100, and 200 °C/s (1.8, 9, 18, 45, 180, and 360 °F/s).

## Appendix D: Microhardness Measurements

**Table 14.** Vickers Microhardness of HSLA-80 as a Function of Peak Temperature and Cooling Rate. Note: Errors are one standard deviation and values in parenthesis are the number of indents measured.

| Cooling Rate | | Peak Temperature | | | | |
|---|---|---|---|---|---|---|
| | | °C | 825 | 1000 | 1150 | 1350 |
| °C/s | °F/s | °F | 1517 | 1832 | 2102 | 2462 |
| 1 | 1.8 | 173 ± 14 (10) | | 180 ± 10 (10) | 204 ± 11 (10) | 230 ± 6 (10) |
| 5 | 9 | 201 ± 11 (10) | | 191 ± 9 (10) | 222 ± 7 (10) | 233 ± 9 (10) |
| 10 | 18 | 199 ± 10 (10) | | 205 ± 26 (10) | 234 ± 10 (10) | 248 ± 8 (10) |
| 25 | 45 | 208 ± 20 (10) | | 225 ± 15 (10) | 261 ± 12 (10) | 266 ± 22 (10) |
| 100 | 180 | 209 ± 21 (10) | | 248 ± 20 (10) | 282 ± 18 (10) | 302 ± 17 (10) |
| 200 | 360 | 222 ± 14 (10) | | 262 ± 6 (10) | 277 ± 9 (10) | 295 ± 12 (10) |

**Table 15.** Vickers Microhardness Measurements across the Experimental Tee Joint Weldment Illustrated in **Figure 17**. Note: Distance refers to distance from the fusion line, parallel to the indent pattern, and for each pattern the column on the left corresponds to the row closest to the plate surface.

| | Pattern 1 (Pass 1) | | | | | |
|---|---|---|---|---|---|---|
| | Distance (μm) | Hardness ($HV_{200}$) | Distance (μm) | Hardness ($HV_{200}$) | Distance (μm) | Hardness ($HV_{200}$) |
| Weld Metal | -700 | 219 | -585 | 210 | -465 | 222 |
| | -450 | 223 | -335 | 222 | -215 | 218 |
| | -200 | 218 | -85 | 220 | 35 | 252 |
| CGHAZ | 50 | 246 | 165 | 240 | 285 | 253 |
| | 300 | 244 | 415 | 244 | 535 | 234 |
| FGHAZ | 550 | 230 | 665 | 238 | 785 | 220 |
| | 800 | 227 | 915 | 219 | 1035 | 213 |
| ICHAZ | 1050 | 216 | 1165 | 217 | 1285 | 208 |
| | 1300 | 219 | 1415 | 212 | 1535 | 201 |
| | 1550 | 212 | 1665 | 203 | 1785 | 204 |
| | 1800 | 206 | 1915 | 201 | 2035 | 198 |
| | 2050 | 213 | 2165 | 209 | 2285 | 212 |
| Base Metal | 2300 | 222 | 2415 | 226 | 2535 | 222 |
| | 2550 | 232 | 2665 | 227 | 2785 | 232 |
| | 2800 | 235 | 2915 | 236 | 3035 | 246 |

**Pattern 2 (Pass 1)**

| | Distance (µm) | Hardness ($HV_{200}$) | Distance (µm) | Hardness ($HV_{200}$) | Distance (µm) | Hardness ($HV_{200}$) |
|---|---|---|---|---|---|---|
| Weld Metal | -600 | 212 | -142 | 207 | 80 | 249 |
| | -350 | 205 | 108 | 228 | 330 | 252 |
| | -100 | 217 | 358 | 243 | 580 | 242 |
| CGHAZ | 150 | 233 | 608 | 229 | 830 | 229 |
| FGHAZ | 400 | 227 | 858 | 242 | 1080 | 231 |
| | 650 | 241 | 1108 | 223 | 1330 | 223 |
| | 900 | 226 | 1358 | 220 | 1580 | 221 |
| | 1150 | 229 | 1608 | 222 | 1830 | 217 |
| ICHAZ | 1400 | 214 | 1858 | 213 | 2080 | 218 |
| | 1650 | 219 | 2108 | 219 | 2330 | 208 |
| | 1900 | 219 | 2358 | 205 | 2580 | 203 |
| | 2150 | 208 | 2608 | 202 | 2830 | 203 |
| Base Metal | 2400 | 204 | 2858 | 200 | 3080 | 194 |
| | 2650 | 222 | 3108 | 206 | 3330 | 212 |
| | 2900 | 263 | 3358 | 223 | 3580 | 226 |

**Pattern 3**

| | Distance (µm) | Hardness ($HV_{200}$) | Distance (µm) | Hardness ($HV_{200}$) |
|---|---|---|---|---|
| Weld Metal | -438 | 229 | -560 | 231 |
| | -188 | 231 | -310 | 212 |
| CGHAZ | 62 | 246 | -60 | 216 |
| | 312 | 222 | 190 | 239 |
| FGHAZ | 562 | 223 | 440 | 214 |
| | 812 | 208 | 690 | 213 |
| | 1062 | 218 | 940 | 202 |
| | 1312 | 220 | 1190 | 217 |
| ICHAZ | 1562 | 228 | 1440 | 234 |
| | 1812 | 233 | 1690 | 229 |
| | 2062 | 225 | 1940 | 235 |
| | 2312 | 228 | 2190 | 224 |
| | 2562 | 228 | 2440 | 224 |
| | 2812 | 238 | 2690 | 217 |
| | 3062 | 222 | 2940 | 220 |
| Base Metal | 3312 | 220 | 3190 | 228 |
| | 3562 | 228 | 3440 | 211 |
| | 3812 | 222 | 3690 | 231 |
| | 4062 | 221 | 3940 | 213 |
| | 4312 | 216 | 4190 | 213 |

**Table 16.** Vickers Microhardness Measurements across the Butt Joint Weldment Illustrated in **Figure 20**. Note: Distance refers to distance from the fusion line, parallel to the indent pattern, and for each pattern the column on the left corresponds to the row closest to the plate surface.

**Pattern 1 (Pass 1)**

| | Distance (µm) | Hardness ($HV_{200}$) | Distance (µm) | Hardness ($HV_{200}$) | Distance (µm) | Hardness ($HV_{200}$) |
|---|---|---|---|---|---|---|
| Weld Metal | -600 | 203 | -538 | 211 | -455 | 200 |
| | -300 | 193 | -238 | 202 | -155 | 193 |
| CGHAZ | 0 | 210 | 62 | 217 | 145 | 219 |
| | 300 | 218 | 362 | 200 | 445 | 200 |
| FGHAZ | 600 | 191 | 662 | 199 | 745 | 180 |
| | 900 | 187 | 962 | 198 | 1045 | 198 |
| ICHAZ | 1200 | 199 | 1262 | 196 | 1345 | 195 |
| | 1500 | 211 | 1562 | 214 | 1645 | 220 |
| | 1800 | 229 | 1862 | 210 | 1945 | 222 |
| | 2100 | 222 | 2162 | 224 | 2245 | 217 |
| Base Metal | 2400 | 229 | 2462 | 219 | 2545 | 213 |
| | 2700 | 223 | 2762 | 232 | 2845 | 232 |
| | 3000 | 224 | 3062 | 243 | 3145 | 230 |
| | 3300 | 241 | 3362 | 233 | 3445 | 229 |
| | 3600 | 229 | 3662 | 243 | 3745 | 244 |

**Pattern 2 (Pass 1)**

| | Distance (µm) | Hardness ($HV_{200}$) | Distance (µm) | Hardness ($HV_{200}$) | Distance (µm) | Hardness ($HV_{200}$) |
|---|---|---|---|---|---|---|
| Weld Metal | 174 | -350 | 174 | -265 | 180 | -165 |
| | 182 | -50 | 220 | 35 | 213 | 135 |
| CGHAZ | 213 | 250 | 226 | 335 | 202 | 435 |
| FGHAZ | 219 | 550 | 206 | 635 | 220 | 735 |
| | 187 | 850 | 213 | 935 | 192 | 1035 |
| ICHAZ | 204 | 1150 | 195 | 1235 | 216 | 1335 |
| | 196 | 1450 | 206 | 1535 | 190 | 1635 |
| | 191 | 1750 | 200 | 1835 | 187 | 1935 |
| | 206 | 2050 | 184 | 2135 | 200 | 2235 |
| | 180 | 2350 | 175 | 2435 | 204 | 2535 |
| Base Metal | 182 | 2650 | 185 | 2735 | 193 | 2835 |
| | 183 | 2950 | 185 | 3035 | 197 | 3135 |
| | 180 | 3250 | 200 | 3335 | 191 | 3435 |
| | 187 | 3550 | 188 | 3635 | 189 | 3735 |
| | 188 | 3850 | 194 | 3935 | 189 | 4035 |

**Pattern 3 (Pass 2)**

| | Distance (µm) | Hardness ($HV_{200}$) | Distance (µm) | Hardness ($HV_{200}$) | Distance (µm) | Hardness ($HV_{200}$) |
|---|---|---|---|---|---|---|
| Weld Metal | -730 | 217 | -340 | 234 | -550 | 214 |
| | -430 | 221 | -40 | 216 | -250 | 231 |
| | -130 | 214 | 260 | 193 | 50 | 226 |
| CGHAZ | 170 | 232 | 560 | 224 | 350 | 236 |
| FGHAZ | 470 | 211 | 860 | 213 | 650 | 205 |
| | 770 | 205 | 1160 | 203 | 950 | 214 |
| ICHAZ | 1070 | 199 | 1460 | 201 | 1250 | 211 |
| | 1370 | 206 | 1760 | 197 | 1550 | 204 |
| Base Metal | 1670 | 183 | 2060 | 192 | 1850 | 193 |
| | 1970 | 204 | 2360 | 203 | 2150 | 210 |
| | 2270 | 223 | 2660 | 214 | 2450 | 203 |
| | 2570 | 225 | 2960 | 221 | 2750 | 228 |
| | 2870 | 222 | 3260 | 236 | 3050 | 222 |
| | 3170 | 240 | 3560 | 223 | 3350 | 224 |
| | 3470 | 238 | 3860 | 232 | 3650 | 229 |

**Pattern 4 (Pass 2)**

| | Distance (µm) | Hardness ($HV_{200}$) | Distance (µm) | Hardness ($HV_{200}$) | Distance (µm) | Hardness ($HV_{200}$) |
|---|---|---|---|---|---|---|
| Weld Metal | -955 | 246 | -600 | 246 | -710 | 242 |
| | -655 | 243 | -300 | 238 | -410 | 229 |
| | -355 | 239 | 0 | 266 | -110 | 235 |
| | -55 | 249 | 300 | 216 | 190 | 237 |
| CGHAZ | 245 | 229 | 600 | 229 | 490 | 230 |
| FGHAZ | 545 | 234 | 900 | 226 | 790 | 230 |
| | 845 | 221 | 1200 | 213 | 1090 | 217 |
| ICHAZ | 1145 | 207 | 1500 | 208 | 1390 | 207 |
| | 1445 | 202 | 1800 | 185 | 1690 | 181 |
| Base Metal | 1745 | 184 | 2100 | 171 | 1990 | 184 |
| | 2045 | 176 | 2400 | 181 | 2290 | 166 |
| | 2345 | 199 | 2700 | 185 | 2590 | 175 |
| | 2645 | 209 | 3000 | 205 | 2890 | 186 |
| | 2945 | 218 | 3300 | 199 | 3190 | 205 |
| | 3245 | 207 | 3600 | 214 | 3490 | 210 |

## Appendix E: Thermo-Physical Property Datasets for HSLA-80

**Table 17.** Experimentally Measured Specific Heat of HSLA-80

| Temperature (°C) | $c_p$ (J/g-°C) | (°C) | $c_p$ (J/g-°C) | (°C) | $c_p$ (J/g-°C) | (°C) | $c_p$ (J/g-°C) |
|---|---|---|---|---|---|---|---|
| 23 | 0.4558 | 320 | 0.5677 | 620 | 0.7567 | 920 | 0.5151 |
| 30 | 0.4583 | 330 | 0.5719 | 630 | 0.7733 | 930 | 0.5223 |
| 40 | 0.462 | 340 | 0.5760 | 640 | 0.7947 | 940 | 0.5340 |
| 50 | 0.4657 | 350 | 0.5803 | 650 | 0.8131 | 950 | 0.5387 |
| 60 | 0.4693 | 360 | 0.5848 | 660 | 0.8358 | 960 | 0.5458 |
| 70 | 0.4732 | 370 | 0.5890 | 670 | 0.8649 | 970 | 0.5450 |
| 80 | 0.4770 | 380 | 0.5936 | 680 | 0.8826 | 980 | 0.5542 |
| 90 | 0.4810 | 390 | 0.5984 | 690 | 0.9163 | 990 | 0.5591 |
| 100 | 0.4847 | 400 | 0.6031 | 700 | 0.9611 | 1000 | 0.5602 |
| 110 | 0.4883 | 410 | 0.6077 | 710 | 0.9974 | 1010 | 0.5629 |
| 120 | 0.4921 | 420 | 0.6126 | 720 | 1.0358 | 1020 | 0.5659 |
| 130 | 0.4958 | 430 | 0.6179 | 730 | 1.0778 | 1030 | 0.5686 |
| 140 | 0.4995 | 440 | 0.6238 | 740 | 1.1182 | 1040 | 0.5709 |
| 150 | 0.5032 | 450 | 0.6296 | 750 | 1.2131 | 1050 | 0.5730 |
| 160 | 0.5068 | 460 | 0.6352 | 760 | 1.2680 | 1060 | 0.5747 |
| 170 | 0.5106 | 470 | 0.6411 | 770 | 1.1121 | 1070 | 0.5761 |
| 180 | 0.5142 | 480 | 0.6472 | 780 | 0.9898 | 1080 | 0.5773 |
| 190 | 0.5179 | 490 | 0.6541 | 790 | 0.9136 | 1090 | 0.5782 |
| 200 | 0.5217 | 500 | 0.6614 | 800 | 0.8730 | 1100 | 0.5788 |
| 210 | 0.5253 | 510 | 0.6692 | 810 | 0.8541 | 1110 | 0.5792 |
| 220 | 0.5290 | 520 | 0.6778 | 820 | 0.8488 | 1120 | 0.5794 |
| 230 | 0.5330 | 530 | 0.6845 | 830 | 0.8640 | 1130 | 0.5794 |
| 240 | 0.5375 | 540 | 0.6877 | 840 | 0.8777 | 1140 | 0.5792 |
| 250 | 0.5410 | 550 | 0.6958 | 850 | 0.8749 | 1150 | 0.5788 |
| 260 | 0.5447 | 560 | 0.7020 | 860 | 0.8026 | 1160 | 0.5783 |
| 270 | 0.5485 | 570 | 0.7035 | 870 | 0.6776 | 1170 | 0.5774 |
| 280 | 0.5522 | 580 | 0.7142 | 880 | 0.5790 | 1180 | 0.5766 |
| 290 | 0.5559 | 590 | 0.7216 | 890 | 0.5217 | 1190 | 0.5757 |
| 300 | 0.5597 | 600 | 0.7329 | 900 | 0.5131 | 1200 | 0.5747 |
| 310 | 0.5636 | 610 | 0.7433 | 910 | 0.5075 | | |

**Table 18.** Experimentally Measured Thermal Properties of HSLA-80

| Temperature (°C) | Thermal Diffusivity ($cm^2/sec$) | Density ($g/cm^3$) | Thermal Conductivity (W/cm-°C) |
|---|---|---|---|
| **23** | 0.11666 | 0.78234 | 0.4160 |
| **50** | 0.11467 | 7.8221 | 0.4177 |
| **100** | 0.11167 | 7.8070 | 0.4226 |
| **200** | 0.10680 | 7.7745 | 0.4332 |
| **300** | 0.09930 | 7.7405 | 0.4302 |
| **400** | 0.09041 | 7.7049 | 0.4201 |
| **500** | 0.08111 | 7.6679 | 0.4114 |
| **600** | 0.07075 | 7.6314 | 0.3957 |
| **700** | 0.05884 | 7.5957 | 0.4295 |
| **800** | 0.03957 | 7.5716 | 0.2616 |
| **900** | 0.06101 | 7.6063 | 0.2381 |
| **1000** | 0.06635 | 7.5571 | 0.2809 |
| **1100** | 0.07069 | 7.5089 | 0.3072 |
| **1200** | 0.07355 | 7.4609 | 0.3154 |

## Appendix F: Thermo-Mechanical Properties

**Table 19.** Assumed Elevated Temperature Elastic Modulus for HSLA-80 Base Material. Note: Data are based on an assumed room temperature modulus of 210 GPa (30.5 Msi) as shown in **Figure 28**.

| Temperature (°C [°F]) | Fraction of Room Temperature Modulus | Elastic Modulus (GPa [Msi]) |
|---|---|---|
| **23 (73)** | 1.0000 | 210 (30.5) |
| **100 (212)** | 1.0000 | 210 (30.5) |
| **200 (392)** | 0.9000 | 189 (27.4) |
| **300 (572)** | 0.8000 | 168 (24.4) |
| **400 (752)** | 0.7000 | 147 (21.3) |
| **500 (932)** | 0.6000 | 126 (18.3) |
| **600 (1112)** | 0.3100 | 65 (9.4) |
| **700 (1292)** | 0.1300 | 27 (4.0) |
| **800 (1472)** | 0.0900 | 19 (2.7) |
| **900 (1652)** | 0.0675 | 14 (2.1) |
| **1000 (1832)** | 0.0450 | 9 (1.4) |
| **1100 (2012)** | 0.0225 | 5 (0.7) |
| **1200 (2192)** | 0.0000 | 0 (0) |

**Table 20.** Elevated Temperature Mechanical Properties of HSLA-80 Base Material. Note: Data as shown in **Figures 29-30**.

| Specimen ID | Test Temperature (°C [°F]) | Yield Strength (MPa [ksi]) | Tensile Strength (MPa [ksi]) | Elongation in 2 in. (%) |
|---|---|---|---|---|
| 4230-1FTT | 23 (74) | 640 (92.8) | 703 (101.9) | 19.5 |
| 4230-1ETT1 | 200 (392) | 587 (85.2) | 650 (94.3) | 16.5 |
| 4230-1ETT2 | 400 (752) | 522 (75.7) | 605 (87.8) | 19.0 |
| 4230-1ETT3 | 600 (1112) | 314 (45.5) | 348 (50.4) | 25.0 |
| 4230-1ETT4 | 700 (1292) | 116 (16.8) | 142 (20.6) | 27.0 |
| 4230-1ETT5A1 | 800 (1472) | 36 (5.2) | 53 (7.7) | 86.0 |
| 4230-1ETT6A1 | 900 (1652) | 26 (3.8) | 47 (6.8) | 20.0 |
| 4230-1ETT7A1 | 1000 (1832) | 16 (2.3) | 30 (4.4) | 25.5 |
| 4230-1ETT8B | 1100 (2012) | 7 (1.0) | 20 (2.9) | 32.0 |

**Table 21.** Yield Strength of Simulated HSLA-80 CGHAZs after Heating to 1350 °C (2462 °F) and Cooling at Various Rates. Note: Data as illustrated in **Figure 31**.

| Temperature (°C) [°F] | Yield Strength (MPa) | | | |
|---|---|---|---|---|
| | 1 °C/s Cooling | 10 °C/s Cooling | 25 °C/s Cooling | 100 °C/s Cooling |
| 25 [77] | 527 | 596 | 632 | 674 |
| 200 [392] | 509 | 610 | 625 | 692 |
| 400 [752] | 381 | 470 | 523 | 546 |
| 600 [1112] | 361 | 404 | 414 | 394 |
| 700 [1292] | 222 | 237 | 219 | 203 |

**Table 22.** On-heating Flow Behavior of HSLA-80 Base Material. Note: Data as shown in **Figures 32-33**.

| 22 °C (72 °F) | | 200 °C (392 °F) | | 400 °C (752 °F) | | 600 °C (1112 °F) | | 700 °C (1292 °F) | |
|---|---|---|---|---|---|---|---|---|---|
| $\varepsilon_{p,\,true}$ | σ (MPa) | $\varepsilon_{p,\,true}$ | σ (MPa) | $\varepsilon_{p,\,true}$ | σ (MPa) | $\varepsilon_{p,\,true}$ | σ (MPa) | $\varepsilon_{p,\,true}$ | σ (MPa) |
| **0.0000** | 640 | **0.0000** | 587 | **0.0000** | 522 | **0.0000** | 314 | **0.0000** | 116 |
| **0.0020** | 641 | **0.0020** | 601 | **0.0020** | 541 | **0.0020** | 315 | **0.0020** | 120 |
| **0.0050** | 641 | **0.0050** | 616 | **0.0050** | 559 | **0.0050** | 320 | **0.0050** | 122 |
| **0.0100** | 643 | **0.0100** | 618 | **0.0100** | 575 | **0.0100** | 320 | **0.0100** | 123 |
| **0.0200** | 659 | **0.0109** | 619 | **0.0175** | 591 | **0.0200** | 325 | **0.0200** | 123 |
| **0.0300** | 680 | | | | | **0.0205** | 325 | **0.0201** | 123 |
| **0.0352** | 686 | | | | | | | | |

| 800 °C (1472 °F) | | 900 °C (1652 °F) | | 1000 °C (1832 °F) | | 1100 °C (2012 °F) | |
|---|---|---|---|---|---|---|---|
| $\varepsilon_{p,\,true}$ | σ (MPa) | $\varepsilon_{p,\,true}$ | σ (MPa) | $\varepsilon_{p,\,true}$ | σ (MPa) | $\varepsilon_{p,\,true}$ | σ (MPa) |
| **0.0000** | 35.9 | **0.0000** | 26.2 | **0.0000** | 15.9 | **0.0000** | 7.0 |
| **0.0020** | 36.0 | **0.0020** | 27.0 | **0.0020** | 16.9 | **0.0020** | 9.0 |
| **0.0050** | 36.0 | **0.0050** | 27.9 | **0.0050** | 17.1 | **0.0050** | 10.5 |
| **0.0100** | 36.8 | **0.0100** | 28.1 | **0.0100** | 17.6 | **0.0100** | 11.4 |
| **0.0200** | 37.7 | **0.0200** | 29.0 | **0.0200** | 18.6 | **0.0200** | 11.7 |
| **0.0231** | 38.0 | **0.0300** | 29.8 | **0.0300** | 18.9 | **0.0500** | 12.4 |
| | | **0.0335** | 29.9 | **0.0318** | 19.0 | **0.0564** | 12.6 |

**Table 23.** Flow Stress of Simulated HSLA-80 CGHAZs after Heating to 1350 °C (2462 °F) and Cooling at 1 °C/s (1.8 °F/s). Note: Data as illustrated in **Figure 34** and terminal values are at the UTS.

| 25 °C (77 °F) | | 200 °C (392 °F) | | 400 °C (752 °F) | | 600 °C (1112 °F) | | 700 °C (1292 °F) | |
|---|---|---|---|---|---|---|---|---|---|
| $\varepsilon_{p,\,true}$ | σ (MPa) | $\varepsilon_{p,\,true}$ | σ (MPa) | $\varepsilon_{p,\,true}$ | σ (MPa) | $\varepsilon_{p,\,true}$ | σ (MPa) | $\varepsilon_{p,\,true}$ | σ (MPa) |
| **0.000** | 527 | **0.000** | 509 | **0.000** | 381 | **0.000** | 361 | **0.000** | 222 |
| **0.005** | 576 | **0.005** | 575 | **0.005** | 500 | **0.005** | 413 | **0.004** | 247 |
| **0.010** | 602 | **0.010** | 600 | **0.010** | 550 | **0.010** | 424 | | |
| **0.020** | 638 | **0.020** | 634 | **0.020** | 603 | **0.013** | 426 | | |
| **0.030** | 665 | **0.030** | 660 | **0.030** | 645 | | | | |
| **0.040** | 684 | **0.040** | 680 | **0.040** | 674 | | | | |
| **0.050** | 699 | **0.050** | 695 | **0.050** | 695 | | | | |
| **0.074** | 723 | **0.073** | 715 | **0.081** | 733 | | | | |

**Table 24.** Flow Stress of Simulated HSLA-80 CGHAZs after Heating to 1350 °C (2462 °F) and Cooling at 10 °C/s (18 °F/s). Note: Data as illustrated in **Figure 35** and terminal values are at the UTS.

| 25 °C (77 °F) | | 200 °C (392 °F) | | 400 °C (752 °F) | | 600 °C (1112 °F) | | 700 °C (1292 °F) | |
|---|---|---|---|---|---|---|---|---|---|
| $\varepsilon_{p,\,true}$ | σ (MPa) | $\varepsilon_{p,\,true}$ | σ (MPa) | $\varepsilon_{p,\,true}$ | σ (MPa) | $\varepsilon_{p,\,true}$ | σ (MPa) | $\varepsilon_{p,\,true}$ | σ (MPa) |
| **0.000** | 596 | **0.000** | 610 | **0.000** | 470 | **0.000** | 404 | **0.000** | 237 |
| **0.005** | 670 | **0.005** | 685 | **0.005** | 605 | **0.004** | 454 | **0.002** | 260 |
| **0.010** | 700 | **0.010** | 720 | **0.010** | 648 | | | | |
| **0.020** | 730 | **0.020** | 755 | **0.020** | 692 | | | | |
| **0.030** | 754 | **0.030** | 780 | **0.030** | 718 | | | | |
| **0.040** | 770 | **0.040** | 800 | **0.040** | 735 | | | | |
| **0.050** | 780 | **0.050** | 810 | **0.050** | 748 | | | | |
| **0.054** | 785 | **0.054** | 820 | **0.058** | 753 | | | | |

**Table 25.** Flow Stress of Simulated HSLA-80 CGHAZs after Heating to 1350 °C (2462 °F) and Cooling at 25 °C/s (45 °F/s). Note: Data as illustrated in **Figure 36** and terminal values are at the UTS.

| 25 °C (77 °F) | | 200 °C (392 °F) | | 400 °C (752 °F) | | 600 °C (1112 °F) | | 700 °C (1292 °F) | |
|---|---|---|---|---|---|---|---|---|---|
| $\varepsilon_{p,\,true}$ | σ (MPa) | $\varepsilon_{p,\,true}$ | σ (MPa) | $\varepsilon_{p,\,true}$ | σ (MPa) | $\varepsilon_{p,\,true}$ | σ (MPa) | $\varepsilon_{p,\,true}$ | σ (MPa) |
| **0.000** | 632 | **0.000** | 625 | **0.000** | 523 | **0.000** | 414 | **0.000** | 219 |
| **0.005** | 719 | **0.005** | 752 | **0.005** | 650 | **0.003** | 454 | **0.002** | 247 |
| **0.010** | 750 | **0.010** | 800 | **0.010** | 691 | | | | |
| **0.020** | 787 | **0.020** | 850 | **0.020** | 727 | | | | |
| **0.030** | 809 | **0.030** | 870 | **0.030** | 747 | | | | |
| **0.040** | 826 | **0.040** | 888 | **0.040** | 759 | | | | |
| **0.050** | 837 | **0.050** | 902 | **0.043** | 764 | | | | |
| **0.052** | 839 | **0.060** | 914 | | | | | | |

**Table 26.** Flow Stress of Simulated HSLA-80 CGHAZs after Heating to 1350 °C (2462 °F) and Cooling at 100 °C/s (180 °F/s). Note: Data as illustrated in **Figure 37** and terminal values are at the UTS.

| 25 °C (77 °F) | | 200 °C (392 °F) | | 400 °C (752 °F) | | 600 °C (1112 °F) | | 700 °C (1292 °F) | |
|---|---|---|---|---|---|---|---|---|---|
| $\varepsilon_{p,\,true}$ | σ (MPa) | $\varepsilon_{p,\,true}$ | σ (MPa) | $\varepsilon_{p,\,true}$ | σ (MPa) | $\varepsilon_{p,\,true}$ | σ (MPa) | $\varepsilon_{p,\,true}$ | σ (MPa) |
| **0.000** | 674 | **0.000** | 692 | **0.000** | 546 | **0.000** | 394 | **0.000** | 203 |
| **0.005** | 790 | **0.005** | 830 | **0.005** | 675 | **0.004** | 451 | **0.003** | 225 |
| **0.010** | 828 | **0.010** | 880 | **0.010** | 718 | | | | |
| **0.020** | 865 | **0.020** | 928 | **0.020** | 749 | | | | |
| **0.030** | 887 | **0.030** | 950 | **0.030** | 764 | | | | |
| **0.040** | 901 | **0.040** | 966 | **0.040** | 774 | | | | |
| **0.046** | 908 | **0.050** | 979 | | | | | | |
| | | **0.059** | 990 | | | | | | |

**Table 27.** Engineering Fracture Strain for the Specimens in **Figures 34-Figure** 37.

| Temperature (°C) [°F] | Fracture Strain, $\varepsilon_{f,\,eng}$ (mm/mm) | | | |
|---|---|---|---|---|
| | 1 °C/s Cooling | 10 °C/s Cooling | 25 °C/s Cooling | 100 °C/s Cooling |
| 25 [77] | 0.292 | 0.261 | 0.287 | 0.228 |
| 200 [392] | 0.200 | 0.208 | 0.193 | 0.197 |
| 400 [752] | 0.199 | 0.181 | 0.059 | 0.074 |
| 600 [1112] | 0.105 | 0.012 | 0.010 | 0.010 |
| 700 [1292] | 0.060 | 0.007 | 0.006 | 0.009 |

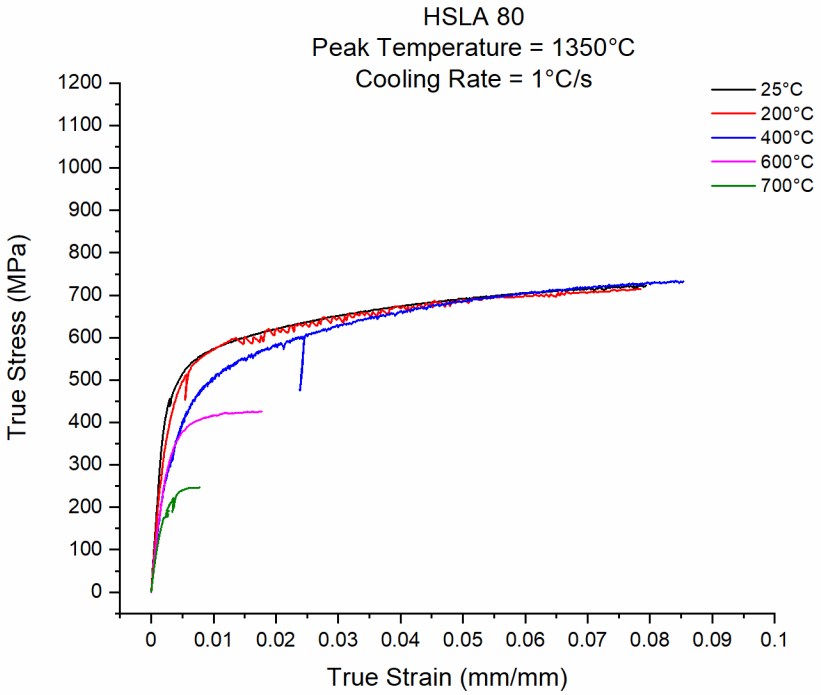


**Figure 68.** Uniaxial tension stress-strain curves from Gleeble tensile samples thermally cycled to a peak temperature of 1350 °C (2462 °F), cooled at 1 °C/s (1.8 °F/s), then reheated to the test temperature.

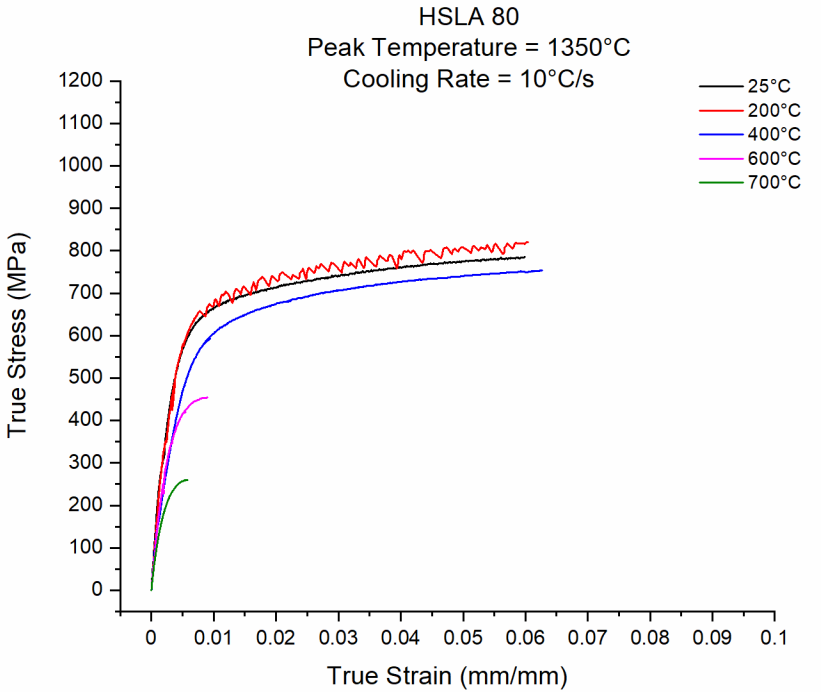


**Figure 69.** Uniaxial tension stress-strain curves from Gleeble tensile samples thermally cycled to a peak temperature of 1350 °C (2462 °F), cooled at 10 °C/s (18 °F/s), then reheated to the test temperature.

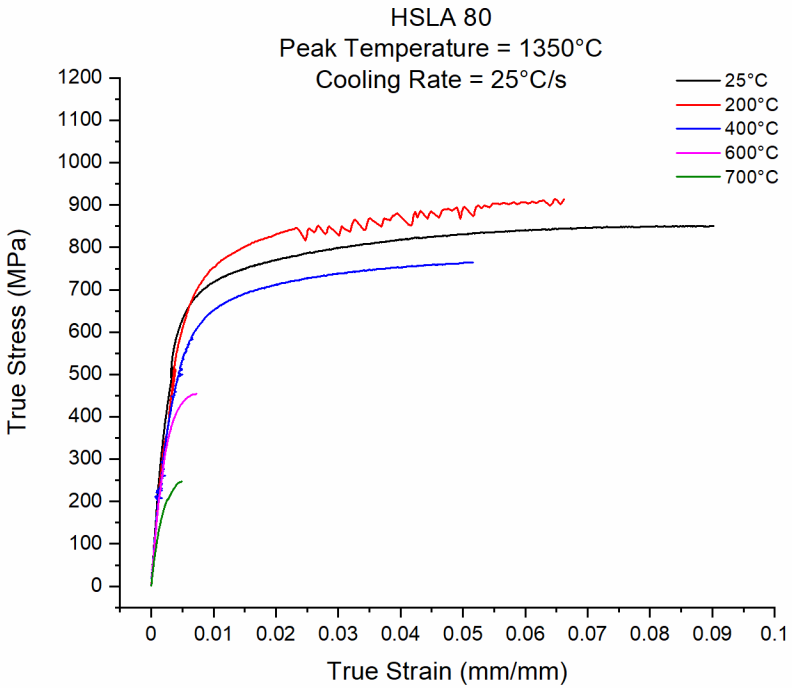


**Figure 70.** Uniaxial tension stress-strain curves from Gleeble tensile samples thermally cycled to a peak temperature of 1350 °C (2462 °F), cooled at 25 °C/s (45 °F/s), then reheated to the test temperature.

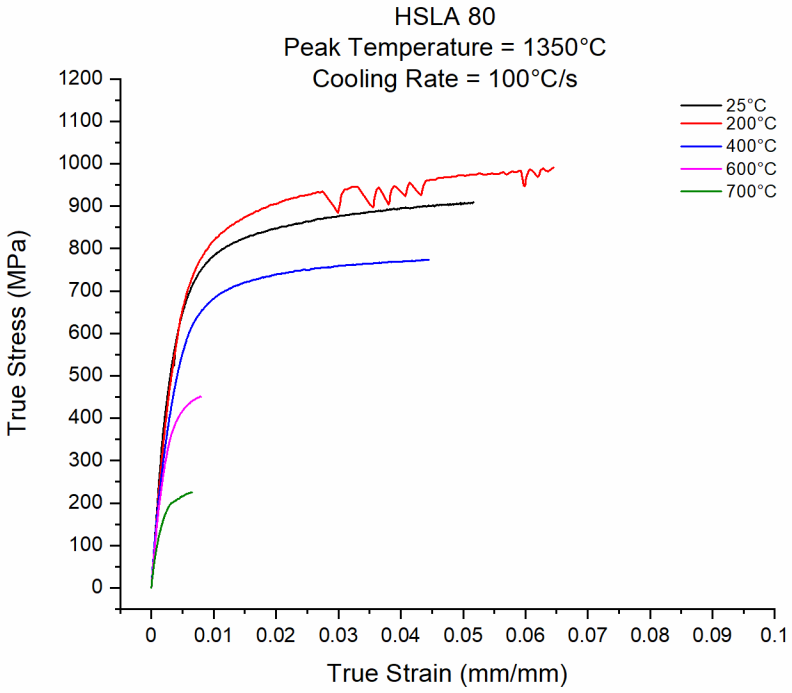


**Figure 71.** Uniaxial tension stress-strain curves from Gleeble tensile samples thermally cycled to a peak temperature of 1350 °C (2462 °F), cooled at 100 °C/s (180 °F/s), then reheated to the test temperature.

## REFERENCES

[1] L. F. Andersen, "Residual Stresses and Deformations in Steel Structures," Doctoral Thesis, Department of Naval Architecture and Offshore Engineering, University of Denmark, 2000.

[2] MIL-S-22698C, "Military Specification: Steel Plate, Shapes, and Bars, Weldable Ordinary Strength and Higher Strength: Structural," 29 June 1988.

[3] ASTM A945/M-16, "Standard Specification for High-Strength Low-Alloy Structural Steel Plate with Low Carbon and Restricted Sulfur for Improved Weldability, Formability, and Toughness," ASTM International, West Conshohocken, PA, 2016.

[4] NAVSEA Technical Publication T9074-BD-GIB-010/0300 Rev. 2, "Base Materials for Critical Applications: Requirements for Low Alloy Steel Plate, Forgings, Castings, Shapes, Bars, and Heats of HY-80/100/130 and HSLA-80/100," 18 December 2012.

[5] D. H. Bechetti, J. K. Semple, C. R. Fisher and W. Zhang, "Temperature-Dependent Material Property Databases for Marine Steels - Part 1: DH36," NSWCCD-61-TR-2019/03, 2019.

[6] J. K. Semple, D. H. Bechetti, W. Zhang and C. R. Fisher, "Temperature-Dependent Material Property Databases for Marine Steels - Part 2: HSLA-65," NSWCCD-61-TR-2020/03, 2020.

[7] ASTM E417-17, "Standard Test Method for Analysis of Carbon and Low-Alloy Steel by Spark Atomic Emission Spectrometry," ASTM International, West Conshohocken, PA, 2017.

[8] G. R. Eisler and P. W. Fuerschbach, "SOAR: An Extensible Suite of Codes for Weld Analysis and Optimal Weld Schedules," in *Seveth International Conference on Computer Technology in Welding*, San Francisco, CA, 1997.

[9] ASTM E1461-13, "Standard Test Method for Thermal Diffusivity by the Flash Method," ASTM International, West Conshohocken, PA, 2013.

[10] ASTM E1269-11 (2018), "Standard Test Method for Determining Specific Heat Capacity by Differential Scanning Calorimetry," ASTM International, West Conshohocken, PA, 2018.

[11] ASTM A370-18, "Standard Test Methods and Definitions for Mechanical Testing of Steel Products," ASTM International, West Conshohocken, PA, 2018.

[12] ASTM E21-17, "Standard Test Methods for Elevated Temperature Tension Tests of Metallic Materials," ASTM International, West Conshohocken, PA, 2017.

[13] T. D. Huang, M. Harbison, S. Scholler, H. Rucker, J. Hu, P. Dong, M. Collette, H. Chung, M. Groden, W. Zhang, J. Semple, R. Kirchain, R. Roth, M. Bustamante, Y. Yang, R. Dull, Y. Gooroochurn, M. Doroudian, C. F. Fisher, M. Sinfield, D. Kihl and A. Gonzalez, "Robust Distortion Control Methods and Implementation for Construction of Lightweight Metallic Structures," *SNAME Transactions*, 2016.

[14] J. J. Valencia and C. Papesch, "Automated Thermal Plate Forming: Apparent Specific Heat and Thermal Expansion During Heating of HSLA-80 and DH-36 Steel Plates," Naval Metalworking Center as operated by Concurrent Technologies Corporation, Johnstown, PA, 2005.

[15] N. Yurioka, S. Oshita and H. Tamehiro, "Determination of Necessary Preheating Temperature in Steel Welding," *Welding Journal,* vol. 52, no. 6, pp. 147-s to 153-s, 1983.

[16] ASTM E1382-97 (2015), "Standard Test Methods for Determining Average Grain Size Using Semiautomatic And Automatic Image Analysis," ASTM International, West Conshohocken, PA, 2015.

[17] R. R. Mohanty, N. Fonstein and O. Girina, "Effect of Heating Rate on the Austenite Formation in Low-Carbon High-Strength Steels Annealed in the Intercricial Region," *Metallurgical and Materials Transactiona A,* vol. 42A, no. 12, pp. 3680-3690, 2011.

[18] F. L. G. Oliveira, M. S. Andrade and A. B. Cota, "Kinetics of Austenite Formation during Continuous Heating in a Low Carbon Steel," *Materials Characterization,* vol. 58, pp. 256-261, 2007.

[19] C. A. Apple and G. Krauss, "The Effect of Heating Rate on the Martensite to Austenite Transformation in Fe-Ni-C Alloys," *Acta Materialia,* vol. 20, pp. 849-856, 1972.

[20] C. Heinze, A. Pittner, M. Rethmeiri and S. S. Babu, "Dependency of Martensite Start Temperature on Prior Austenite Grain Size and Its Influence on Welding-Induced Residual Stress," *Computational Materials Science,* vol. 69, pp. 251-260, 2013.

[21] M. Shome and O. N. Mohanty, "Continuous cooling Transformation Diagrams Applicable to the Heat-Affected Zone of HSLA-80 and HSLA-100 Steels," *Metallurgical and Materials Transactions A,* vol. 37A, pp. 2159-2169, 2006.

[22] B. Taljat, B. Radhakrishnan and T. Zacharia, "Numerical Analysis of GTA Welding Process with Emphasis on Post-Solidification Phase Transformation Effects on Residual Stress," *Materials Science and Engineering A,* vol. A246, pp. 45-54, 1998.

[23] X. Yue, J. C. Lippold, B. T. Alexandrox and S. S. Babu, "Continuous Cooling Transformatoin Behavior in the CGHAZ of Naval Steels," *Welding Journal,* vol. 91, no. 3, pp. 67-s to 75-s, 2012.

[24] Bainite Committee of The Iron & Steel Institute of Japan, "Atlas for Bainitic Microstructures, Vol. 1: Continuous-Cooled Microstructures of Low Carbon HSLA Steels," The Iron & Steel Institute of Japan, 1992.

[25] H. K. D. H. Bhadeshia and R. W. K. Honeycombe, Steels: Microstructure and Properties, 3 ed., Oxford, UK: Butterwoth-Heinemann, 2006.

[26] A. K. Sinha, Ferrous Physical Metallurgy, Stoneham, MA: Butterworth Publishers, 1989.

[27] G. Thewlis, "Classification and Quantification of Microstructures in Steels," *Materials Science and Technology,* vol. 20, pp. 143-160, 2004.

[28] International Institute of Welding, Compendium of Weld Metal Microstructures and Properties: Submerged-arc Welds in Ferritic Steel, Cambridge, UK: Woodhead Publishing, 1985.

[29] A. Bhagat, S. Pabi, S. Ranganathan and O. Mohanty, "Aging Behaviour in Copper Bearing High Strength Low Alloy Steels," *ISIJ International,* vol. 44, no. 1, pp. 115-122, 2004.

[30] J. O. Andersson, T. Herlander, L. Hoglund, P. F. Shi and B. Sundman, "Thermo-Calc & DICTRA, Computational Tools for Materials Science," *Calphad,* vol. 26, pp. 92-101, 2002.

[31] M. Peet, "Prediction of Martensite Start Temperature," *Materials Science and Technology*, vol. 31, no. 11, pp. 1370-1375, 2014.

[32] S. Kang, S. Yoon and S.-J. Lee, "Prediction of Bainite Start Temperature in Alloy Steels with Difference Grain Sizes," *ISIJ International,* vol. 54, no. 4, pp. 997-999, 2014.

[33] C. Capdevilla, F. G. Caballero and C. Garcia de Andres, "Determination of Ms Temperature in Steels: A Bayesian Neural Network Model," *ISIJ International,* vol. 42, pp. 894-902, 2002.

[34] J. S. Kirkaldy and D. Venugopalan, "Phase Transformations in Ferrous Alloys," in *Phase Transformations in Ferrous Alloys: Proceedings of an International Conference,* Philadelphia, PA, 1984.

[35] ASTM E111-17, "Standard Test Method for Young's Modulus, Tangent Modulus, and Chord Modulus," ASTM International, West Conshohocken, PA, 2017.

[36] E. 1993-1-1, "Eurocode 3: Design of steel structures - Part 1-1: General rules and rules for buildings," 2005.

[37] E. 1993-1-2, "Eurocode 3: Design of steel structures - Part 1-2: General rules - Structural fire design," 2005.

*This page intentionally left blank*

## DISTRIBUTION

### EXTERNAL

| | Copies |
|---|---|
| DEFENSE TECHNICAL INFORMATION CENTER<br>727 JOHN J KINGMAN ROAD<br>SUITE 0944<br>FORT BELVOIR, VA 22060-6218 | 1 |
| RESEARCH COMMONS<br>NAVAL UNDERSEA WARFARE CENTER<br>BUILDING 101<br>NEWPORT, RI 02841 | 1 |
| COMMANDER<br>ATTN: SEA 05P2<br>NAVAL SEA SYSTEMS COMMAND<br>1333 ISAAC HULL AVENUE S.E.<br>WASHINGTON NAVY YARD<br>WASHINGTON, DC 20376<br>ATTN: Archer, Bjornson, McGrorey, Melvin | 4 |
| ATTN: SEA 05P4<br>NAVAL SEA SYSTEMS COMMAND<br>1333 ISAAC HULL AVENUE S.E.<br>WASHINGTON NAVY YARD<br>WASHINGTON, DC 20376<br>ATTN: Rodgers | 1 |
| OFFICE OF NAVAL RESEARCH<br>875 N RANDOLPH ST<br>ARLINGTON, VA 22217<br>ATTN: Mullins | 1 |
| LIGHTWEIGHT INNOVATIONS FOR TOMORROW (LIFT)<br>1400 ROSA PARKS BOULEVARD<br>DETROIT, MI 48216<br>ATTN: Hawke | 1 |
| HUNTINGTON-INGALLS INDUSTRIES – INGALLS SHIPBUILDING<br>100 JERRY ST PE HIGHWAY<br>PASCAGOULA, MS 39581<br>ATTN: Scholler, Yang | 2 |
| OHIO STATE UNIVERSITY<br>WELDING ENGINEERING PROGRAM<br>1248 ARTHUR E ADAMS DR<br>COLUMBUS, OH 43221<br>ATTN: Zhang | 1 |

### NSWCCD INTERNAL DISTRIBUTION

| Code | Name | Copies |
|---|---|---|
| 60 | | 1 |
| 60 | Mercier | 1 |
| 60 | Rivera | 1 |
| 604 | Waters | 1 |
| 61 | DeLoach | 1 |
| 611 | Davis | 1 |
| 611 | Sinfield | 1 |
| 611 | Farren | 1 |
| 611 | Fisher | 2 |
| 611 | Bechetti | 1 |
| 611 | Semple | 1 |
| 612 | Roe | 1 |
| 651 | Nelson | 1 |
| 651 | Rodriguez | 1 |


NAVSEA
WARFARE CENTERS
Carderock